Copyright

by

Nathaniel T Heathman

2023

The Dissertation Committee for Nathaniel T Heathman Certifies that this is the approved version of the following Dissertation:

Advanced Manufacturing of Carbon Fiber Reinforced PAEK Composites: Bonding and Fracture Mechanisms

Committee:

Mehran Tehrani, Supervisor

Desiderio Kovar

Carolyn Seepersad

Hyonny Kim

Advanced Manufacturing of Carbon Fiber Reinforced PAEK Composites: Bonding and Fracture Mechanisms

by

Nathaniel Heathman

Dissertation

Presented to the Faculty of the Graduate School of
The University of Texas at Austin
in Partial Fulfillment
of the Requirements
for the Degree of

Doctor of Philosophy

The University of Texas at Austin
August 2023

Abstract

Advanced Manufacturing of Carbon Fiber Reinforced PAEK Composites: Bonding and Fracture Mechanisms

Nathaniel T Heathman, Ph.D. Mechanical Engineering

The University of Texas at Austin, 2023

Supervisor: Mehran Tehrani

Fiber reinforced composites are used in applications where lightweight, strength, stiffness, fatigue life, and corrosion resistance are critical. Thermoplastic composites (TPC) offer several advantages over thermosetting ones, including higher toughness, recyclability, weldability, and ease of repair. Over the last decade, the interest in in situ consolidation additive manufacturing (AM) of TPCs has increased exponentially due to their potential for rapid cycle out-of-autoclave processes. To this end, several limitations need to be resolved. Specifically in situ consolidation of TPCs usually result in low interlaminar bonding, weak matrix/fiber adhesion, high void content, and low crystallinity. This dissertation aims to provide a new understanding and solutions to these issues. The material system used in this work is carbon fiber reinforced low-melt polyarylyletherketone (LM-PAEK), processed via two AM methods: fused filament fabrication (FFF) and directed energy deposition (DED) in the form of laser-assisted automated fiber placement (AFP). By combining experiments and modeling, this work aims to develop an understanding of how processing parameters affect interlaminar bonding, void development, and crystallinity for both processes. This dissertation also investigates in situ consolidation of TPCs by examining the underlying physics that control bond strength and fracture toughness at inter-layer interfaces. Overall, this dissertation contributes to the knowledge base in the field, toward the adoption of low-energy and high-rate processes for manufacturing high-performance TPC structures.

Table of Contents

List of Tables

List of Figures

Nomenclature

ABS	*Acrylonitrile butadiene styrene*
AFP	*Automated fiber placement*
AM	*Additive manufacturing*
ASTM	*American Society for Testing and Materials*
CF	*Carbon fiber*
CFRP	*Carbon fiber reinforced polymers*
DCB	*Double cantilever beam*
DED	*Directed energy deposition*
DOE	*Design of experiments*
DSC	*Dynamic scanning calorimetry*
ENF	*End notched flexure*
FEA	*Finite element analysis*
FFF	*Fused filament fabrication*
FRP	*Fiber reinforced polymer composites*
HGT	*Hot gas torch*
HIP	*Hot isostatic pressing*
ICAT	*In-situ consolidation automated fiber placement of thermoplastic composites*
ILSS	*Interlaminar shear strength*
ILTS	*Interlaminar tensile strength*
LM-PAEK	*Low melt polyaryletherketone*
PAEK	*Polyaryletherketone*
PBI	*Polybenzimidazole*
PEEK	*Polyetheretherketone*
PEI	*Polyetherimide*
PEKK	*Polyetherketoneketone*
PPS	*Polyphenylene*
PSI	*Pounds per square inch*
RTM	*Resin transfer molding*
SBS	*Short beam strength*
SEM	*Scanning electron microscope*
SLS	*Selective laser sintering*
TPC	*Thermoplastic composite*
UTS	*Ultimate tensile strength*
VBO	*Vacuum bag only*
μCT	*Micro computed tomography*

Chapter 1. Introduction

Fiber reinforced polymer composites (FRP) have been a mainstay in production of lightweight, high strength components since the 1930s when Owens Corning developed the first fiberglass polyester resin FRP. Since then, the composites industry has expanded significantly, with FRPs being used in components ranging from household appliances to automotive and aerospace applications. There are two main elements to FRPs, fibers and resin, with a significant number of options for both. One of the most utilized fiber types is carbon fiber (CF) due to its high specific strength, specific stiffness, and corrosion resistance; polymer composites manufactured with carbon fiber are deemed carbon fiber reinforced polymers (CFRPs). CFRPs can be manufactured using a variety of methods including hand layup, resin transfer molding (RTM), thermoforming, filament winding, and various additive processes. Both thermosetting and thermoplastic polymers can be utilized in the manufacturing of CFRPs, with each type having specific benefits and drawbacks.

Thermosetting resins are the most common polymers utilized in manufacturing CFRPs due to their low viscosity and excellent thermo-mechanical properties. Once cured these polymers form a cross-linked molecular structure that offers a high strength, high temperature stability, and corrosion resistance. The main drawbacks to thermosets are a long and energy-intensive autoclave curing process and inability to re-shape or alter the component once fully cured. Thermoplastics on the other are a much less utilized polymer system in the manufacturing of CFRPs but offer many benefits when compared with thermosets.

Thermoplastics contain a molecular structure of long spaghetti like chains, with branches, that flow when heated above melting temperature, intertwining with one another to form strong entanglement once cooled blow melt. Unlike thermosets, these bonds can be broken and reformed any number of times by melting and cooling the material, as long as the system does not reach its thermal degradation temperature. While the main advantage of thermoplastics over thermosets is the ability to transition from melt to a solid repeatedly, they also offer several other benefits. Thermoplastic composites (TPCs) boast a similarly high specific mechanical properties to thermosets, while providing increased impact resistance, excellent corrosion and chemical resistance, ease of repair, and recyclability due to the ability to be remelted. In a world transitioning towards a sustainable future, the recyclability aspect is of utmost importance, especially considering thermoset composites are traditionally discarded after their lifecycle.

There are many thermoplastic variants utilized in the manufacturing of TPCs, from more common plastics such as nylon and acrylonitrile butadiene styrene (ABS) to high-performance plastics such as polyphenylene sulfide (PPS) and those from the polyaryletherketone (PAEK) family. Within the composites industry, PAEK polymers have generated the most attention as materials that have the best potential for pushing the envelope of what TPCs are capable of. PAEK polymers sit atop the thermoplastics pyramid and have a molecular backbone consisting of ether (E) and ketone (K) groups with aryl (A) linkages. These polymers form a semi-crystalline structure when solidified and achieve a high strength, stiffness, and thermal stability with melting temperatures upwards of 300 ˚C.

The traditional manufacturing method for TPCs is compression molding. Compression molding is a thermoforming process that consolidates stacked plies of thermoplastic towpregs (pre-impregnated fibers with a thermoplastic) between heated mold halves to form a part. Typically, compression molding of TPCs is a multistep process requiring the TPC towpregs (referred to tapes hereafter) to be initially fully consolidated into a flat plate, after which is then inserted into the final mold for taking the part’s shape. Compression molding is a costly process requiring specialty equipment and precisely machined molds, it also requires large amounts of energy to pre-heat the TPC plate and molds to melting temperature. Although expensive, the process does produce fully consolidated TPCs with high crystallinity due to precise temperature and pressure controls and slow cooling. Compression molding of TPCs is generally suited for medium to large production runs of smaller components with simple geometries. These drawbacks open the door for manufacturing technologies that are capable of layer-by-layer consolidation, producing larger yet more intricate part geometries, and require less energy.

In both conventional TPC manufacturing processes and layer by layer additive processes, final part strength is dependent on the same mechanisms, intimate contact development, polymer chain diffusion, thermal history and crystallization kinetics, void formation, and residual stress development [1]. Intimate contact is specified as the percentage of the total area of each TPC tape surface in contact with one another during the forming process and is quantified as the degree of intimate contact [2]. The degree of intimate contact is dependent on the viscosity of the material at melt and the time interval and magnitude of the pressure applied [3]. Once intimate contact is achieved, polymer chains begin to diffuse across the interface, intertwining with other polymer chains to form bonds between tapes [4]. For semi-crystalline materials, such as discussed here, another phenomenon called crystallization begins to come into play as the material cools from melt. Crystallization occurs as the polymer chains organize into ordered plate-like structures called lamella. The lamellae continue to grow radially outward from a nucleation site, forming a spherical or semispherical structure known as a spherulite. Crystallization is highly dependent on cooling rate from melt [5]. Both interdiffusion and crystallization play a major role in strength development of a fully consolidated TPC part with interdiffusion (also referred to autohesion in the literature) being the main factor in degree of consolidation (bonding) and crystalline regions providing improvements to overall strength, stiffness, toughness, and wear resistance when compared to their amorphous counterparts.

Void development during the manufacturing of TPC parts is another critical factor affecting their performance. Voids can decrease the overall strength of the part or act as stress concentration points which detract from the fatigue strength. Void content must be minimized to less than 2% in parts destined for use in critical applications. Voids can appear from a number of sources during TPC manufacturing; volatiles trapped on the surface or within the tapes that expand and migrate through the tapes once the matrix is in the melt window, foreign objects can become trapped between layers which allow for voids to form, or even a lack of intimate contact can lead to voids appearing at ply interfaces [6], [7]. The main method to mitigate void formation is to keep a high consolidation pressure on the laminate all the way from melt to below the glass transition temperature. Residual stresses are an additional issue with TPC manufacturing. Due to the differences in thermal expansion coefficients of the fibers and matrix, as well as thermal gradients imposed during manufacturing processes, residual stresses can develop within TPCs parts, leading to their distortion once cooled. Careful planning and process parameter control must be carried out in order to minimize the effect of residual stresses.

Intimate contact development, polymer chain interdiffusion, thermal history and crystallization kinetics, void formation, and residual stress development are all critical aspects of TPC manufacturing. While these main mechanisms carry over between each type of manufacturing process, they are not carried out in the same manner. Understanding the specific TPC manufacturing process and how to maximize intimate contact, interdiffusion, and crystallization, while minimizing void development and residual stress buildup is key to manufacturing high strength parts.

Given the inherent ability of TPCs to be melted from a solid, deposited, then resolidified, they are a natural fit for utilization in additive manufacturing (AM). In the past, AM has typically utilized low strength polymers to fabricate prototypes or novelty items, however, with the introduction of short and continuous CF into the feedstock material, significant improvements in stiffness and strength can be achieved, even to the point of producing end use components for a variety of applications. In the current state of industrial advancement, PAEK polymers combined with continuous CF offer the best mechanical and thermal performance among all additively manufactured TPCs, with a significant amount of research being undertaken around the world on these materials. AM of TPCs enables optimized design methods coupled with freeform fabrication, taking full advantage of processes and materials to produce the most lightweight, high strength components possible with minimal waste and potential for recycling at the end of their lifecycle.

Two of the main AM methods being utilized and studied for TPCs are fused filament fabrication (FFF) and directed energy deposition (DED) in the form of automated fiber placement (AFP). AFP is a type of robotic manufacturing technology that allows for rapid construction of large complex laminates. AFP has traditionally been used to construct thermosetting-based composites that are in a variety of applications but with the main target being aerospace. AFP has expanded to include in-situ consolidation of TPCs. In-situ AFP layup of thermoplastics is similar to manufacturing of thermoset laminates, except a high temperature heating source, such as a laser or hot gas torch, is used to fully melt the thermoplastic tape as it passes under a compaction roller [1]. The use of thermoplastics offers the promise of decreasing manufacturing time and overall cost. However, there are several drawbacks to using thermoplastics in AFP, with the main issues being low interlaminar shear strength, slow layup speeds, high void content, and low crystallinity.

Fused filament fabrication or FFF, has been one of the predominant forms of extrusion-based AM. While this process is great for producing prototypes and non-load bearing components, the parts manufactured via this process lack the strength to be more commonly used in industry. This process has advanced in recent years by the development of high-performance PAEK thermoplastics and the incorporation of short and continuous carbon fibers into the filaments. While these new filaments have produced promising mechanical properties, the process still suffers from poor interlaminar strength, high porosity, and low crystallinity [8], [9].

Developing equipment capable of processing these materials has been one of the major challenges to the advancement of AM, however, these processes are just as dependent on the development of the thermoplastics themselves. As previously mentioned, the PAEK family of polymers has provided quite the solution to producing high strength components, with polyetheretherketone (PEEK) and polyetherketoneketone (PEKK) being commonly used in FFF and AFP. While these materials have high strengths, chemical resistance, and glass transition temperatures, the manufacturing process temperatures for these materials is close to 400 ˚C and typically require heated chambers to achieve inter-layer bonding [10]. These high processing temperatures pose challenges for manufacturing, specifically high-speed manufacturing required in AFP. To combat this, a low melt PAEK (LM-PAEK™) has been developed by Victrex® that offers similar mechanical and thermal properties to PEKK, but with a 40 ˚C reduction in processing temperature [10]. This material is the latest development in the semi-crystalline high performance thermoplastic family and enables easier manufacturability. The focus of this dissertation is to investigate the resulting mechanical properties, thermal properties, and microstructure of CF/LM-PAEK™ manufactured via FFF and in-situ consolidation automated fiber placement of thermoplastic composites (ICAT) for advancement of the technology as a whole.

This work is focused on four individual studies, all pertaining to further the understanding of processing and failure mechanics in additive manufacturing of CF/LM-PAEK. The first study investigates interlaminar bonding and void content of discontinuous CF/PEKK manufactured via FFF. The second study provides a comprehensive investigation into continuous fiber CF/LM-PAEK manufactured via FFF, where tested parts are analyzed for their interlaminar properties, crystallinity, void content, and fiber misalignments. The 3rd and 4th studies both investigate CF/LM-PAEK manufactured via ICAT. The first one aims to link processing parameters to interlaminar bonding as well as provide insights into crystallinity and void development. The study also provides modeling results to correlate process physics to interlaminar bonding strength. The second ICAT study investigates fracture toughness in mode I and mode II of parts produced through ICAT, high speed AFP layup with post compression molding. Summaries of each presented study are provided in the following paragraphs.

Chapter 2 presents an investigation of bonding mechanisms in additively manufactured carbon fiber PEKK parts via annealing and hot isostatic pressing (HIP) post processing. The goal of the study is to isolate and investigate the individual bonding mechanisms of intimate contact, crystallization, and interdiffusion, and understand how they affect the resulting bond strength. To this end, specimens were manufactured via FFF out of carbon fiber PEKK in the build (vertical or Z-) direction. Specimens were then treated to varying post processing techniques including annealing and HIP. Interlaminar bonding strength, stiffness, crystallinity, and void content for all samples were measured and correlated. Results showed that all samples contained a significant amount of porosity that HIP treatment could effectively remove. This study suggests that while intimate contact is important, the development of crystallinity plays a more significant role in establishing interlaminar bonding strength in tested samples.

In Chapter 3, continuous fiber FFF is employed to manufacture a verity of specimens from high-performance Cf/LM-PAEK filaments. These specimens were tested to gain insights into their microstructure and thermo-mechanical properties. Additionally, complex-shaped parts are manufactured using out-of-plane 3D printing capability of the equipment and investigated for manufacturing defects as a result of fiber steering. The results open up possibilities for the use of LM-PAEK as a replacement for PEEK in continuous fiber fused filament fabrication. They also provide new information regarding the manufacturing of intricate parts.

Chapter 4 elaborates on the construction of a laser-assisted AFP manufacturing cell, beginning with careful component selection and detailing the assembly process. It provides details of the various factors involved in building such a manufacturing cell, from the choice of components to the actual construction. Using this manufacturing cell, Chapter 5 focuses on investigating the in-situ consolidation AFP of TPCs (ICAT) toward their process optimization and revealing how heat and pressure result in consolidation of ICAT coupons. To achieve this objective, the AFP system was employed to manufacture short beam shear samples using CF/ LM-PAEK tapes, at various processing parameters. The obtained results were analyzed to gain insights into the influence of ICAT process parameters on interlaminar bonding, crystallinity, and void content of the resulting parts. Additionally, multi-physics finite element analysis (FEA) was utilized to reveal how the repetitive application of temperature and pressure controls void formation and elimination, crystallinity, and bonding in the ICAT process. Furthermore, a comparison was made between post-fracture specimens produced via ICAT and traditional compression molding to explain the underlying failure mechanisms in ICAT coupons. The findings of this study demonstrate that achieving high interlaminar shear strengths exceeding 60 MPa is feasible while maintaining low void content (<1%) and high crystallinity (>20%) through the ICAT process. These results suggest that ICAT holds significant potential as a viable manufacturing process for the next generation of aerospace composites.

The study presented in Chapter 6 aims to enhance our understanding of bonding strength and fracture toughness in ICAT parts. Several ICAT coupons were manufactured, specifically SBS and Mode I and Mode II fracture toughness samples, using thin CF/LM-PAEK tapes. The manufacturing speed was varied to create specimens with two different sets of bonding strengths and crystallinities. Additionally, specimens prepared using conventional thermoforming are included for comparison. The sample sets are evaluated based on interlaminar bonding strength, mode I and mode II fracture toughness, crystallinity, void content, and failure modes. The results of all the tests provide valuable insights into how varying levels of bonding and crystallinity influence fracture toughness and resist crack propagation in ICAT samples. The study demonstrates that ICAT can produce coupons with interlaminar strength lower than those molded by compression, yet with comparable fracture toughness values.

Chapter 7 provides major conclusions drawn from the body of this dissertation and outlines knowledge gaps for future studies.

Chapter 2. Studying Bonding Mechanisms in Additively Manufactured Carbon Fiber PEKK Parts via Hot Isostatic Pressing

Authors: Nathaniel Heathman, Timothy Yap, and Mehran Tehrani

Additive manufacturing (AM) of composites is a rapidly expanding technology, with increasing focus on printing end-use parts rather than prototyping. Fused filament fabrication (FFF) is relatively inexpensive and fast compared to other AM technologies. However, the resulting FFF parts suffer from low interlaminar mechanical properties due to poor layer-to-layer bonding and the presence of voids. Understanding the underlying bonding mechanisms and their effects on bond strength is crucial to addressing the shortcomings of FFF composites. This study investigates these mechanisms through hot isostatic pressing (HIP) post-processing. HIP utilizes high temperatures and pressures to close voids and enhance properties of AM parts. By choosing specific HIP parameters, this study achieves parts with low void content and low crystallinity, allowing for the separation and understanding of two bonding mechanisms, namely intimate contact and crystallization. In particular, the effects of HIP on the structure and interlaminar strength of short carbon fiber-reinforced polyetherketoneketone (PEKK) parts manufactured via FFF are investigated in this chapter. Coupons were printed vertically (normal to the print bed or along the Z-direction) and post-processed for one hour in an in-house HIP device. The HIP pressure was set to 0, 0.138, and 1.38 (MPa) with a constant temperature of 165 °C (slightly above its glass transition temperature but below cold crystallization). Another set of reference samples were heat-treated at atmospheric pressures, with their temperature raised to 200 °C to enhance their crystallinity. All samples were characterized via tensile tests to evaluate their inter-layer tensile strength and modulus. Additionally, the samples were analyzed using X-ray micro-computed tomography (μCT) to assess their void content before and after the HIP processing. The structure, morphology, and properties of all tested samples were compared and correlated to the HIP treatment conditions. It was concluded that low-temperature HIP at relatively high pressures can nearly eliminate all voids in samples, but the measured properties are still significantly lower than those with higher crystallinities and even larger void contents. This study therefore highlights the effect of crystallization, as opposed to other mechanisms such as intimate contact and interdiffusion, on strength development in composites fabricated through FFF. Finally, this work proposes a new processing route to significantly enhance inter-layer properties of FFF composite parts, paving the way for their use in functional and structural applications.

This chapter contains material from the following publication: [8] Proc. 35th Annu. Am. Soc. Compos. Tech. Conf. 2020.

Author Contribution
Nathaniel H: Fabrication, testing, analysis
Timothy Y: Testing
Mehran T: Supervisor

INTRODUCTION

Additive manufacturing (AM) of composites is a rapidly expanding technology with an increasing focus on printing end use parts without the use of molds [11], [12]. To this end, used filament fabrication (FFF) offers a relatively inexpensive and fast approach for fabricating parts from both short and continuous fiber reinforced plastic filaments [13] [14]. In FFF, a thermoplastic filament is fed through a nozzle which melts the filament and selectively deposits it onto a build plate where it is allowed to cool. The nozzle moves upwards by one-layer height in relation to the build plate and selectively deposits more plastic melt onto the previous layer. The process repeats to build the entire part layer-by-layer. The resulting FFF parts suffer from low interlaminar (or inter-layer) mechanical properties due to poor layer-to-layer bonding (or adhesion) and voids [11]. The poor layer-to-layer strength arises from poor bonding between layers, which in turn is due to the filaments' fast cooling from melt and lack of pressure during filament deposition [15]. On the other hand, voids arise from porosity in the stock material and individual rasters or roads being laid down with gaps between each other, resulting in voids running parallel to rasters. Voids formed in FFF parts degrade mechanical properties in the transverse and vertical (perpendicular to build plate) directions [16], [17].

A possible solution to alleviate the effects of porosity and poor inter-layer bonding is post processing using hot isostatic pressing (HIP) [18], [19]. HIP applies high temperatures and pressures to consolidate parts, reducing their void content and in turn improving their mechanical properties. Additionally, the high temperatures enhance inter-layer polymer inter-diffusion and can potentially increase the crystallinity of the parts (if a semi-crystalline polymer is used), which in turn would improve mechanical properties [20], [21]. On the downside, HIPing results in part deformation, since it is typically carried out above the glass transition temperature of the polymer, and bulk shrinkage of parts, which can be significant.

Polyetherketoneketone (PEKK) is a high-performance polymer that can withstand high temperatures while retaining mechanical strength, making it a material of choice for various applications. PEKK can be differentiated based on the ratio of terephthalic to isophthalic monomers (T/I ratio) [22]. A T/I ratio of 70/30 gives a melt temperature of ~332 °C and a glass transition temperature of ~162 °C, and a crystallinity between 5% to 20% depending on manufacturing (most strongly affected by cooling rate from melt) conditions. Short carbon fibers (CF) can be added to PEKK to make a reinforced composite, where the beneficial properties of both materials are combined. CF reinforced PEKK demonstrates a higher Young's modulus and ultimate tensile strength than the neat PEKK [23]. No literature exists on FFF of PEKK and CF-PEKK composites, although a previous study on CF reinforced polyetheretherketone (PEEK), a polymer similar to PEKK but more crystalline, suggested a six- and three-fold improvement in ultimate tensile strength and Young's modulus, respectively, by the addition of CF [24].

Bonding formation in FFF of thermoplastics can be simply explained by three consecutive phenomena: polymer flows and the two bonding surfaces "kiss" (intimate contact), then they start sharing long chain polymers (interdiffusion), and finally solidifying into a semi-ordered structure (crystallization). This paper aims to better understand the effects of these three processes on bond formation by utilizing HIP on carbon fiber PEKK coupons manufactured by FFF. Tensile samples were printed in the Z-direction and post processed according to various HIP treatment parameters or simple annealing. The coupons were then tensile tested to assess their Young's modulus and ultimate tensile strength in the vertical (Z) direction. Additionally, the samples were analyzed using μCT to assess their void content. Structure, morphology (crystalline degree), and properties for all HIP treated samples are compared against reference samples that were printed with no post processing treatment and annealed samples that were heat treated but subjected to no pressure. A schematic of the fabrication, HIP treatment and characterization is provided in Figure 1. The following sections provide a description of the sample preparation, HIP treatment process, and the resulting findings.

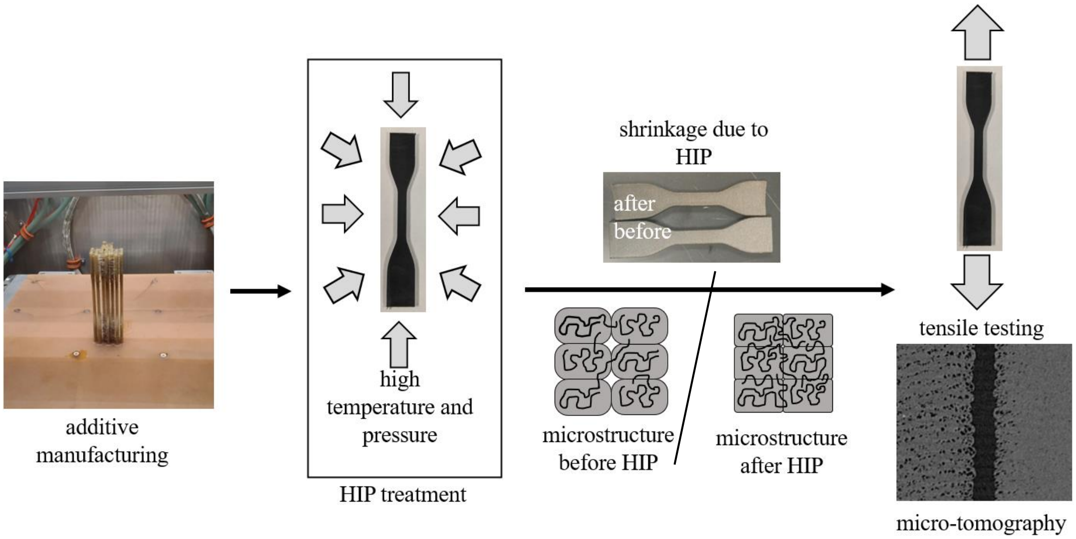

Figure 1: Schematic of the fabrication, HIP treatment and characterization. The inserts show the bulk shrinkage that can occur due to HIPing, and the hypothesized changes to the microstructure before and after HIPing.

EXPERIMENTAL APPROACH

Materials

The filament used for printing the samples was 3DXTech, CarbonX™ CF reinforced PEKK-C; PEKK copolymer with a T/I ratio of 70/30, filled with Toray T-800 aerospace-grade chopped carbon fiber. Filament diameter was 1.75 mm. The manufacturer claims filament-direction strength and Young’s modulus of 115 MPa and 9.56 GPa, respectively, a glass transition temperature of 165 °C, and a filament-direction heat deflection temperature of 280 °C.

Fabrication

ASTM Type IV tensile coupons were printed on an AON3D M2 industrial printer. Samples were printed six at a time in the Z-direction. The Z-direction samples were increased in size by 1.27 mm in the X and Y directions to aid in their AM. The Z-direction coupon was sliced with Simplify3d at a 100% infill using entirely perimeter shells so that the extrusion paths are concentric within each layer. Samples were printed one at a time in the X-direction, with no increase in size. The X-direction coupon was sliced with Simplify3d at a 100% infill using only rectilinear rasters in the X direction with no perimeter shells. A nozzle diameter of 0.6 mm, layer height of 0.2 mm, nozzle speed of 20 mm/s, nozzle temperature of 360 °C, bed temperature of 140 °C, and chamber temperature of 95 °C were used.

Post Processing

The tensile coupons were post processed using a custom fabricated HIP device capable of 13.8 MPa (2000 psi) and 230 °C. All samples were HIP treated using 99.9% pure nitrogen slightly above their glass transition temperature (T_g) but below the cold crystallization temperature, at 165 °C, and dwelled at temperature and pressure for one hour. Pressures for HIP treatment were varied between 0 MPa (0 psi), 0.138 MPa (20 psi), and 1.38 MPa (200 psi). From this point forward, HIP pressures will be noted in English units of PSI to maintain consistency with the equipment parameters. To keep the samples from warping, they were constrained vertically. The HIP procedure followed for all samples consisted of bringing the samples to 165 °C, pressurizing the device to the desired pressure, allowing the samples to dwell for one hour, turning off the heater, bleeding pressure once the temperature reached 100 °C, then removing the samples. A final sample set was annealed at ambient pressure but higher temperatures to promote crystallization. The purpose of this sample set was to analyze the interlaminar bonding strength of the material with enhanced crystallinity but no void consolidation. A table summarizing the post processing parameters is presented in Table 1.

Table 1: HIP Post-Processing Conditions

Sample Name	**Post-processing Conditions**	
	Temperature (°C)	**Pressure (psi)**
ref	NA	NA
0psi	165	0
20psi	165	20
200psi	165	200
Annealed	165 and 200	0

Characterization

Each tensile coupon was tested following ASTM standards on a MTS Criterion™, Model 43 universal test system with a 50 kN load cell. A testing speed of 5 mm/min was used and strain was measured using an MTS extensometer with a gauge length of 25.4 mm. Gauge section thickness and width was measured with calipers at several locations and recorded prior to each tensile test. A total of five samples were tested for each HIP treatment condition. The tensile strength and Young's modulus were calculated from data recorded from each test.

To assess void content in the samples, the grip section of tensile coupons from each sample configuration was scanned in a μCT 400 Zeiss scanner. All samples were placed next to each other and scanned with a 12.1-microns resolution. Several μCT scans were analyzed for void content calculations in Fiji. The void analysis was done from the direction perpendicular to the filament path and cropped down to exclude edge features and layers close to the print bed. The threshold of the image sequence was adjusted to show the matrix and fibers in black and voids in white. A histogram was developed from each sequence and the void percentage was calculated based upon the number of white pixels.

RESULTS AND DISCUSSIONS

Averaged tensile testing results are summarized for all sample configurations in Figure 2. Representative stress-strain curves for each sample set are also shown in Figure 3. All the Z-direction samples suffered from a brittle fracture in the gauge section, suggesting interlaminar failure, which was further verified by visual inspection. In comparing average ultimate tensile strength for each experimental set, all samples that had undergone post-treatments outperformed the reference. The samples treated at 165 °C, 0 psi, and 20 psi show no discernable improvement in strength compared to the reference sample. At 165°C and 200 psi there is some improvement in ultimate tensile strength (UTS), 8.1±1.2 MPa compared to 5.3±1.4 MPa. However, this is still much lower than the manufacturer proclaimed 115 MPa in the filament direction. Significant improvement is achieved in the annealed sample, with a measured UTS of 53.0±4.4 MPa.

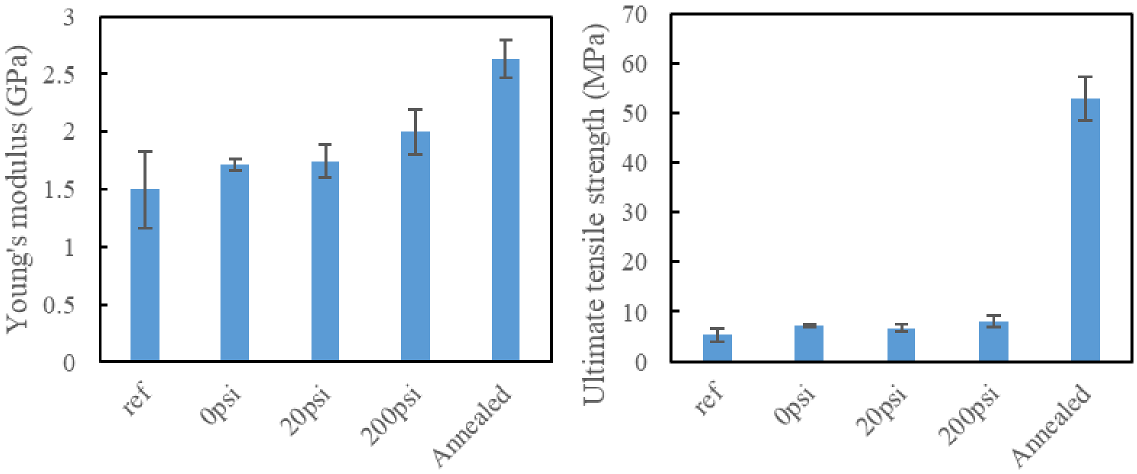

Figure 2: Ultimate tensile strength (left) and Young’s modulus (right) for studied samples. The 0, 20, and 200 psi correspond to the post treatment pressure at a treatment temperature of 165 °C. Annealed corresponds to 0 psi at 165 °C followed by 200 °C.

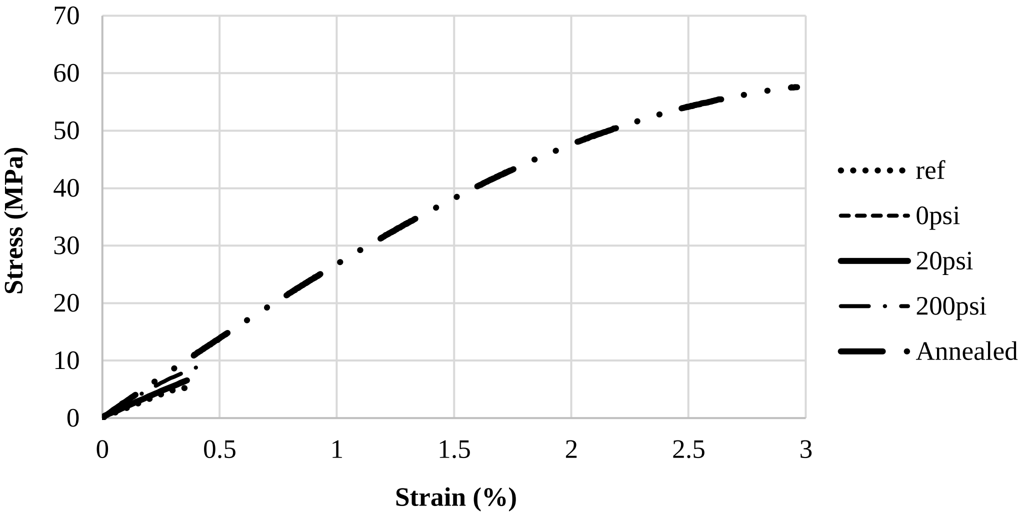

Figure 3: Representative stress-strain curves for different sample types.

The average Young’s modulus for each experimental set showed the same trend as compared to the ultimate tensile strength. The HIP samples treated 0 psi, and 20 psi showed a negligible increase compared to the reference samples at 1.7±0.1 GPa compared to

1.5±0.3. The 200 psi HIP samples show the largest increase in Young's modulus at 2.0±0.2 GPa. The annealed sample resulted in the highest modulus of 2.6±0.2 GPa. To put this in perspective, the moduli of bulk crystallized PEKK and CF-PEKK in the transverse direction (not along the aligned fibers) are around 3 GPa. UTS and modulus results show highly anisotropic behavior compared to strengths in the X direction. Both fiber alignment, polymer chain alignment, interlaminar bonding strength, and crystallization provide a role in this anisotropic behavior and will be discussed further in the following sections. To understand the effects of HIP on mechanical properties of the examined samples, X-ray μCT characterization was conducted. Reconstructed 2D μCT results are shown in Figure 4 and Figure 5. A μCT based 3D void reconstruction for the annealed sample is provided in Figure 6. These results confirm both inter-raster and intra-raster voids contributing to the large porosity observed in all samples. The results reveal no improvement in void content between the reference and 0 psi samples, with the reference sample having a void content of 19.4% and the 0 psi sample having a similar void content of 20.6%. The largest improvement in void content was achieved for the 200 psi sample. The annealed sample shows a void content of 16%, a small improvement over the reference sample. While the results show an increase of voids from the reference to the 0 psi sample, this is most likely due to the variation in print results. It is also important to note that while the interior of the 20 psi and 200 psi samples showed a significant reduction in voids, HIP treatment does not affect the voids on the outermost region of the samples, as shown in the orange box in Figure 5. This is due to the voids on the outermost region of the samples having an open path to the exterior. While not studied here, given the brittle behavior of the samples tested, surface defects like those shown can degrade the mechanical performance of HIP samples.

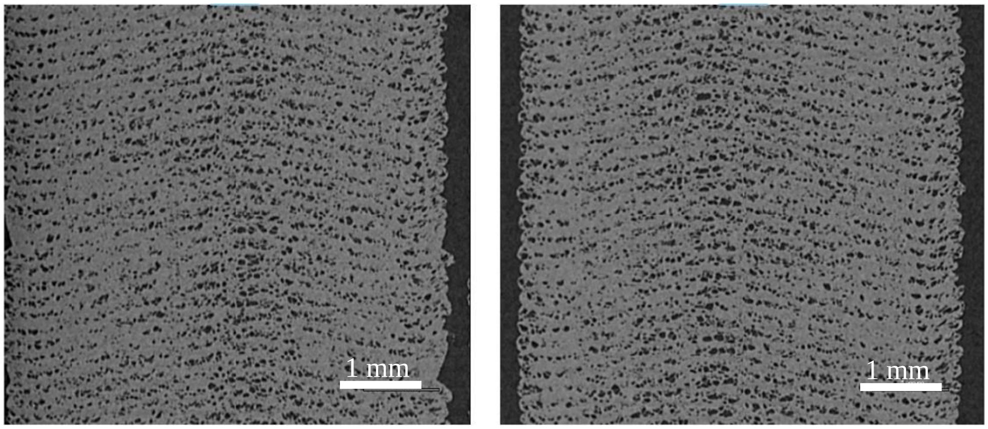

Figure 4: μCT cross section scans of samples, left is the reference and right is the 0 psi sample.

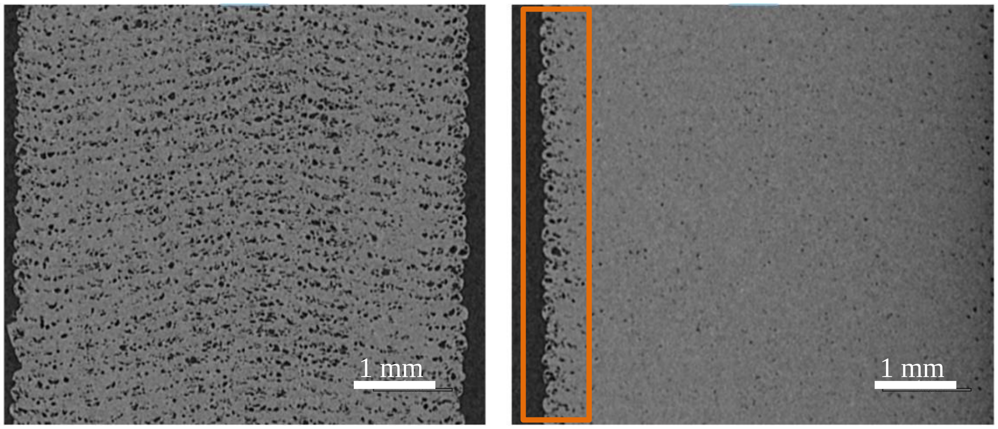

Figure 5: μCT cross section scans of samples, left is the 20 psi and right is the 200 psi sample.

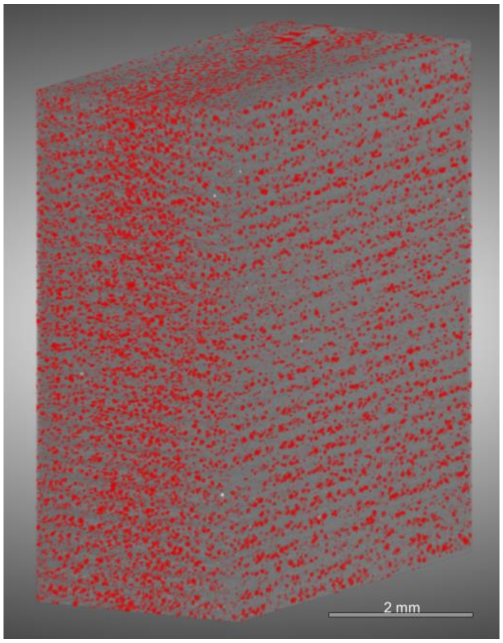

Figure 6: Annealed sample with μCT void reconstruction.

All measured results, including estimated crystallinity values for all samples, are tabulated in Table 2. PEKK 70/30 doesn't achieve high crystallinity when cooled at high rates from the melt, which is the case in FFF. It is therefore expected to achieve a low crystallinity of around 5-6%. Similarly, HIP at temperatures above PEKK's T_g yet below its cold crystallization temperature of nearly 200 °C, doesn't change the crystallinity. Finally, annealing at 200 °C for an hour has shown, in unpublished work by our group, to enhance crystallinity to above 20%, which is near the maximum achievable value for PEKK.

It is shown here that with limited polymer mobility at only a few degrees above PEKK's Tg (162 °C), a high enough HIP pressure of 200 psi can successfully close most voids resulting in nearly void-free samples. This, however, resulted in only a minor increase in mechanical properties, suggesting that while intimate contact and interdiffusion (resulting in void elimination) have significantly improved, as measured by the reduced void content and increased modulus, their effects on inter-layer strength and stiffness is relatively low. In contrast, the annealed sample at 200 °C shows a considerable increase in inter-layer mechanical properties despite a large void content, highlighting the importance of crystallization of bond strength if PEKK 70/30.

Table 2: Tensile Properties vs. void content and crystallinity.

Experimental Set	**Ultimate Tensile Strength (MPa)**	**Young's Modulus (GPa)**	**Void Content**	**Crystallinity degree (estimated)**
ref	5.3±1.4	1.5±0.3	19.4%	<11%
0psi	7.3±0.3	1.7±0.1	20.6%	<11%
20psi	6.7±0.8	1.7±0.1	17.1%	<11%
200psi	8.1±1.2	2.0±0.2	0.4%	<11%
Annealed	53.0±4.4	2.63±0.2	16%	>20%

CONCLUSIONS

Taking all the results into account, several conclusions can be drawn from the experiments conducted in this chapter. Removing all voids and increasing the intimate contact and interdiffusion between layers has a minimal effect on interlaminar bonding strength and stiffness. The results suggest that during the HIP process, even though intimate contact is near maximum, there was likely a relatively low polymer interdiffusion across the interfaces. As expected, a temperature of 165 °C was not high enough to provide an increase in crystallinity in the samples but sufficient to allow polymer flow and interdiffusion. Samples annealed at 200 °C showed the highest modulus and UTS due to enhanced crystallinity, even though the void content was still high. Considering all aspects of the study, an increase in crystallinity is shown to have the highest impact on enhancing interlaminar bonding in FFF PEKK parts. The combination of HIP at 200 psi and annealing at 200 °C can therefore be used as a novel processing technique to significantly enhance mechanical properties of FFF composites, promoting their adoption for end-use applications.

ACKNOWLEDGEMENTS

The authors acknowledge the support by the Office of Naval Research (ONR) Award No. N00014-20-1-2683.

Chapter 3. Additive Manufacturing of Intricate and Robust Parts with Continuous Carbon Fiber Reinforced LM-PAEK

Authors: Nathaniel Heathman, Michael DeLay[*], and Mehran Tehrani

[*]Mantis Composites, San Luis Obispo, CA 93401

Additive manufacturing (AM) offers many advantages over standard manufacturing methods such as design freedom, enabling limited production run components, material savings, and others. In recent years, AM of polymers has advanced to the point of being able to produce components with mechanical properties rivaling metals for end-use applications. One key enabling factor for this advancement has been the emergence of continuous fiber reinforced polymer composites manufactured with AM. In this paper, continuous fiber fused filament fabrication (FFF), is utilized to manufacture specimens from a high-performance semi-crystalline polymer, low-melt polyaryletherketone (LM-PAEK), reinforced with ~37% volume fraction continuous carbon fibers. Specimens were tested to measure their interlaminar shear, flexural, and curved beam strengths. These results are correlated to their micro-structure and polymer crystallinity. Additionally, complex parts were manufactured utilizing the full out-of-plane 3D printing capability of the AM equipment and assessed for homogeneity and build quality. Fiber steering experiments and X-ray computed tomography were used to understand manufacturing defects in resulting parts. Results show record properties for as printed composites, measured interlaminar bonding strength (short beam and curved beam strengths of 60 MPa), flexural strength (943 MPa), porosity (1.63% void volume content), and crystallinity (24%), thus paving the way for the use of LM-PAEK to replace other high-performance polymers in continuous fiber AM. However, extra care should be taken in designing intricate structures requiring fiber steering in load critical sections.

Author Contribution
Nathaniel H: Testing, analysis
Michael D: Fabrication
Mehran T: Supervisor

INTRODUCTION

Fused filament fabrication (FFF) is an additive manufacturing (AM) technique that has been widely adopted and employed in recent years for a variety of applications. While at first its use was predominantly for prototyping and hobbyist applications, material and process advancements have driven the technology towards manufacturing of end use components. One of the main developments in enabling FFF technology is the emergence and widespread adoption of carbon fiber reinforced polymers (CFRP). CFRPs offer a high strength and stiffness to weight ratio. These materials are directly applicable for use in high performance markets such as automotive, energy, and aerospace where high strength, low weight, and high temperature performance are required [25]. By combining CFRPs with AM technology, it becomes possible to leverage AM process benefits to take better advantage of the material traits of CFRPs, enabling several key benefits. Firstly, AM allows for the production of intricate geometries using the full strength of CFRP by optimizing fiber paths and part geometry for specific loading situations, such as steering fibers around fastener holes. This can result in significantly higher performance parts at a fraction of the weight. Secondly, AM can significantly reduce the need for and cost of tooling (molds), by printing molds of reduced volume and complexity in-situ using relatively inexpensive materials. These molds (typically referred to as "support" in AM) require no post finishing.

FFF is an extrusion-based process that employs a heated polymer deposition nozzle, called a hot end, attached to a positioning system to lay down molten thermoplastic or highly viscous slurries following a designated path to form layers [26]. Layers are deposited one on top of another to form a complete three-dimensional shape. FFF printers can utilize either a gantry-based positioning system to deposit one 2-dimensional layer at a time at a given z-axis spacing, or robotic positioning systems to take advantage of placement in all three dimensions at once, called multi-axis or out-of-plane 3D printing

[27]. The thermoplastic material is conventionally supplied to the hot end in the form of a filament with a circular cross section with a consistent diameter, however certain equipment can also utilize thermoplastic pellets fed via a hopper [28]. Traditionally, low-cost low-strength thermoplastics such as acrylonitrile butadiene styrene (ABS), polylactic acid (PLA), and Nylon have been used to manufacture parts via FFF. In recent years, high performance thermoplastics such as polyetheretherketone (PEEK), polyetherketoneketone (PEKK), and polyaryletherketone (PAEK) are being increasingly used , enabling FFF parts for end use and not just prototyping [29]. To push the boundaries of FFF even further, short and continuous fibers have been incorporated into filaments to print composite materials with superior in-plane mechanical properties and enhanced thermal properties [30].

While short fibers have shown to increase stiffness of FFF parts, the real advantage to utilizing composites comes when utilizing continuous fibers [31]. FFF of continuous fiber reinforced polymers takes advantage of fiber lengths that are much higher than the critical fiber length of the composite system, as well as higher fiber volume fractions, due to packing of aligned fibers, to achieve mechanical properties that are an order of magnitude higher than those of their short fiber counterparts [32]. A variety of polymer matrices and fibers can be used in the process, including ABS, PLA, Nylon, and PAEK family of polymers with glass, Kevlar, and carbon fibers [33]. While FFF manufacturing with continuous fibers remains similar to the standard FFF process, there are two key differences. First, there are two main methods of incorporating the continuous fibers, either using filaments that have been pre-impregnated with fibers via a melt impregnation process or combining fibers and polymer together within the hot end right before printing [34], [35]. The second main difference involves the path planning for how the filaments are laid down during each layer. As opposed to conventional FFF, the continuous fiber process must utilize a continuous path along each layer with no starts and stops, due to the necessity to cut the filament at the end of each layer [36], [37]. While this complication may seem detrimental, it in fact opens an opportunity to optimize the design of continuous fiber FFF parts for particular loading situations in a way which increases specific strength and stiffness [14], [38].

As with standard FFF, the continuous fiber process is very dependent on processing parameters to develop ideal properties in the final part. Process speed, layer height and width, as well as nozzle, bed, and chamber temperature are all critical parameters to the FFF process, where each parameter has to be finely tuned for particular materials and printer types [39]. Optimizing these parameters are crucial for the manufacturing of high-performance amorphous and semi-crystalline polymers such as polyetherimide (PEI), polybenzimidazole (PBI), polyphenylene (PPS), and PAEKs where high nozzle, bed, and chamber temperatures along with slow speeds are typically required to consolidate the layers and achieve crystallization, if a semi-crystalline polymer is used [40], [41]. Interlaminar bonding, void development, crystallization in semi-crystalline materials, and fiber alignment and breakage are all significant mechanisms that contribute to the overall strength of parts manufactured via continuous fiber FFF [42].

Interlaminar bonding is the main factor governing the overall strength of continuous fiber FFF parts, especially when subjected to loads that are not in the fiber direction. Compared to thermoforming, where the polymer/fibers are heated uniformly to melting temperature under compressive forces and allowed to cool at a controlled rate, the FFF process deposits molten material on top of an already cooled layer, relying largely on the heat in the material being extruded to remelt the previous layer and bond the two together [43]. The result of this is very high cooling rates and poor interlaminar bonding due to limited time above melting temperatures for the polymer to form intimate contact and interdiffuse, lack of crystallinity, and formation of voids. As soon as the bead is laid on top of the previous layer, heat transfer occurs between the two, causing the previously deposited layer to increase in temperature above glass transition temperature (T_g) and into the melt window where polymer can flow and its chains interdiffuse across the interface to achieve bonding between the layers [29], [44]. The level of bonding is highly dependent on the viscosity of the polymer controlling its flow to form intimate contact, the time at which the two layers are in contact above a threshold temperature, which is typically higher than the T_g , and finally the degree of crystallization at the newly formed interface. Bonding can, therefore, be significantly improved by the use of heated chambers or, in certain cases, preheating of the previous layer [45].

Void development and their presence in a CRFP manufactured via FFF can significantly impact mechanical properties [46]. The appearance of voids is inherent to the FFF process due to stacking of the extruded beads with an elliptical shape that creates diamond or triangular voids at each raster boundary [47]. In FFF of fiber reinforced polymers, many times voids are present within the filament itself and can be passed onto the part [48]. These voids appear in the filament due to a low polymer matrix-fiber adhesion, or inability to fully impregnate the fibers with polymer [49]. Successful attempts to eliminate voids in FFF parts have been made using several different methods. In one study, a significant reduction of inter-raster voids in a neat polymer was made by the adjustment of the extrusion rate, amount of material deposited, to increase the inter-raster pressures allowing the molten material to flow and fill these areas [50]. Another method proposed for void reduction is utilizing a heated compaction roller that follows the hot end to compress the rasters, increasing the intimate contact, hence decreasing the void content [51]. Hot isostatic pressing (HIP) has also been utilized, where a FFF manufactured part is subjected to elevated temperatures and isostatic pressures in a post processing step to remove voids and increase interlayer bonding [19].

When utilizing high performance semi-crystalline polymers, such as those belonging to the PAEK family, the role of the crystallization process becomes significant to the overall part strength. Crystallinity in polymers refers to the self-organization of polymer chains into ordered groupings within the amorphous regions where polymer chains are disorganized. Crystalline regions provide significant improvements to overall strength, stiffness, increased toughness, and wear resistance when compared to their amorphous counterparts [52]. Crystallization occurs above T_g and primarily from melt when polymer chains organize into repeating units called lamella. These lamellae growth and align, forming spherulites or spherical groupings of crystalline polymer chains [5]. Another type of crystallization that can occur above T_g but below the melt temperature, is called cold crystallization, where a material that was cooled too fast to reach full crystallinity can begin to have polymer chains regain mobility and begin to organize when temperature is brought back above T_g [53]. Crystallinity is highly dependent on cooling rate, where mobility of polymer chains to nucleate and grow spherulites is directly related to the time spent in the crystallization window [54]. As in, a slow cooling rate allows ample time for crystalline regions to grow, and a high cooling rate inhibits this process [23]. This is of specific importance to the FFF process due to the inherently high cooling rates observed during material extrusion. While a fully crystalline structure is preferred, evidence shows it is very difficult to achieve during the FFF process, however careful control of processing and environmental parameters can help to achieve complete crystallization. Another important aspect of crystallization during FFF is ensuring sufficient time for the crystals in the filament to melt and then preventing premature crystallization before interdiffusion of polymer chains across newly formed interfaces. To this end, engineering polymers with specific crystallization behaviors are necessary to achieve strong bonding in FFF.

FFF of continuous fiber filaments presents a specific challenge of ensuring proper fiber alignment and minimizing fiber breakage while the material is being deposited. During printing, fibers are aligned in the direction of travel of the print head. Due to the fixed orientation of the deposition nozzle, fibers naturally resist a change in direction during the print, which can lead to twists, overlaps, and void formation between fibers any time the print direction is altered. Considering the main benefit to AM is the design freedom enabled by the process, it is important to know exactly what occurs to fibers during direction changes. In a study, polyamide 6-1 continuous carbon fiber samples were prepared at various radii and angles to inspect the behavior of the fibers under different curvatures [55]. Their findings show that while fibers are aligned nicely with minimal voids at high radii, when decreasing the radius, many print defects occur, including path errors, fiber twisting, folding, and misalignment, along with the formation of voids [55]. Considering these defects are inherent with the process, it is important to note their occurrence and be able to path plan to mitigate their occurrence, ensuring the highest strength possible in the manufactured parts.

With the development of off-the-shelf printers suited for FFF of continuous fiber filaments by a variety of firms, such as Markforged, 9T labs, Desktop Metal, Anisoprint, Arevo, and others, mechanical properties for lower grade materials are beginning to be well documented [56], [57], [58], [59], [60]. However, within the scope of the semicrystalline high-performance polymer field, much less research has been conducted. In one study, van de Werken et al. sought to investigate the mechanical and thermal properties, along with microstructure of AS4C continuous carbon fiber PEEK with a 42% fiber volume fraction (V_f), manufactured by FFF, in as-printed form as well as after a HIP post processing procedure [19]. Results show as-printed samples achieved a short beam shear (SBS) strength of 27 ± 2 MPa, flexural strength of 834 ± 126 MPa, with a void content of 10%, and a degree of crystallinity of 22%. When subjected to HIP at 200 psi and 250 ˚C, SBS was increased to 35 ± 6 MPa, flexural strength to 1221 ± 61 MPa, void content decreased to 5%, and the degree of crystallinity increased slightly to 23 %. Kuba et al. studied the effect of melt viscosity on void content and interlaminar tensile strength of specimens manufactured from three different grades of PEEK by continuous fiber FFF [61]. Outcomes of testing showed the lower melt viscosity filament reduced the void content and increased interlaminar tensile strength considerably when compared to the standard viscosity material, with void content being 8.0% compared to 16% respectively, and an increase of 117% in interlaminar tensile strength. These results provide significant evidence that reducing melt viscosity in these semi-crystalline material helps improve bonding strength and reducing void content. Meng et al. employed a laser preheating technique in the continuous fiber FFF process to enhance interlaminar bonding and tested its effectiveness by manufacturing and testing two viscosity grades of PEEK in a 38 wt.% carbon fiber filament [45]. With laser preheating enabled, a maximum SBS strength, flexural strength, and flexural modulus of 36 MPa, 480 MPa, and 37 GPa, respectively, were achieved. While these studies show a variation in flexural strength and void content, the low SBS values remain consistent, and the topic of low interlaminar bonding is extensively discussed. The proposed conclusion is that PEEK suffers from too high of a melt viscosity to enable sufficient flow, and polymer chain mobility and diffusion across interfaces to properly bond each layer in the continuous fiber FFF process. It could also be the case that the fast cooling rates result in premature crystallization, occurring prior to interdiffusion of polymers across interfaces.

The goal of this research is to utilize a new high-performance semi-crystalline material from the PAEK family, denoted as low melt PAEK (LM-PAEK), to manufacture specimens and analyze their mechanical, thermal, and microstructural properties. LM-

PAEK, while providing similar strength, high temperature performance, chemical and wear resistance to PEEK, offers a lower melting temperature and viscosity, which in turn should help to alleviate the interlaminar bonding challenges as seen in previous research of continuous fiber FFF of PEEK. In this paper, samples are manufactured by continuous fiber FFF, with half being post process annealed, then tested to assess their interlaminar bonding strength, flexural strength, interlaminar tensile strength, void content, microstructure, fiber alignment, and crystallinity. The results hope to provide insight into the properties achieved with this new material in the continuous fiber FFF process and drive advancement of the technology beyond previous understandings developed with standard PEEK.

EXPERIMENTATION

Material and Fabrication

The material used for sample fabrication is carbon fiber LM-PAEK continuous fiber filament. The filament comprises AS4C carbon fiber and Victrex AE250 LM-PAEK polymer with a resulting 37% carbon fiber volume fraction (measured via micro computed tomography of the filament) and a 0.8 mm filament diameter. LM-PAEK is a high performance semi-crystalline polymer that belongs to the PAEK grouping of polymers and is thus similar to PEEK and PEKK. LM-PAEK has comparable mechanical and thermal properties, with high chemical resistance, but provides a lower processing temperature thanks to a reorganization of the polymer chains into co-polymer groupings that brings processing temperature down 60 ˚C lower than PEEK and PEKK [62].

All samples were fabricated with a 5-axis continuous fiber FFF printer developed by Mantis Composites. Processing parameters of 10 mm/s speed, extruder temperature of 340 ˚C, and a bed temperature of 200 ˚C were utilized. Three types of samples were fabricated per ASTM standards for analysis, short beam strength (SBS), curved beam strength (CBS), and flexural. Samples were also prepared at a single layer height with radii varying between 1.25 mm and 10 cm to assess fiber alignment and breakage in corners. Lastly, a complex 3-dimensional geometry part was manufactured utilizing the 5-axis capability of the printer and analyzed for defects and voids. Path planning was optimized to ensure a constant fiber direction was maintained along the path of the part. SBS and flexural samples were fabricated oversize and machined to correct size afterwards. After fabrication, selected SBS and flexural samples were subjected to annealing and compared to non-annealed reference coupons. Annealing consisted of heating samples to 160 ˚C from room temperature at a 3 ˚C/min rate, holding for 30 minutes then heating to 210 ˚C at a 3 ˚C/min rate and again holding for 1 hour, after which they were allowed to cool to room temperature in the oven at an uncontrolled rate.

Characterization

Mechanical property characterization was carried out to test for short beam strength (SBS) corresponding to interlaminar shear strength (ILSS), curved beam strength (CBS) corresponding to interlaminar tensile strength (ILTS), and flexural strength and modulus. SBS samples were fabricated and tested following the ASTM D2344, CBS samples were fabricated and tested following the ASTM D6415, and flexural samples were fabricated and tested following the ASTM D7264. Figure 7 provides illustrations of all ASTM tests carried out. Thermal properties were evaluated via dynamic scanning calorimetry (DSC) to determine the crystallinity of the samples. DSC tests were carried out in multiple regions within each sample to form an understanding of how crystallinity develops during the printing process. A heating rate of 10 K/min was used for all DSC tests. Cross-sectional microscopy and micro computed tomography (µCT) were performed to analyze the microstructure of the filament and samples for fiber distribution, defects, and void content.

Specifically, the varying radius samples were scanned with µCT to analyze fiber breakage and twisting as well as void development in corners.

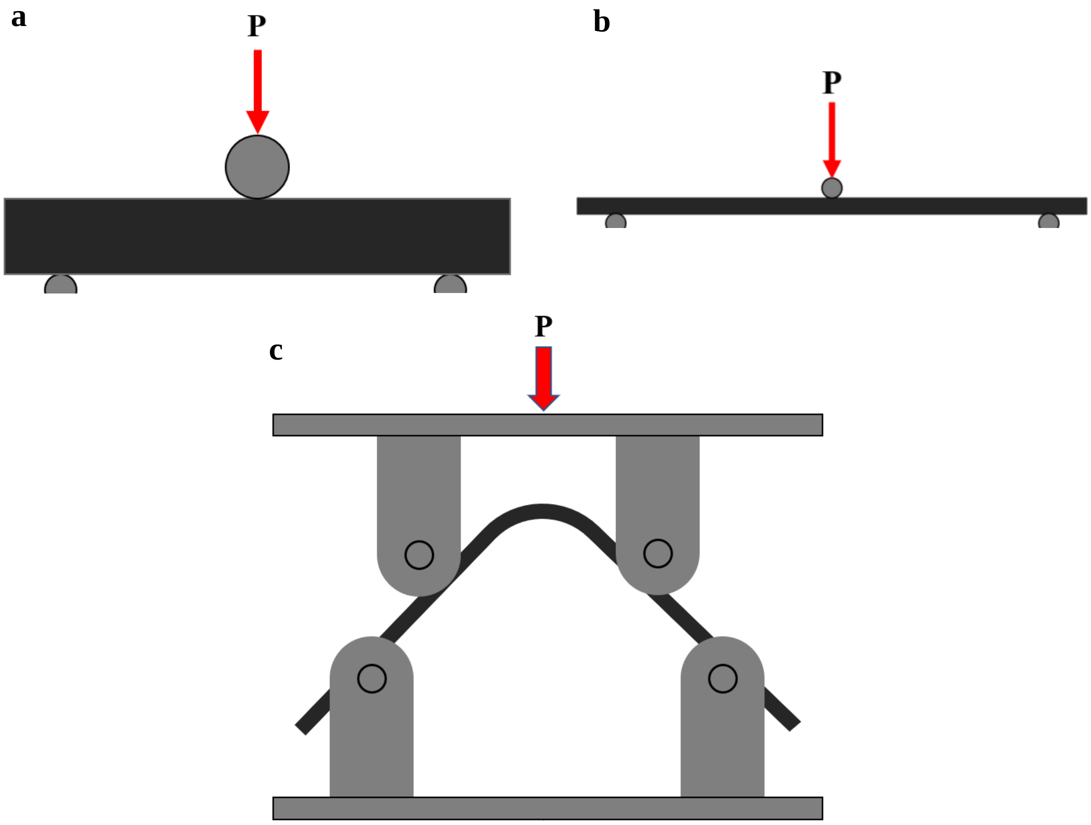

Figure 7: ASTM mechanical property tests, a) Short beam shear, b) Flexural, c) Curved beam strength.

RESULTS AND DISCUSSIONS

Results for all tests are shown in Table 3 and representative loading curves are show in Figure 8. Analysis of the mechanical testing results show multiple interesting phenomena. SBS is a qualitative measure of interlaminar shear strength and is commonly used to assess bonding (consolidation) degree in additively manufactured composites.

Comparing SBS values to others, the 60 MPa SBS strength achieved here, is significantly higher than maximum SBS values of around 35 MPa found in other studies of continuous fiber FFF PEEK parts [45], [19]. However, strength values are only ~60% of compression molded parts, with a reported SBS strength ~95 MPa [63]. While SBS values are lower than those of compression molded samples, 60 MPa is considered quite high for a part manufactured via FFF where intimate contact and interdiffusion between layers suffer due to high cooling rates and dissimilar layer temperatures during deposition.

Flexural testing is another common test to assess intra-laminar properties of composites [64]. Flexural failure is typically fiber compression under a mixed stress mode. A mean flexural strength of 943 MPa was achieved for the tested coupons, which is again higher than any as printed result found in previous studies [19]. Flexural modulus is 84 GPa, which is expected following the tule of mixture; 37% fiber volume fraction and standard modulus carbon fibers (modulus of 230 GPa).

The CBS method utilizes a curved beam specimen comprised of two straight legs joined by a 90° bend with an inner radius of 6.4 mm. When a force is applied through a 4 point loading fixture, it induces an out-of-plane tensile stress within the curved region of the specimen through its thickness. Curved beam testing results provide a maximum ILTS of 62 MPa. With ILTS values closely resembling the SBS ones, the conclusion can be drawn that these parts are no more susceptible to failure due to pure tensile loading than to shear loading. Results from testing annealed samples show no change in mechanical properties within their standard deviation for either SBS or flexural samples. To further understand the measured mechanical properties detailed characterization of failure modes, micro-structure, and polymer crystallinity are conducted.

Table 3: Mechanical property results

Property	Value
Flexural test, reference	
Strength (MPa)	943±24
Maximum Strain (%)	1.1±0.0
Chord Modulus (GPa)	84±1
Flexural test, annealed	
Strength (MPa)	930±44
Maximum Strain (%)	1.2±0.1
Chord Modulus (GPa)	86±2
Short beam shear, reference	
SBS strength (MPa)	60±3
Short beam shear, annealed	
SBS strength (MPa)	60±3
Curved Beam Test	
Interlaminar Tensile Strength (MPa)	62±7

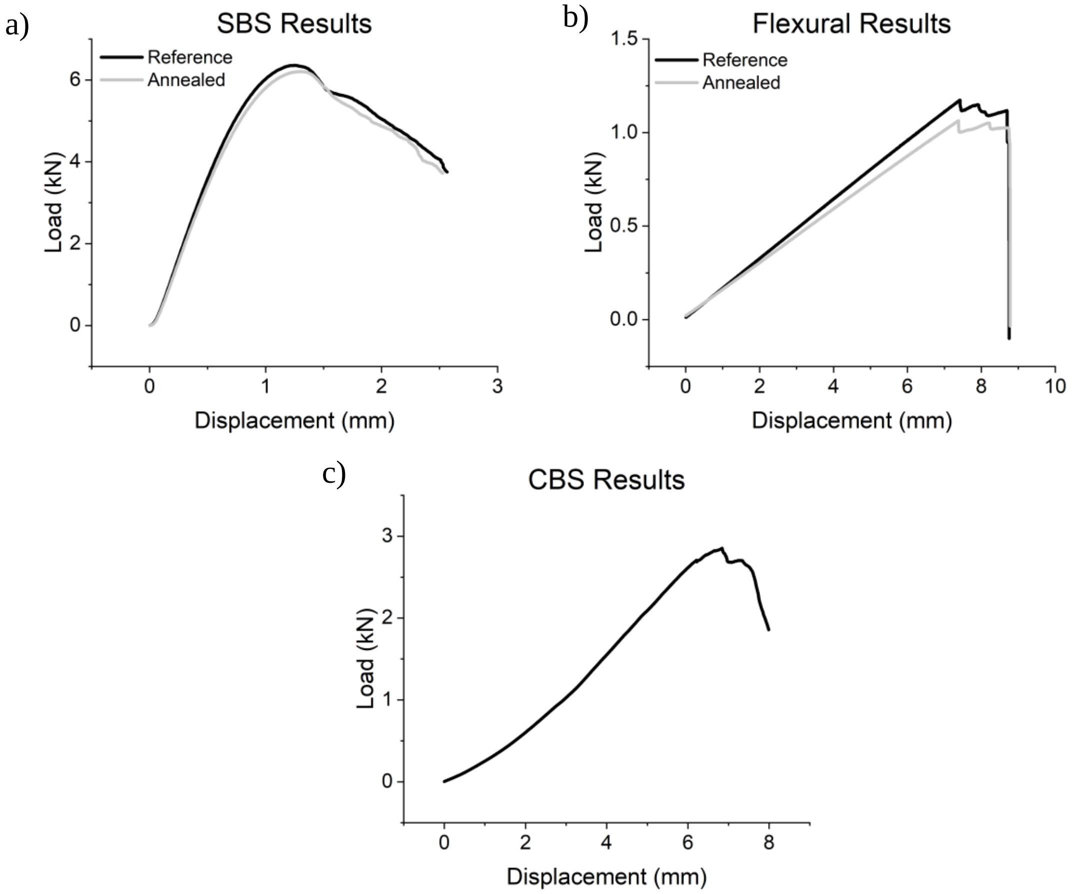

Figure 8: Loading-displacement curves for a) SBS, b) Flexural, and c) CBS tests.

Micro computed tomography was conducted on a SBS coupon, CBS radius section, and samples with different radii. An as printed tomograph of a reference SBS coupon is shown in Figure 9a. A 1.63% void volume content was measured by analyzing the μCT slices. Voids are predominately located at filament interfaces and travel longitudinally along the interfaces for long distances within the sample. These voids were segmented during μCT analysis from the sample and reconstructed in three dimensions to demonstrate how they are located within the sample, as shown Figure 9b. Shape and location of voids here is much different than those observed in FFF of un-reinforced thermoplastics. During the FFF process, diamond shaped voids form between individual rasters due to the oval shape of deposited filament. In the continuous fiber FFF process studied here, voids appear at random predominately on the raster boundaries, with a small portion of voids appearing within the rasters themselves. This suggests that voids appear at interfaces due to incomplete intimate contact (lack of flow and interdiffusion), which in turn is caused by a lack of pressure to facilitate polymer flow, whereas the voids within the rasters could be from the raw filament. Compared to previous studies on continuous fiber-PEEK FFF, the measured void content is significantly lower, 1.6% compared to 10% in one study and 8% in another [19], [61]. Considering the similar manner of fabrication for the aforementioned PEEK specimens, the lower void content presented here suggests the lower viscosity at melt for LM-PAEK is the driving factor for the low void content. It should be noted that while the void content is low, they are elongated and present at most raster-raster interfaces, reducing the interlaminar strength significantly; SBS is 60% of its maximum value.

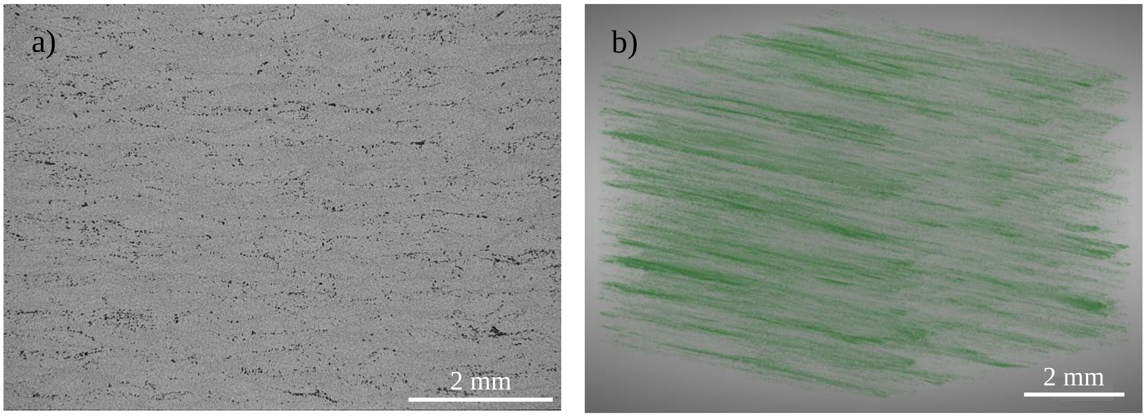

Figure 9: a) µCT tomograph of a reference SBS coupon, b) µCT reconstruction of voids in a SBS coupon.

DSC was performed on the raw filament, as well as SBS and CBS samples to inspect the crystallinity and its development during the manufacturing, by assessing it through samples' height. Figure 10a shows DSC curves for the filament in as delivered, heated to melt and cooled at 500 K/min (denoted as fast cooled), and heated to melt and cooled at 1 K/min (denoted as slow cooled) forms. The as delivered filament showed a 7% crystallinity a 5% minimum with fast cooling, and a 25% maximum with slow cooling. These values are typical of carbon fiber LM-PAEK, as measured by others [65], [66]. All samples exhibit a T_g of ~150 °C. Slow-cooled samples demonstrate a slightly higher melting temperature compared to other two samples. All samples melt below the processing nozzle temperature of 340 °C used here. Both the filament as fast-cooled samples exhibit cold-crystallization below 200 °C, which is ideal for FFF. In FFF, the cooling rate from the melt is quite rapid (hundreds of degrees per second) [65], [19]. The use of a heated bed at 200 °C, as employed in this study, enables cold-crystallization to occur within relatively short samples. However, taller samples are expected to cool at similar rates but do not remain near 200 °C for an extended period., hence may not achieve a large degree of cold-crystallization.

Degree of crystallization values measured from several locations in different specimens are summarized in Table 4. SBS samples, curves provided in Figure 10b, show a near maximum crystallinity of ~24%, developed at the bottom and middle of the sample but a sharp drop off at the surface of the sample, only 7%. The annealed samples on the other hand have a consistent crystallinity of ~24% through the entire height of the sample. Given that the SBS samples are 6 mm thick, printing bed effects are only noticeable within a few millimeters, which helps the deposited rasters to crystallize by sustaining their temperatures for sufficient durations within the cold-crystallization window. Regardless, the simple annealing performed results in relatively high crystallinity values throughout all samples.

Similar to the SBS samples, the CBS ones (printed on their side) have a relatively high crystallinity near the bottom few millimeters but start to drop to ~ 11% at the middle and top of the sample, 12.5 mm and 25 mm from the print bed, respectively. As iterated earlier, when each sample is printed, the heat from the deposition of filament above or alongside any given section of filament can raise the temperature enough to allow for further cold-crystallization of the previously deposited material. The repeated heating effect causes cold crystallization of the surrounding material, subsequently raising the overall crystallinity of the part.

An interesting phenomenon shown in the DSC curves for SBS samples, Figure 10b, is the double melting curve. In previous research it is shown that this is a result of isothermal holds above glass transition temperature where there is a primary crystallization process where spherulitic entities are formed, and a secondary process, where interlamellar crystalline structures grow. It is theorized that the double melting curves appear in DSC at 20 ± 10 ˚C above the isothermal hold temperature, which is 200 ˚C for the as printed parts and 210 ˚C for the annealed parts [5]. Results from DSC analysis for as printed samples show the capability to achieve near maximum crystallinity at the bottom surface of the part, but crystallinity decreases as the distance from the print bed increases. However, with annealing it is possible to achieve a maximum crystallinity of ~ 25% throughout the sample. In general, it appears that a post-annealing step is required for samples taller than 2mm. Required annealing temperatures are lower than the heat deflection temperature of the 0˚ coupons and sample deformations are not expected, yet some residual stresses may be eliminated.

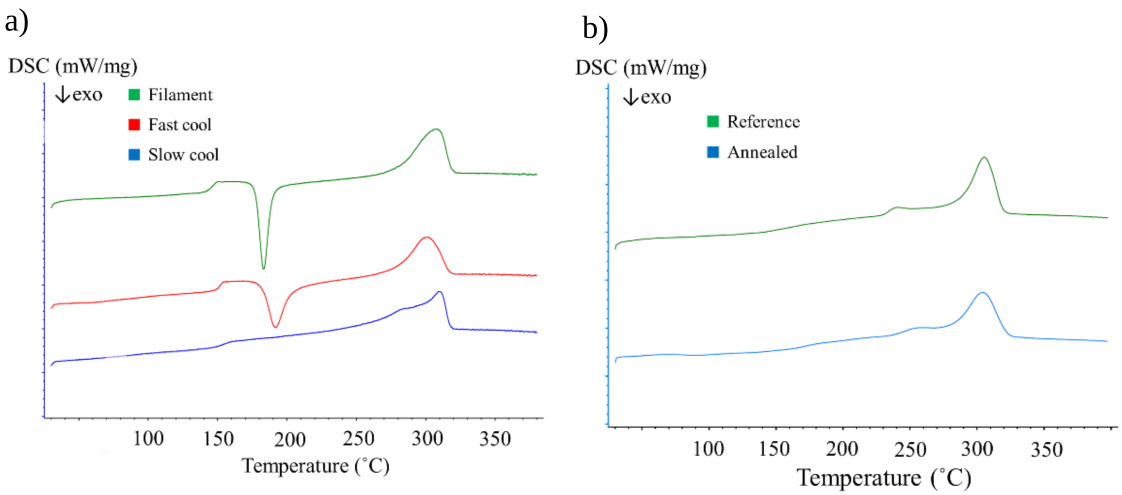

Figure 10: a) DSC curves for the as received filament, melted and fast cooled, and melted and slow cooled samples, b) DSC curves for reference and annealed samples.

Table 4: Crystallinity values for different samples at multiple locations.

Sample	***Crystallinity (%)***
SBS Reference Bottom	24%
SBS Reference Middle	24%
SBS Reference Top	7%
SBS Annealed Bottom	24%
SBS Annealed Top	24%
CBS Bottom	20%
CBS Middle	11%
CBS Top	11%

Fractography was performed to compare failure types in tested samples and traditional laminated composites. Figure 11a shows a side profile a reference SBS sample after testing. The observed failure mode for all SBS, reference and annealed, samples is inelastic deformation with a small amount of crushing under the loading roller, shown in

Figure 11a. This failure mode is representative of a large amount of plastic deformation without apparent delamination. Inspection of the loading curves in

Figure 8 shows clear plastic deformation and no sharp drop offs in loading that are indicative of delamination. SBS failure behavior is different than traditional samples where significant shear failure and delamination occurs, evident by the appearance of a few cracks near the middle of the sample. The presence of several cracks at interlaminar regions, Figure 9a-b, could be the reason for the gradual (several smaller and internal shear delaminations) and different failure behavior in FFF samples.

Flexural samples show a typical fracture surface with clearly defined tensile and compression stress states as shown in Figure 11b where a sharp jagged fracture surface is indicative of tensile failure and smooth flat fracture surface is telling of compression loading. No delamination was observed in flexural samples. CBS test in the 4-point bending fixture is meant to introduce tensile stresses in between plies in the bent section, but in reality, it introduces complex 3D stresses. Upon inspection of the fractured CBS sample, the in-plane fracture surface shown in Figure 11c has clear tensile stress induced fractures along the fiber paths. However, inspection of the out of plane surface, shown in Figure 11d, has delamination and buckling between layers. While this phenomenon is unexplained in the ASTM standard, it can be theorized that the delamination is a result of the less than ideal interlaminar bonding and fiber misalignments in the 6.4 mm radius bend. It is also possible that variation in local matrix properties caused by crystallinity changes throughout the sample contributed to the delamination; the CBS sample was not post-annealed, hence achieved a low crystallinity in the regions that are shown as failed in in Figure 11d.

SEM imaging of the SBS and flexural samples was conducted to inspect the fiber matrix interfaces on fracture surfaces. Due to the inelastic deformation failure of the SBS samples, to image the interfaces, a crack was initiated at the end of the sample with a razor blade and split manually. This fracture surface is shown in Figure 12a, where the most notable feature is the remnant of the polymer matrix on the fibers. Figure 12b shows a magnified area of the flexural sample under tensile stress. Analysis of this region shows multiple fibers bundled together with polymer matrix, a small number of individual fibers pulled out of the bundles, and overall, very few clean fibers. Figure 12c shows a magnified area of the flexural sample under compression failure. In this area, the majority of fibers fracture cleanly from the surface of the polymer matrix, however there are notable regions of shear fracture and clean fibers. Overall, inspection of the fracture surface via SEM imaging shows significant evidence of a strong matrix interphase region, which is a major factor in developing high interlaminar shear strength.

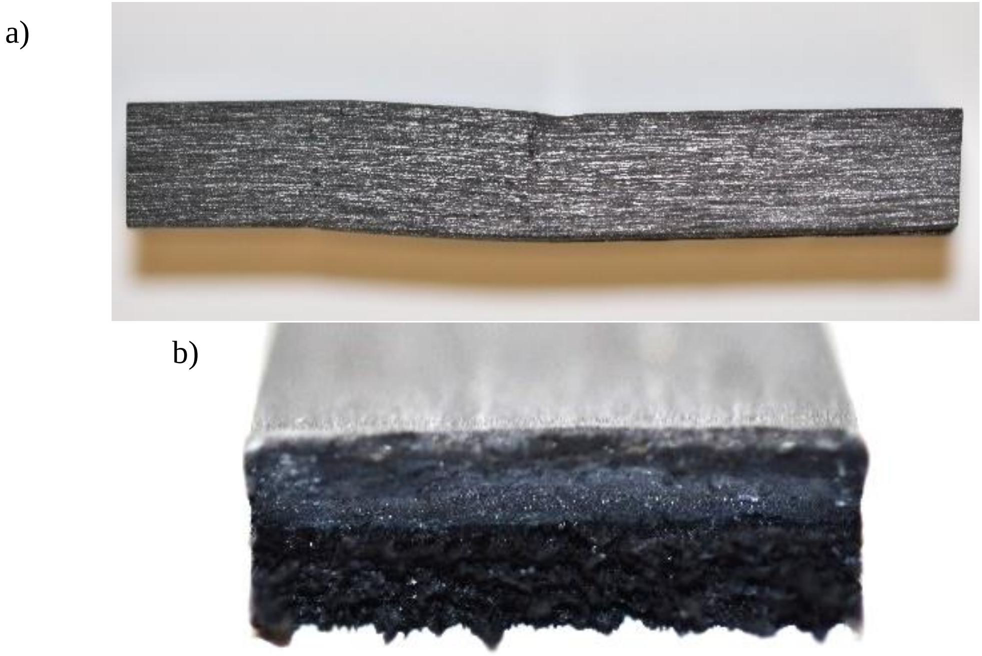

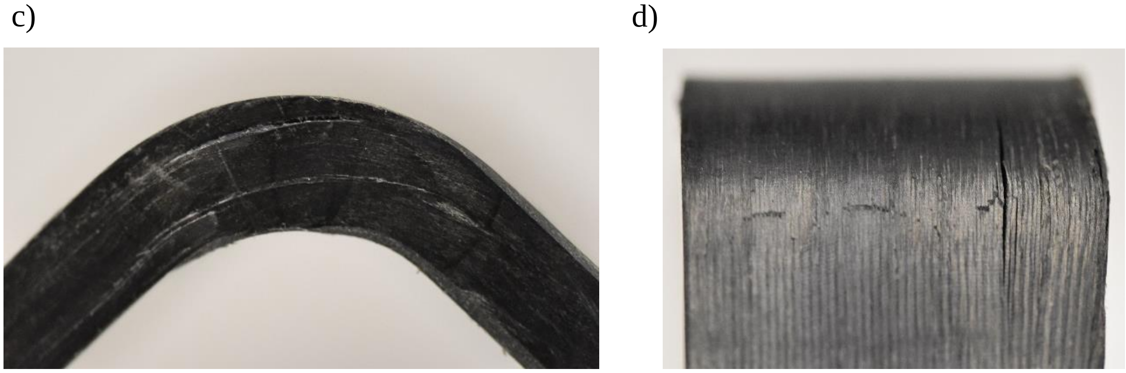

Figure 11: a) SBS coupon after testing showing inelastic deformation and buckling, b) Flexural test sample fracture surface, c) CBS fracture in plane, d) CBS fracture out of plane.

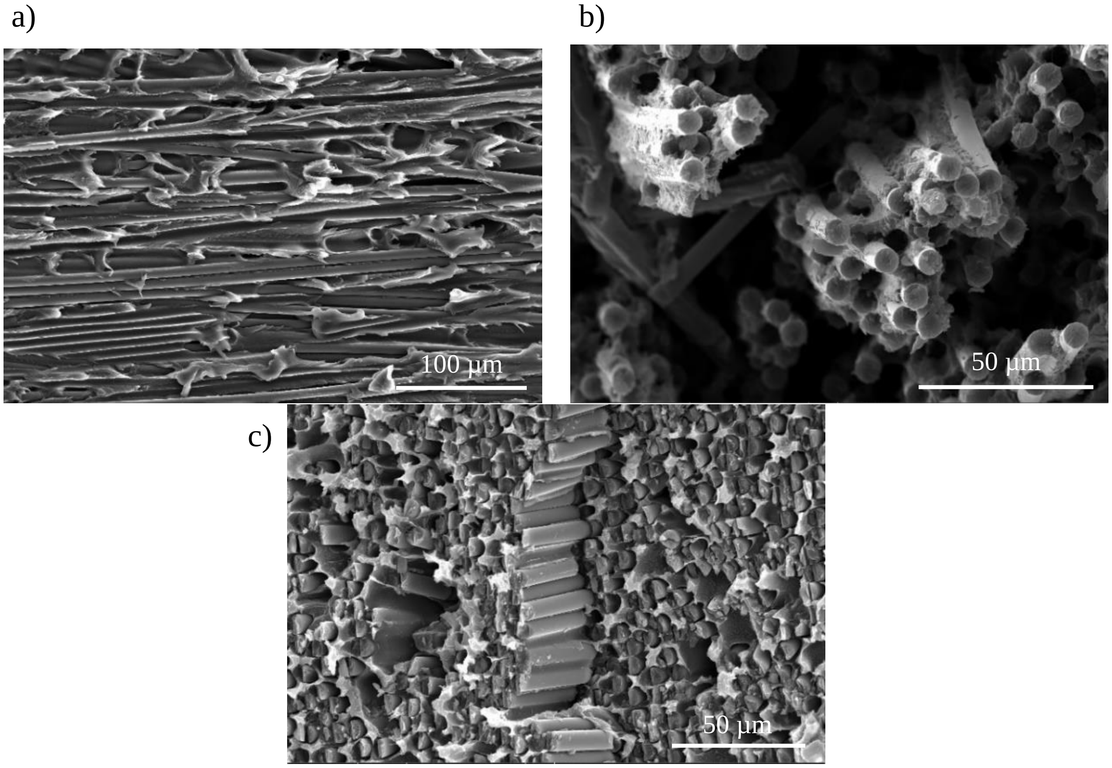

Figure 12: Fracture surface SEM images, a) SBS coupon fracture surface, b) Flexural test sample, tensile region, c) Flexural test sample compression region.

Steering is recognized for its tendency to cause fiber misalignments, particularly in automated fiber placement (AFP) of tapes. While steering is commonly employed in 3D printing, our current understanding of this process remains limited. Filament steering is considered more suitable for 3D printing compared to tapes used in AFP, mainly due to the round shape of filaments and their lower fiber volume fraction, allowing for better fiber spreading and movement. Moreover, the observed failure behavior in the CBS test underscores the importance of gaining further insight into the steering process. In pursuit of this understanding, 3D µCT reconstructions of various radii samples as well as a tomographic image of the CBS sample were generated, see Figure 13.

Figure 13a shows the tomographic image of a printed filament at a radius of 1.25 cm, minimum which can be printed, where the fiber path is steering to align directly next to the previous path. It is clear that the fibers fold over one another to round the corner as opposed to being steered in the previous orientation. As the radius declines from 1000 mm to 1.25 mm, Figure 13a-f, common trends are that the fibers are unable to conform to the steering angle and tend to fold over and twist as opposed to following the programmed path. This trend is even more evident in the interior of the curved regions, where the radius is smaller than the exterior. This phenomenon can be explained by the forces experienced in the individual filaments during deposition. If a line was drawn in the middle of curved filament, the inside portion would be under compression, where the outside portion would be under tension [55]. The compressive force causes fibers to buckle where the tensile forces cause the fibers to fold over one another. One possible solution to this issue is the development of a rotating deposition nozzle that manually twists the filament during deposition in corners to relieve these stresses [67] The main downside of this phenomenon is that it introduces voids in the twisted regions, as evident in Figure 13e. However, based upon CBS testing results, where ILTS is almost identical to ILSS, it is unclear if the presence of these voids significantly impacts the strength of the sample in the through-the-thickness direction. Regardless, it is important to make note that this will happen in all steered corners while printing and can act as stress concentration.

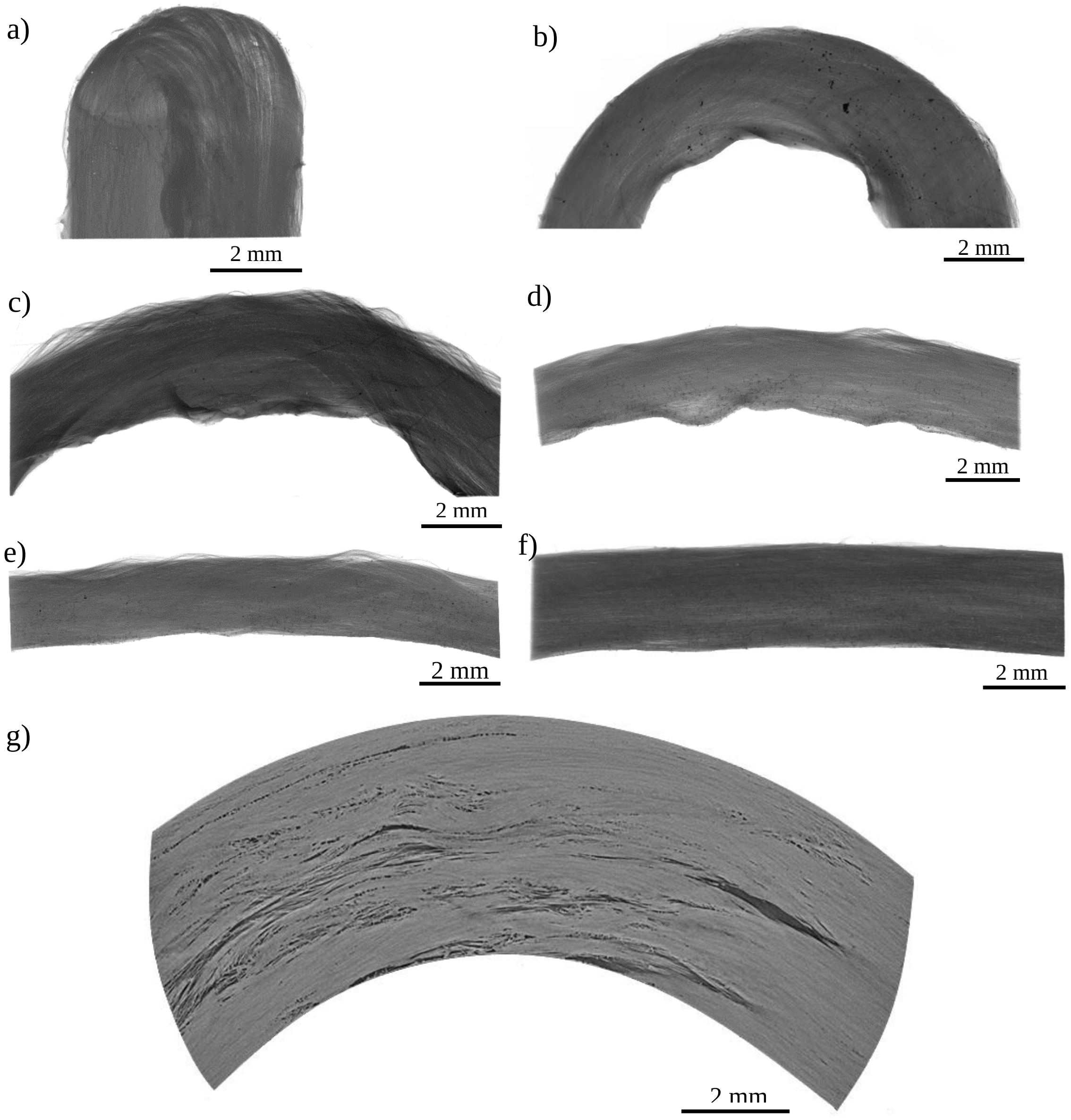

Figure 13: µCT tomographs of steered fibers a) 1.25 mm radius, b) 50 mm radius, c) 100 mm radius, d) 200 mm radius, e) 500 mm radius, f) 1000 mm radius, and g) CBS sample.

To highlight the out-of-plane printing capability of the continuous fiber AM process, a complex 3-dimensional bracket was manufactured and analyzed for overall quality. Figure 14a-b show the nozzle path and orientation for the bracket shown in Figure 14c. The bracket was printed on a heated metal mold, following a path that formed a single continuous loop. The orientation of the nozzle was maintained perpendicular to the mold's surface. Processing parameters such as speed and temperature are varied depending on the location in the path to optimize the part quality. Given the varying process parameters and nozzle travel orientation during the print, part properties can vary from one location to the next. It is critical to analyze and note any variations in quality.

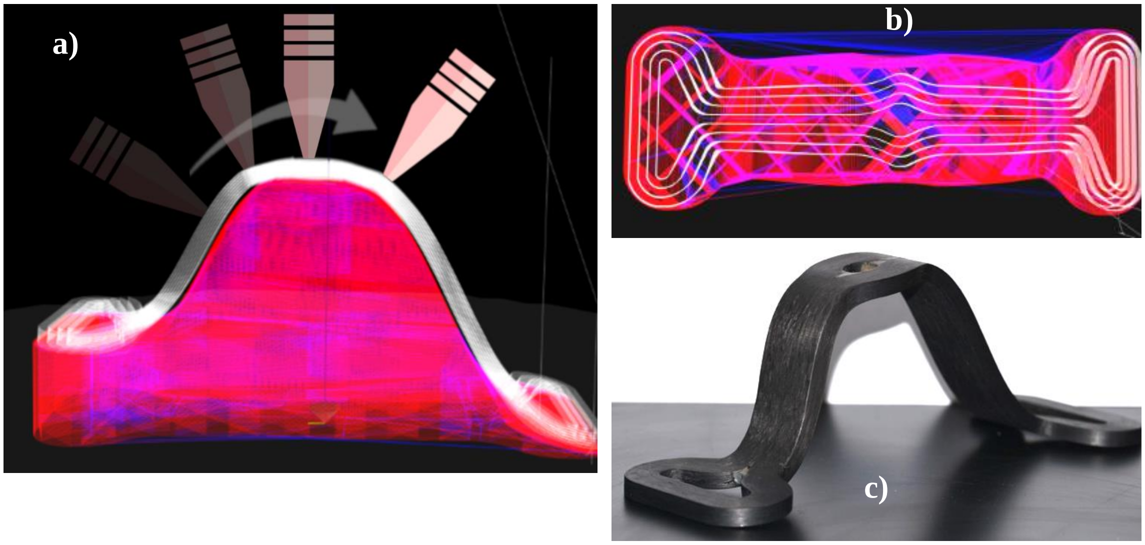

Figure 14: a) Conformal out-of-plane AM on a mold, b) top view of the asymmetrical bracket showing planned fiber paths, and c) final printed part.

The bracket was imaged with µCT in two regions of importance to view void development and defects. Figure 15a provides an image of the bracket, with boxes highlighting the two areas that were scanned. Figure 15b shows a cross sectional tomograph of the corner region. In this region the presence of voids is increased where the fibers are steered around the corner when compared to the straight regions. Figure 15c provides an image containing voids reconstructed, represented in green. A void analysis of the steered section compared to the straight section yields an 8.8% void content in the corner, compared to 5.2% when the fibers are oriented in a straight line; note that the SBS coupons contained less than 2% void. These results validate the previous evidence of an increased void content in the corner regions. Figure 15d and Figure 15e provides cross sectional tomographs of the slope region. Notable findings include the large presence of voids in this region, concentrated at the bottom of the sample where fibers were placed on the mold. Void analysis of the entire slope section yielded a 5% void content. However, when looking at Figure 15e, the difference in void content between the left and the right of the slope region can be seen. This is due to the different paths of travel on the two sides, where in the left region the filament was deposited in travelling down the slope, compared to the right region where the filament was deposited traveling up the slope. The red box located in Figure 15e, highlights an area with a significantly large void volume content. This defect is located in the area where filament was travelling down the slope. It can be theorized that while the nozzle travels down an incline, such as in the left side of Figure 15e, the orientation of travel corresponding to mold angle causes a natural lifting effect on the deposited filament, producing an increased void content or large defects. Results from µCT analysis of this bracket offer valuable insights into the quality of complex parts produced via continuous fiber FFF. Designers need to consider all aspects of the filament path and travel orientation to minimize the occurrence of defects in a part.

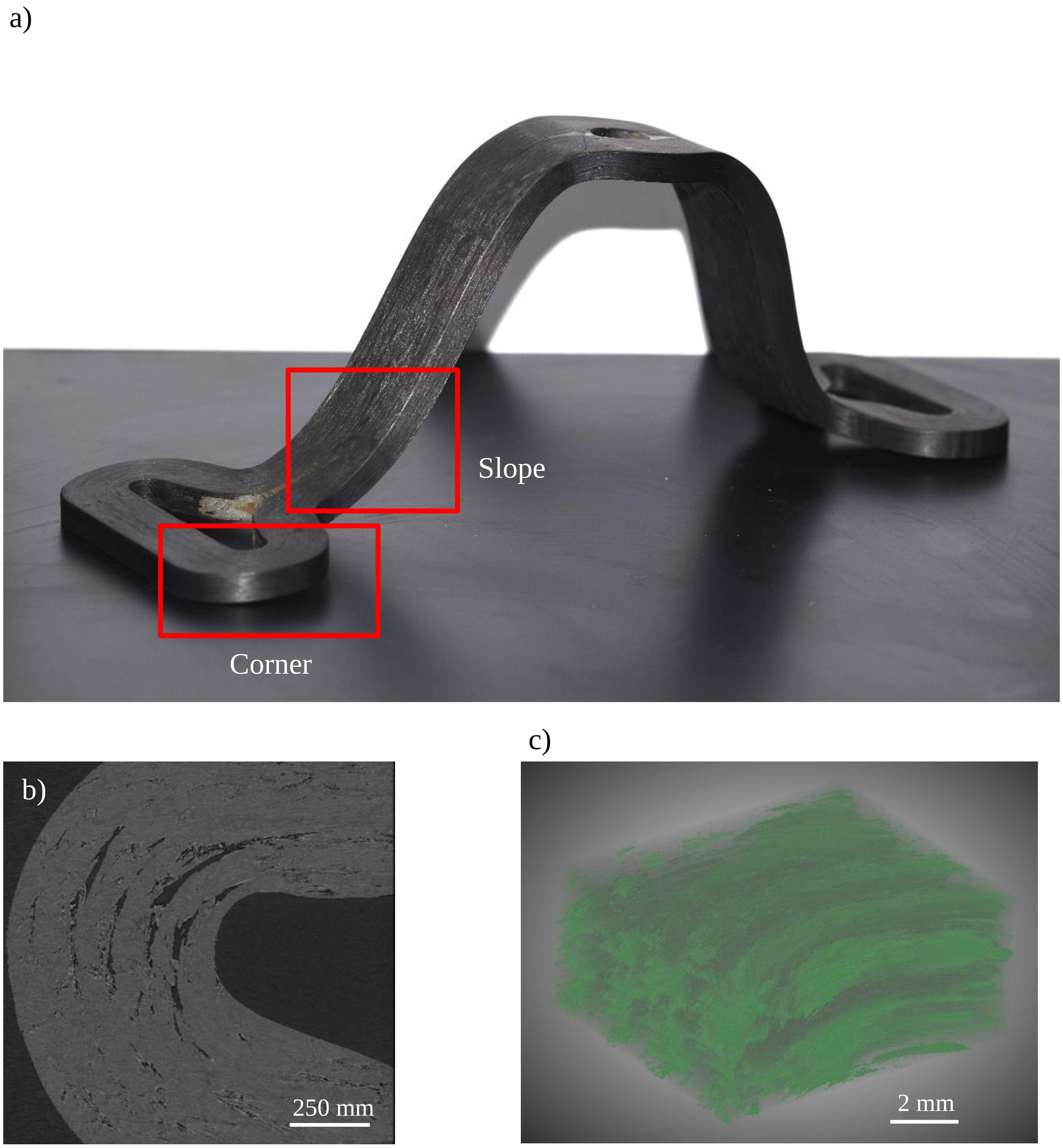
a)
Slope
Corner
c)
b)
250 mm
2 mm

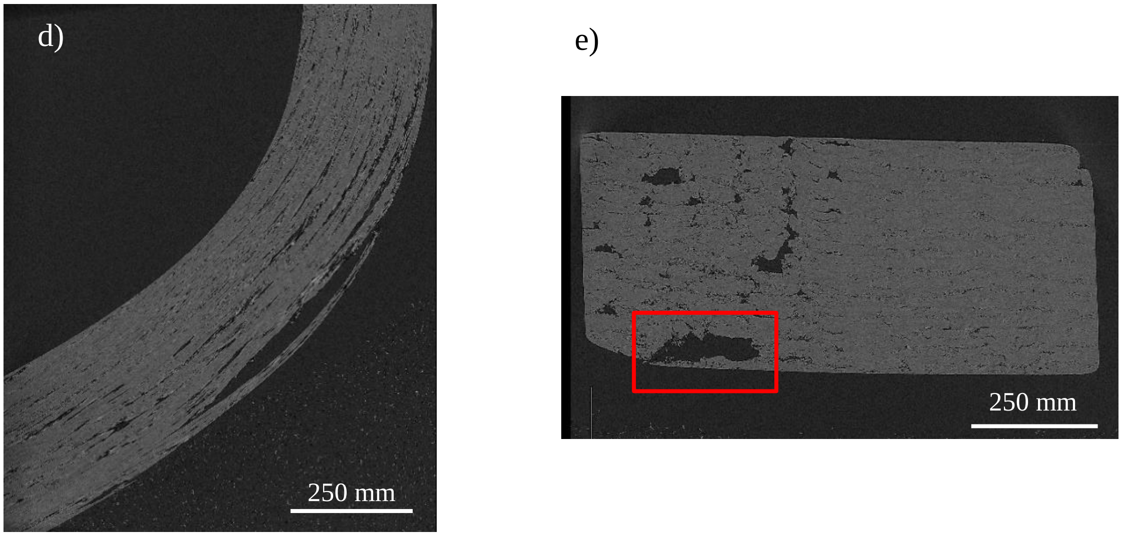

Figure 15: µCT analysis of bracket, a) Bracket, red boxes highlight scanned sections, b) Tomograph of corner region, c) Void reconstruction in corner region, d) Void reconstruction in slope, parallel to fibers, e) Void reconstruction in slope, perpendicular to fibers.

SUMMARY AND CONCLUSIONS

In this study, various standard and complex-shaped specimens were fabricated using continuous fiber FFF and a newly developed semi-crystalline high-performance polymer called LM-PAEK. Analysis of the samples' mechanical properties, thermal properties, and microstructure revealed that LM-PAEK is well-suited for FFF and outperforms other high-performance polymers in terms of part quality and performance.

Mechanical testing demonstrated exceptional interlaminar shear strength (via SBS) and flexural strength of 60 MPa and 943 MPa, respectively, for the as-printed coupons. These samples also exhibited an interlaminar tensile strength (via CBS) of 62 MPa. Void analysis of a printed flat coupon revealed a void volume content of 1.6%, primarily concentrated along fiber interfaces. Crystallinity assessment via DSC indicated that the filament was delivered with 7% crystallinity, while a maximum crystallinity of 25% could be achieved through slow cooling from the melt. DSC testing of the samples themselves demonstrated near-maximum crystallinity at the bottom of the sample, close to the heated bed, which decreased with increasing thickness. It was demonstrated that near-full crystallization of a part could be achieved through a relatively low-temperature (210 ˚C) and quick post-annealing step.

Analysis of µCT data obtained from single deposited filaments showed significant buckling, twisting, and folding of fibers when steered around sharp corners. These defects resulted in the formation of large voids in parts with curved shapes where the filaments had to conform. Overall, the presented results highlight the ability to manufacture intricate parts with continuous fiber LM-PAEK via FFF with enhanced interlaminar bonding and reduced void content compared to their PEEK counterparts. It can be theorized that the lower processing temperature and viscosity provided by LM-PAEK significantly aid in the interlaminar bonding process. In conclusion, LM-PAEK should be considered the new standard for use in continuous fiber FFF of high-performance, semi-crystalline polymers, based on the findings of this study.

ACKNOWLEDGEMENTS

Authors are grateful for the research support provided by the Air Force Research Laboratory (AFRL) award no. FA8649-21-P-0122 and the Air Force Office of Scientific Research (AFOSR) award no. FA9550-21-1-0066.

Chapter 4. AFP Manufacturing Cell Construction

A laser-assisted automated fiber placement. (AFP) manufacturing cell was designed, developed, and constructed at UT Austin. A single tow AFP tool was selected and affixed to a KUKA 6-axis robotic positioning system. The tool was then modified and combined with a 980 nm wavelength 600W laser system to perform in-situ consolidation of thermoplastic composite (TPC) tapes. A heated layup tool was also developed and constructed to provide an optimal layup surface for manufacturing of TPCs. The entire system was contained in a laser radiation safe cage and a control center was setup outside of the containment cell, so that the AFP process could be performed remotely and monitored via cameras. This chapter provides a comprehensive review of the process of critical component selection and construction of the manufacturing cell.

COMPONENT SELECTION

The AFP process, as described previously, is an additive manufacturing process that involves depositing unidirectional prepreg or towpreg tapes with a specialized toolhead affixed to a robotic positioning system. One of the major projects undertaken in the course of research was the development and construction of an in-situ consolidation AFP of TPCs (ICAT) cell for advancing the TPC manufacturing technology. There are several components required in the development of an ICAT cell, those are, a robotic positioning system, AFP end effector, towpreg heating system, layup tool, containment system, and human interface system. Each component subsystem was individually analyzed, and selections were made to best fit the requirements. All components were assembled into a complete manufacturing cell in a process described in detail in the following paragraphs.

The first step in the development stage was to decide on the main requirements for the ICAT cell and analyze setups developed by other manufacturers. Multiple companies are currently utilizing AFP for manufacturing of both thermoset and thermoplastic composites, some of the major organizations utilizing this equipment are Electroimpact, Coriolis, MIKROSAM, and Ingersoll Machine Tools. Figure 16a provides an image of NASA's ISAAC (Integrated Structural Assembly of Advanced Composites) AFP manufacturing equipment [68]. While these systems provide a good reference point for developing a custom system, they are all aimed at manufacturing large components, utilizing large robot positioning systems, and AFP end effectors that can lay down up to 32 uni-directional tapes at once, all with a hefty price tag. With the focus of the cell developed at UT Austin to be for R&D with a focus on design and materials understanding, the size of parts and rate of manufacturing are significantly lower than those aimed at commercial applications. Other main requirements for the system were to minimize overall cost and total footprint of the cell. The best solution for application was found in the AFP-XS AFP tool manufactured by Addcomposites Oy in Finland, depicted in Figure 16b [69]. The AFP-XS is a single-tow AFP tool packaged in a small form factor while still maintaining many of the same features of larger tools. The AFP-XS was coupled with a KUKA KR 160 R1570 nano6-axis robot that provides 1.6 m of reach and a ± 0.06 mm positional repeatability. With the selection of the AFP-XS and KUKA robot, the two major components of the AFP cell were found, and focus was turned to the remaining subsystems.

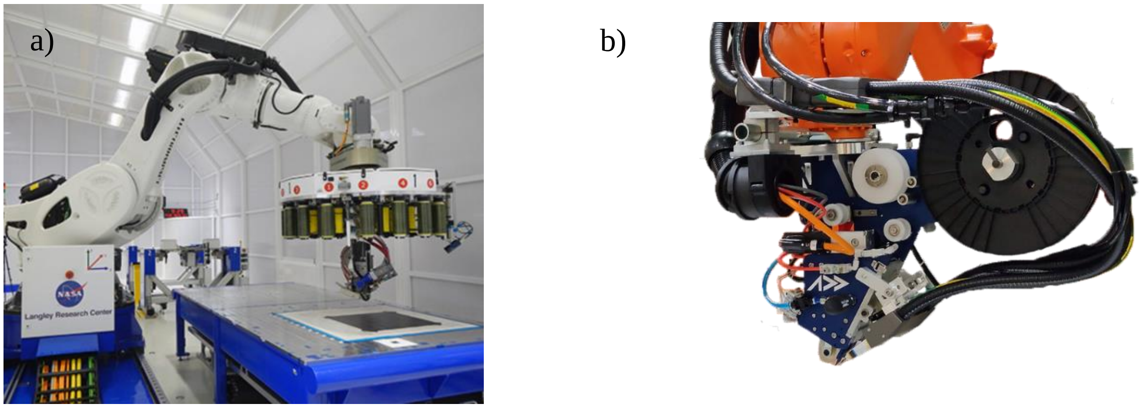

Figure 16. a) ISAAC AFP manufacturing equipment developed by NASA and Electroimpact [68] and b) Addcomposites AFP-XS tool [69].

Heating of the incoming thermoplastic tape was the next subsystem to specify. The AFP-XS tool was originally designed and built to process thermoset prepreg tapes and the system at UT Austin would be the first to modify it for use with thermoplastics. The main differences in AFP layup material is that thermoset prepregs are inherently tacky due to the partially cured epoxy and only require a low powered infrared heating lamp to stick the tows together. For the ICAT process, both the incoming thermoplastic towpregs and previously deposited layers must be heated to melting temperature in order to melt and bond the tapes as they pass under a typically flexible compaction roller. Given the processing velocity of ICAT can range from 10 – 1000 mm/s and the melting temperature of the thermoplastic material can be upwards of 400 ˚C, a high energy heating source is required. Upon researching the heating methods utilized by other manufacturers, it was found that the three most common methods are a hot gas torch (HGT) system, high powered heating lamp, and near infrared (NIR) laser. HGTs have been widely utilized in the past with good success but require a complex support system and a steel compaction roller. They, however, cannot achieve consolidation at high AFP speeds. High powered heating lamps are less utilized and have been shown to not be capable of reaching the high processing temperatures required for PAEK thermoplastics and are more suited for processing TPCs with lower melting points. NIR lasers are the latest technological advancement in ICAT and have come on as the most popular heating method in the previous five to ten years. The key to utilizing a NIR laser is the use of a wavelength that the PAEK matrix is transparent to, allowing the laser to fully penetrate the material and heat only the carbon fibers, which spreads heat to the surrounding matrix, bringing the entire towpreg up to a relatively uniform temperature. A process graphic is shown in Figure 17, depicting how the laser is utilized in ICAT to heat the incoming tape and layers below. For these reasons, a 980 nm wavelength, 600W, air-cooled diode laser was chosen and procured, which is shown mounted to the AFP tool in Figure 18b.

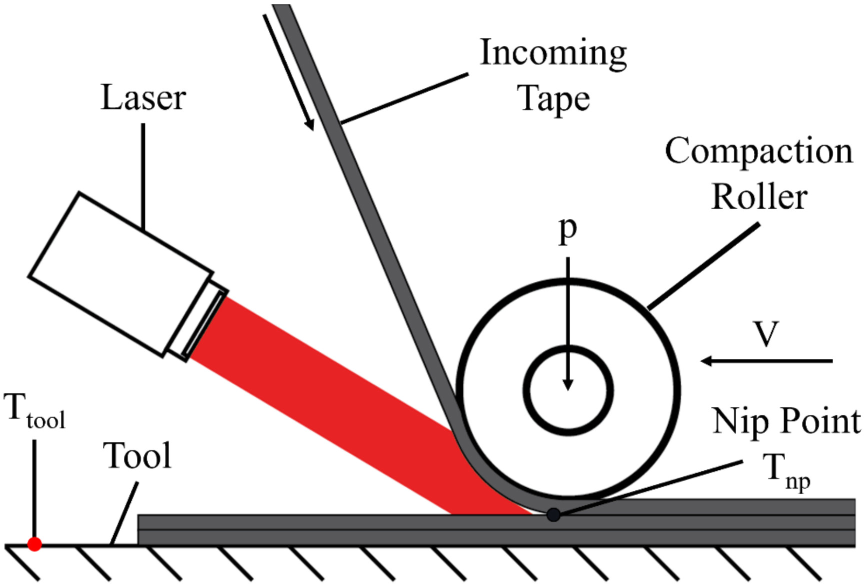

Figure 17: ICAT process overview diagram.

With the three major subsystems selected, the remaining major requirements were to select the layup tooling and design a containment system for the entire manufacturing cell to protect users from the laser and robot. Typical thermoset composites layup tooling can be a wide range of materials from metals to other composites. However, thermoplastic composites manufactured by ICAT have special requirements, the tooling must withstand direct laser contact and the high temperatures associated with it, be able to support the loads applied by the compaction roller and provide heating to minimize warpage inherent with manufacturing TPCs. To create a solution for this problem, a modular system was designed consisting of a 90 × 120 cm granite surface plate base with extruded aluminum rails mounted to the side from which various heated layup tools could be attached to. A granite surface plate was chosen for its tight surface flatness tolerances, ability to withstand high loads from the compaction roller and high temperatures, as well as its relative affordability when compared to precision ground steel or aluminum plates. An adjustable frame was built to hold the surface plate and extruded aluminum was attached to the outside of the frame. A 76 × 76 cm flat layup tool was constructed with silicone heating pads on the underside capable of heating the tool to 150 ˚C. The flat layup tool can be easily mounted and removed from the granite surface plate to exchange with three-dimensional layup tooling. The heated layup tool is shown in Figure 18a.

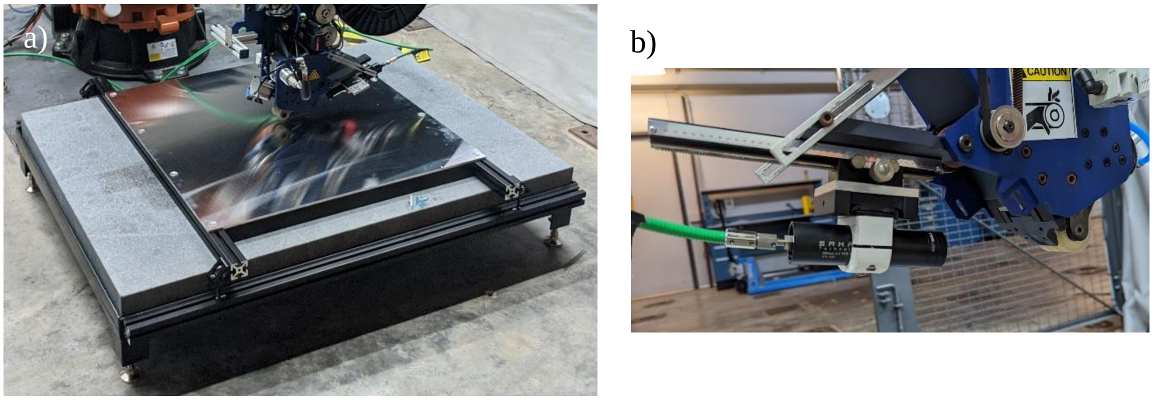

Figure 18: a) Flat heated layup tool and b) the laser mounted onto the AFP-XS.

The entire system was required to be contained in an enclosed cage for two reasons, the first is the inherent danger of operating a robotic system and the second being the class 4 designation of the selected laser system. A 3.9 m wide, 4.8 m long, and 2.6 m high wire panel cage with front entry and full ceiling was chosen to house the robot and layup tool. For laser safety, half the side walls and entire roof were covered in black anodized aluminum sheeting to absorb laser radiation. Laser curtains were put up on the other half of the side walls and front of the cage so that the manufacturing cell could be opened up for display during non-usage if desired.

CONSTRUCTION

Construction of the ICAT cell was carried out over a six-month period. Contractors were brought in to mount the KUKA robot to the floor and bring the robot online. The construction process was carried out as follows, the KUKA was mounted to the floor, the containment cage was erected around the robot, the AFP-XS tool was attached to the KUKA, all controllers were mounted and wired, and the system was brought online and preliminary layups were performed with thermoset prepregs to test functionality. After functionality was confirmed, the laser proofing of the cage and modifications to the AFP-XS for thermoplastic layups were carried out. As previously mentioned, the AFP-XS was designed and built for thermoset layups, resulting in modifications having to be performed to the tool and software to perform ICAT. The first step was to remove the IR heating lamp and affix the laser to the front side of the AFP-XS, aimed equally at the incoming tape and previous layer. To do this, a mounting system was provided by Addcomposites that is adjustable in both length and angle. A rotational stage was added, and laser clamp was fabricated via 3D printing to finish the laser mounting process; the tool with laser attached is shown in Figure 18b. The other major modification to the provided equipment was making changes to the software to turn on and off the laser as well as control laser power. An open loop control method was chosen to set the laser power based upon speed of the tool. For each given processing speed, a calibrated laser power is utilized to heat the incoming towpreg to melt. An unforeseen issue was the overheating of tapes at the very beginning of each pass where the speed of the robot is lower during initial tape placement than in the middle of the pass. To combat this issue, a step function was implemented in the post processor to bring up laser power slowly from a lower power as opposed to the value set for constant speed in the middle of the layup. With the modifications for ICAT carried out, the cell was complete and ready for research use. Figure 19 provides images of the complete cell.

Figure 19: a) AFP cell front, b) AFP cell control center, and c) AFP robot and tool.

Chapter 5. In situ Consolidation of Carbon Fiber PAEK via Laser-Assisted Automated Fiber Placement

Authors: Nathaniel Heathman, Pratik Koirala, Timothy Yap, Anahita Emami[*],
and Mehran Tehrani

[*]Ingram School of Engineering, Texas State University, San Marcos, TX

Automated fiber placement (AFP) of thermosetting composites has been one of the leading manufacturing techniques for aerospace structures over the last decade. Thermoplastic composites (TPC) offer several advantages including a high toughness, recyclability, weldability, and potential for rapid out-of-autoclave manufacturing. High-power heating sources and flexible compaction rollers can be used to melt and consolidate TPC tapes via AFP to form large structures in a layer-by-layer manner as used in additive manufacturing. This paper investigates the in-situ consolidation AFP of TPC tapes (ICAT) toward their process optimization and revealing mechanisms that govern the ICAT process. To this end, a laser-assisted AFP was utilized to fabricate short beam strength samples from carbon fiber reinforced low-melt polyarylyletherketone (LM-PAEK™) at various processing parameters. Analysis of results revealed how ICAT process parameters affect interlaminar bonding, crystallinity, and void content in manufactured parts. Multiphysics finite element analysis (FEA) was also carried out to reveal mechanisms that control void, crystallinity, and bonding in ICAT. Finally, a comparison of post-fracture specimens made via ICAT with traditional compression molding was used to explain the underlying failure mechanisms in ICAT coupons. This study shows that at AFP rates of up to 0.15 m/s, high interlaminar shear strengths, up to 60 MPa, are possible to achieve with low void content (<1%) and high crystallinity (>20%), proving that ICAT is potentially a viable process for manufacturing the next generation of aerospace composites.

This chapter contains material from the following publication: [65] Composites Part B Eng., vol. 249, p. 110405, Jan. 2023

Author Contribution
Nathaniel H: Fabrication, testing, analysis
Pratik K & Anahita E: Modeling
Timothy Y: Fabrication, testing
Mehran T: Supervisor

INTRODUCTION

Automated Fiber Placement (AFP) has become a mainstay in aerospace manufacturing over the past two decades, with multiple major companies turning to AFP for production of their latest airframes, such as the 787 one-piece fuselage program. AFP relies on deposition of dry fiber or prepreg tapes to form a composite preform for processing such as liquid molding or autoclave curing. AFP enables manufacturing of complex geometries with a high repeatability and at layup rates that are otherwise not possible [70]. Even with the high placement rates achievable with AFP, autoclave post-processing (inherent to thermoset-based composites) increases composite manufacturing time and energy significantly. In-situ consolidation AFP of thermoplastic composites (TPC) offers a solution to this issue, potentially resulting in composite structures that are fully consolidated and ready for trimming, drilling, and assembly directly after layup [71]. Achieving in-situ consolidation AFP of TPC (ICAT) rates above 500 mm/s can potentially retire autoclaves for commercial aircraft manufacturing, while lower deposition rates can enable out-of-autoclave manufacturing of medium-sized composite structures for other markets such as the urban air mobility industry. A third possibility, currently being investigated by NASA, is high-rate partial consolidation AFP of TPCs followed by vacuum bagging only consolidation in a regular oven [72].

Manufacturing of TPCs has seen a dramatic increase in several industries and research groups in the past few years [12]. Aside from the in-situ processing ability of TPCs, they also offer impressive toughness, repairability, recyclability, and weldability for joining [73], [74], [75]. AFP utilizes a specialized end effector to deposit carbon fiber tapes onto a layup tool, as shown in Figure 20. With ICAT, the incoming tape and top surface of the previously deposited layer are heated to melting temperature and simultaneously compressed with a compaction roller to consolidate the layers, as shown in Figure 20.

Placement rates to achieve ICAT in past studies have been relatively slow (e.g., an order of magnitude slower than rates used for thermosetting tape AFP) as bond formation across interfaces requires time under elevated temperatures and high pressures. To combat the low placement rate issue, special end effectors have been designed with individual compaction rollers and heaters to place up to thirty-two tapes at once [76]. There is a wide range of heating methods being utilized to bring the tapes up to melting temperature at high processing speeds. Hot gas torches, high-powered flash lamps, and lasers are all common methods, with lasers becoming the main heat source in recent years [77]. The main advantage to using a laser system is the ability to choose a laser wavelength that is transparent to the polymer matrix, heating up only the fibers which dissipate heat to the matrix and result in a uniform temperature across the entire thickness of tapes. The primary polymers utilized for the laser-assisted AFP process are the semicrystalline high-performance thermoplastics belonging to the polyaryletherketone (PAEK) family, including polyetherketoneketone (PEKK), polyetheretherketone (PEEK), and engineered low melt PAEK (LM-PAEK™). These polymers are compatible with carbon fibers, possess excellent thermo-mechanical properties, inherent chemical resistance, and are suited for additive manufacturing processes [78], [20], [79], [5].

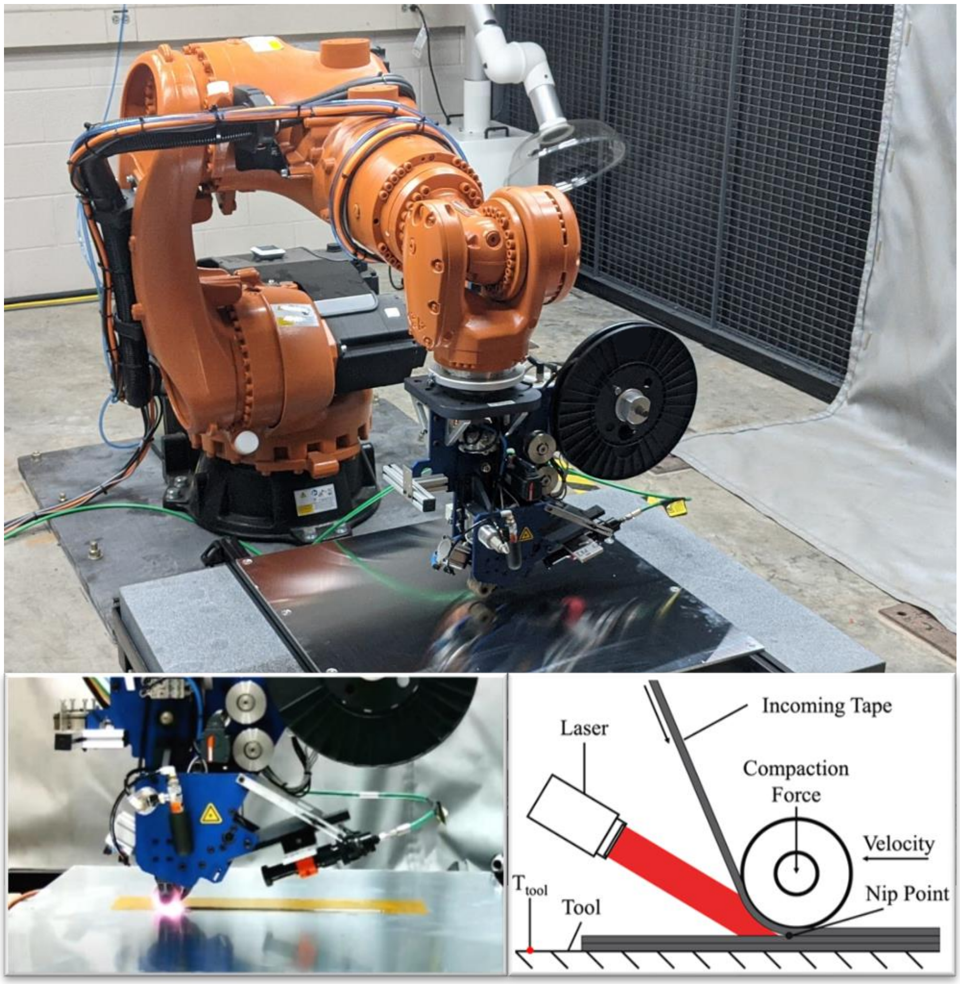

Figure 20: Thermoplastic AFP manufacturing equipment used in this study. Left inset figure is taken during laser-assisted ICAT. Right inset schematically shows the key processing parameters in ICAT.

ICAT is a complex process depending on many different factors to produce a high-quality composite. Intimate contact development, polymer chain diffusion, void formation/growth and elimination, thermal history and crystallization kinetics, and residual stress development determine a part's strength [1], [80], [81]. The degree of intimate contact is defined as the percentage of tape area in contact with the previous layer and is directly dependent on the viscosity of the material at an elevated temperature and the duration and magnitude of pressure applied to the interface [3], [82], [83]. Increasing the process temperature and pressure, applied via the compaction roller, effectively increases the degree of intimate contact, as long as the polymer matrix can flow [84], [85]. For interfaces where intimate contact is achieved, polymer chains begin to diffuse across in a process deemed autohesion [86], [87], [4], [88]. Autohesion occurs at temperatures above polymer's glass transition temperature (T_g). Once autohesion is completed, the strength of the interface can be calculated as the degree of bonding [89], [90]. Thermal history determines the crystallization kinetics of semicrystalline polymers, such as LM-PAEK. A high crystallinity value maximizes mechanical performance and can be achieved with a slow cooling rate (e.g., a few ºC/min) from melt. Cold crystallization can also occur in fast cooled (e.g., 100 ºC/min) non-fully crystallized polymers at temperatures above T_g, but much below melting.

Void content is another critical property of the fabricated laminate and must be minimized to ~1% or less, to meet the standards required in critical applications. Voids exist in feedstock tapes and also form during the AFP process [6]. It is theorized that void transportation and compression/decompression are the main mechanisms involved with interlaminar void development [91]. During TPC AFP, the material is heated to melting temperature, reducing the viscosity and releasing trapped volatiles and voids in the incoming tape, which travel to the surface [7]. The pressure applied via the compaction roller increases the degree of intimate contact and simultaneously eliminates the intra-ply voids; however, when roller pressure is removed and the material is still above T_g, voids can reappear [92]. Gaps between deposited tapes can also result in voids.

Finally, the significant difference in thermal expansion coefficients of fibers and matrix, as well as large thermal gradients inherent to TPC AFP can result in developing residual thermal stresses in TPC parts. Residual stresses cause part distortion in-service and lead to scrapped parts. It has been shown that utilizing a heated layup tool can reduce residual stresses as well as cooling rate, enhancing crystallinity in the final laminate [93], [94]. Intimate contact development, polymer chain diffusion, void formation and growth, and thermal history all have a major role in the resulting properties of a composite manufactured via AFP, and while modeled in prior research, all are a direct result of processing parameters. Modeling of these mechanisms combined with validation through manufacturing and testing is critical in developing a further understanding of the ICAT process. This understanding can facilitate the optimization of ICAT processing parameters, and in turn control defects and microstructure of TPC parts.

ICAT is highly sensitive to process parameters [95]. A study on how processing parameters affect mechanical properties of carbon fiber polyphenylese sulphide (PPS) composites manufactured via ICAT, found that the highest interlaminar shear strength (ILSS) values were achieved with composites that had the lowest void content, independent of crystallinity [96]. Furthermore, when the composites parts were post processed in an autoclave, their ILSS values increased due to a further reduction in void content [96]. When investigating the effect of processing parameters on single lap shear strength (SLS) and crystallinity of CF LM-PAEK composites manufactured via ICAT, it was found that crystallinity and SLS are higher in samples manufactured on a heated layup surface [66]. This study also showed that interlaminar bonding strengths remain high even at higher layup speeds of 250 mm/s, showing that LM-PAEK™ is suitable for high speed in situ AFP [66]; compared with the present study, [66] uses higher processing speeds and lower compaction pressures.

A study on the microstructure and mechanical properties of carbon fiber PEEK composites manufactured via hot gas torch AFP found that increasing torch temperature and consolidation force while keeping the speed constant results in the highest short beam strength (SBS) [97]. However, further increasing of these parameters resulted in fiber damage and thinning of samples [97]. This study showed the importance of optimizing processing parameters for a material while closely controlling the width and thickness of the deposited tape is key to producing a high-quality laminate. It is worth noting that hot gas torch AFP uses a metal roller that is heated to above 900 ˚C to melt the incoming tape upon touching. The hard roller results in a high but short duration pressure. In contrast, flexible rollers used in laser-assisted AFP achieve a lower magnitude but much wider pressure length in tapes underneath them.

Another research study sought to find the effect of processing temperature and speed on the SBS of carbon fiber PEEK composites manufactured via ICAT. The research varied the process speed between 100 mm/s and 400 mm/s and investigated the optimal process temperature to produce the highest SBS [98]. The results show that for 100 mm/s a temperature of 500 ˚C produced laminates with a SBS on par with CF PEEK manufactured with conventional methods. At 400 mm/s, they were unable to achieve SBS results as high, which was theorized to be due to the "insufficient dwell time at the temperatures required for bond development" [98]. To the best of the authors' knowledge, results of the aforementioned study have not been reproduced to date by other groups.

It is clear from the literature review that roadblocks remain in achieving full material strength using ICAT. Most notably, ICAT results in incomplete interlaminar bonding, higher void content, and lower crystallinity compared with compression molded samples. With further research into bonding mechanisms, void development, and crystallization process, along with new material developments, it may be possible to advance ICAT for industry widespread adoption.

This paper aims to investigate processing and bond formation of a relatively new material, unidirectional (UD) carbon fiber LM-PAEK™, manufactured via ICAT. LM-

PAEK is the latest material offering belonging to the PAEK family of semicrystalline thermoplastics. This polymer seeks to resolve the shortcomings with PEEK and PEKK by lowering the processing temperature by 60 ˚C, while providing a lessened viscosity at melt to promote polymer diffusion. In theory, this material has potential to enable higher processing speeds and enhanced interlaminar bonding. The main questions this research seeks to answer are, what the optimized processing parameters for this material are, how do processing parameters affect interlaminar bonding, crystallinity, and void content in parts, and what their interlaminar failure mechanisms are. To answer these questions, samples were prepared at differing process parameters, determined by a design of experiments, and analyzed to find their level of interlaminar bonding, crystallinity, and void content. From the results it was possible to determine how processing parameters affect the resulting short beam strength and to what extent void content and crystallinity affect interlaminar bonding strength. A numerical model was developed to predict layer temperatures and pressures during ICAT, shedding light on ICAT processing, bonding and crystallization kinetics, and void formation/elimination mechanisms. Finally, fractography of ICAT and compression molded samples also provided a new understanding of SBS failure mechanisms in ICAT samples.

MATERIALS AND METHODS

Experimentation

The feedstock tape used for this research was 12.7 x 0.19 mm unidirectional (UD) carbon fiber reinforced LM-PAEK™ towpreg supplied by Suprem. The tape utilizes a standard modulus carbon fiber with a 55% fiber volume content and Victrex AE250 LM-PAEK™ matrix. AE250 LM-PAEK™ is the latest development in the semicrystalline high performance polymer family that offers comparable mechanical and thermal properties to standard PEEK and PEKK but with a lower processing temperature and viscosity. The key to LM-PAEK™'s performance is the reorganization of the polymer chains into co-polymer groupings that change the thermal, crystallization, and rheological characteristics of the material [62]. This enables a lower viscosity at melt temperature and a reduction of processing temperature by up to 60 ˚C compared with PEEK.

All samples were fabricated on a single tow AFP toolhead attached to a KUKA robot. Tape melting was accomplished with a 600 watt 980 nm wavelength diode laser. Processing temperature was calibrated using a FLIR A325 thermal camera to correlate laser wattage to maximum temperature observed near the nip point, within the processing window of 360 – 400 ˚C, at speeds of 50, 100, and 150 mm/s. A silicone compaction roller was used to maximize the pressure area under the roller. The roller has a diameter of 40 mm, width of 32 mm, and a 21 mm diameter aluminum core with over-molded Shore A hardness 25 silicone. Compaction forces of 200, 300, and 400 N were used and verified with a force sensor mounted between the AFP tool and robot. All samples were fabricated on a flat heated layup tool at 100 ˚C to eliminate warpage inherent to fabricating TPCs and enhance crystallinity of fabricated coupons. A side view of the AFP tool and thermal image during a layup are shown in Figure 21.

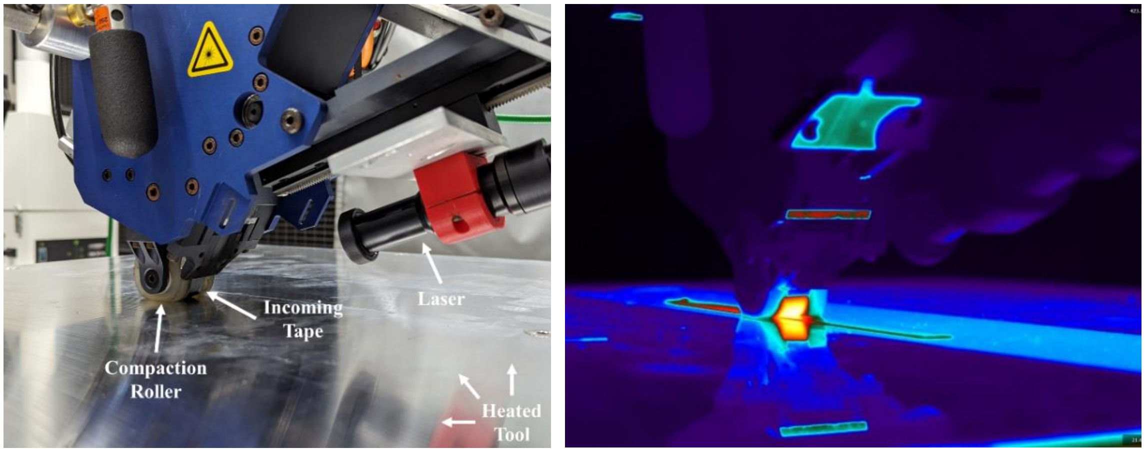

Figure 21: AFP tool schematic and thermal image of the manufacturing process.

Samples were fabricated according to a design of experiments (DOE) built to analyze processing parameters selection to optimize ILSS values, which directly correspond to bonding quality between layers. Speed, processing temperature, and compaction force were chosen as the process parameters to study. Three factors per variable were chosen: speed was varied between 50, 100, 150 mm/s, laser power was varied to achieve 360, 380, and 400 ˚C near the nip point (nip point temperature is higher), and compaction forces were varied between 200, 300, and 400 N. A partial factorial DOE consisting of nine samples was selected, with SBS as the response. The DOE is shown in Table 5. The Taguchi statistical method was used to perform a final analysis of the results to reveal the effects of each variable selection on the interlaminar bonding of the part. Several samples using new processing parameters suggested by the Taguchi analysis results were manufactured afterwards.

A reference compression molded sample was manufactured for comparison. Thermoforming was performed by inserting an AFP coupon into an aluminum mold, heating to 380 ˚C at a 2 ˚C/min heating rate, dwelling at 380 ˚C for one hour, then cooling to T_g at 1 ˚C/min, after which the part was allowed to cool to room temperature in an uncontrolled manner, all while under 41 kPa of pressure. Short beam strength testing was carried out following the ASTM D2344 standard. All SBS samples were cut down to a size of 40 mm in length, 12 mm in width, and 6 mm in thickness and measured before testing. Testing was carried out using an MTS Criterion machine with a 50 kN load cell and a three-point bending fixture with a 24 mm span, 6 mm loading roller, and 3 mm support rollers. The span to thickness ratio (24/6 =4) resulted in pure interlaminar shear failure in all tested samples.

Table 5: Design of experiments

Sample	***Speed (mm/s)***	***Processing Temp. (˚C)***	***Compaction Force (N)***
#1	50	360	200
#2	50	400	300
#3	50	380	400
#4	100	360	300
#5	100	400	400
#6	100	380	200
#7	150	360	400
#8	150	400	200
#9	150	380	300

Cross sectional inspection of the fabricated samples and feedstock was carried out via optical microscopy. Sections of each SBS sample were cut to size, mounted in epoxy, and sanded in steps from 80 grit to 2000 grit with a Struers polishing machine, followed by a final polishing step with 1 µm suspension fluid. Imaging of the samples was performed with a Keyence VK-X1100 Optical Profilometer. Cross sectional images were then analyzed in Object Research Systems Dragonfly software to reveal void content.

Thermal analysis via differential scanning calorimetry (DSC) was performed with a NETZSCH DSC 214. Samples were heated at 10 ˚C /min to 400 ˚C to measure their T_g, cold crystallization values, and crystallinity. Tape material was fast cooled at 500 ˚C /min and slow cooled at 1 ºC/min from 400 ˚C to ambient temperature, and subsequently heated up at 10 ˚C /min to 400 ˚C to measure their crystallization kinetics, i.e., respective maximum and minimum crystallinities. For comparison of the DOE specimens, one sample was taken at the middle of each specimen. Crystallinity was calculated following , using a fiber weight fraction of 63%, provided by the manufacturer, and an enthalpy of fusion of 130 J/g for the LM-PAEK [23].

$$X_c = \frac{\Delta H_f + H_c}{\Delta H_f^{\circ} \times (1 - W_f)} \qquad \text{(Equation 1)}$$

Where X_c is the crystallinity of the material, ΔH_f is the enthalpy of fusion at the melting point, H_c is the enthalpy of cold crystallization, ΔH°_f is the enthalpy of fusion for a completely crystalline polymer, and W_f is the weight fraction of carbon fiber in the sample.

Modeling

An AFP model was developed for finite element analysis (FEA) to investigate thermal and pressure histories at interlaminar interfaces. ABAQUS was used to perform coupled temperature displacement analysis and a 2D plane strain condition was assumed. Each single tape layer was modeled as a 3D, deformable, homogenous solid part with dimensions of 10, 1, and 0.125 mm, shown in Figure 22a, whereas the heated tool surface was modeled as a rigid surface. Since carbon fiber LM-PAEK is a relatively new material, most of its mechanical and thermal properties are not available. To avoid expensive and time consuming material characterization, properties of carbon fiber PEEK (Supplementary materials Table S1-S7) composite were used for the simulations since they share a similar structure; however, the melting and T_g were updated [99]. Three layers of tapes were stacked on top of the substrate (tool) and each tape layer was meshed using

3000 elements. This mesh size was checked for convergence. C3D8T elements (8 nodes, bilinear displacement, and temperature) were used in this model. The heat and pressure boundary conditions were set to simulate the actual AFP process. Transient analysis was performed since both the heat flux and the compaction pressure depend on time. A FORTRAN subroutine was developed to apply the moving heat flux and pressure to the tapes. The speed of the roller and laser, along with the heating length, is also defined in a subroutine file.

To reduce computation time, a scaled down model (10 mm long) was built. Lengths of both the laser heated (12mm) and compaction roller (16mm) sections in experiment were longer than the model's length. The heat flux and pressure boundary conditions in the model were, therefore, scaled down by a factor of four to 3mm and 4mm, respectively, with a time lag of 0.1 s (time lag between pressure and temperature peaks in experiments were calculated to be ~0.4 s). Time was scaled up by the same common factor to plot the simulated pressure and temperature data.

The heat flux was applied on the bottom of the incoming tape and on top of the existing tape, whereas the compaction pressure was applied on the top tape only. For the simulation, a heat flux of 1.4 W/mm^2, maximum compaction pressure of 1.25 MPa, and roller and processing speed of 50 mm/s were used. The substrate was constrained from moving and rotating in all directions. Tapes faces were not constrained, tapes ends were constrained from moving and rotating except for displacement in the build (z) direction, and tapes sides were free to move but not rotate. To define inter-layer interactions, mechanical and thermal contacts were specified. There is conduction between the substrate to tape, tape to tape, and convection between the tape and surrounding air. Temperature-dependent properties of materials were predefined in the material section following [99] and added to the supplementary file. Radiation and heat loss to compaction roller are ignored in this simulation, as they are expected to be negligible. The tool surface is always maintained at 100 °C, whereas the ambient is 25 °C. The force and laser power are applied separately, and the pressure and thermal history on a single node are output.

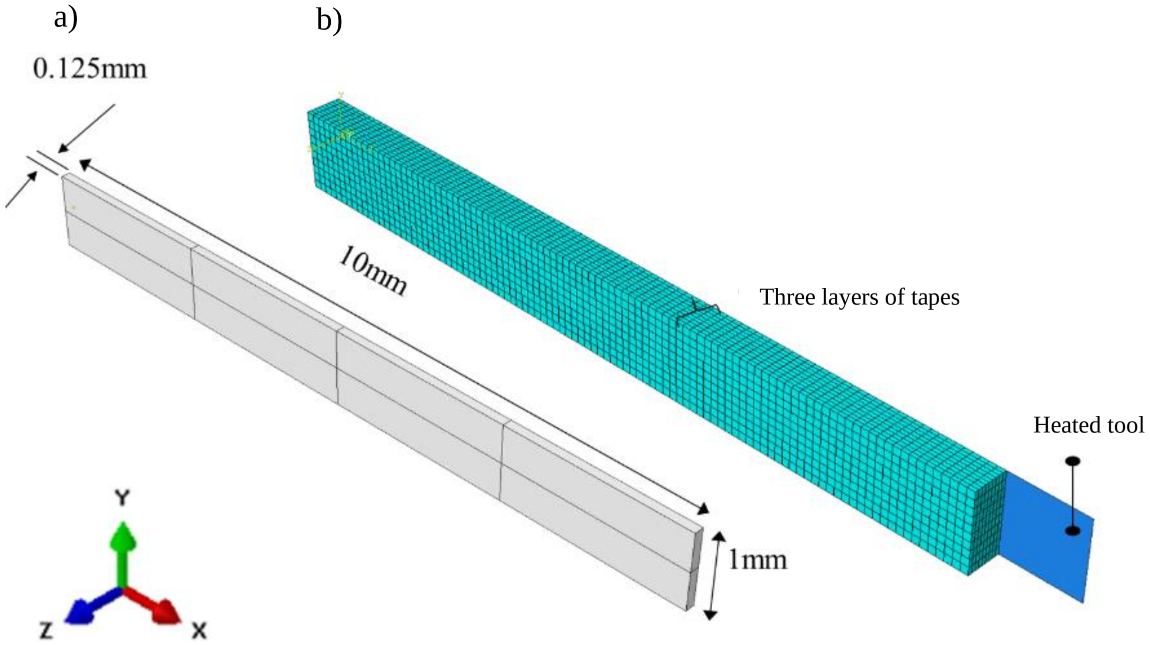

Figure 22: a) Model of single layer of tape and b) the assembly of three layer of tape with mesh size used in simulation.

RESULTS AND DISCUSSIONS

Analyzing the feedstock UD tape for homogeneity was the first step in understanding how possible defects are formed in AFP parts. Figure 23 shows cross sections of representative feedstock tapes imaged at 10x. Figure 23a shows a cross section with a uniform distribution of fibers and polymer, Figure 23b shows a cross section with areas of high polymer content with no fibers, and Figure 23c cross section includes several voids distributed through the tape. While a large majority of the tape width consists of a homogeneous distribution of fibers and polymer, these polymer rich and high void regions represent a portion of the areas across the width of the tape.

Short beam strengths (SBS) for tested samples are plotted in Figure 24a. Testing data shows a maximum SBS value of 63 ± 1 MPa for sample #2, corresponding to a speed of 50 mm/s, processing temperature of 400 ˚C, and 300 N compaction force. At 100 mm/s, a comparable SBS was achieved; 61 ± 1 MPa at 400 ˚C processing temperature and 400 N of compaction force. Samples manufactured at 150 mm/s exhibited relatively lower strengths, with the highest SBS value of 51 MPa. The lowest measured SBS among all tested samples was 45 MPa, corresponding to a processing temperature of 360 ˚C and speed of 150 mm/s, showing that the combination of high processing speed and low temperature is ineffective in forming strong interlaminar bonds.

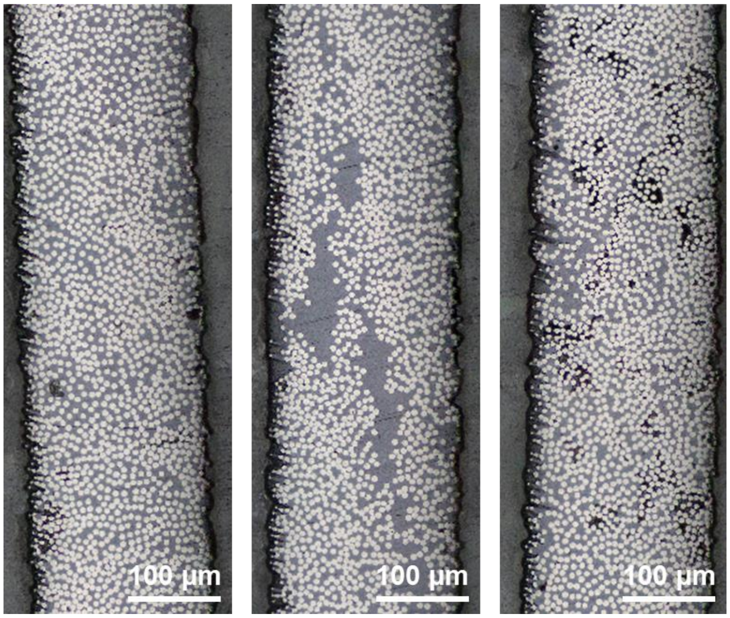

a b c

Figure 23: UD tape cross sections representing a) homogenous region, b) resin rich region, and c) high void content region.

PAEK crystallinity percentages for all nine samples are plotted in Figure 24b. Results show that despite differences in short beam strength, almost all samples obtain a similar crystallinity, i.e., ~ 20%, with the exception of sample #7. The feedstock tape was also tested to identify the range of achievable crystallinities with carbon fiber LM-PAEK. Slow cooling the tape from melt at 1 ˚C/min resulted in a crystallinity of 30%. In contrast, a high cooling rate of 100 ˚C/min from melt resulted in a crystallinity of only 6%. Compared with these two crystallinity extremes, the fabricated SBS samples achieve a relatively high crystallinity. The lowest crystallinity sample (#7) corresponds to a relatively low SBS, resulting from partial consolidation due to relatively fast processing speed and low laser power. SBS results were input into a Taguchi analysis algorithm and the main effects are plotted in Figure 24c. Taguchi analysis provided an understanding of how each processing parameter affects interlaminar bonding in tested composite coupons. For the range of processing parameters studied here, lower speeds, higher processing temperatures, and larger compaction forces are shown to enhance interlaminar bonding.

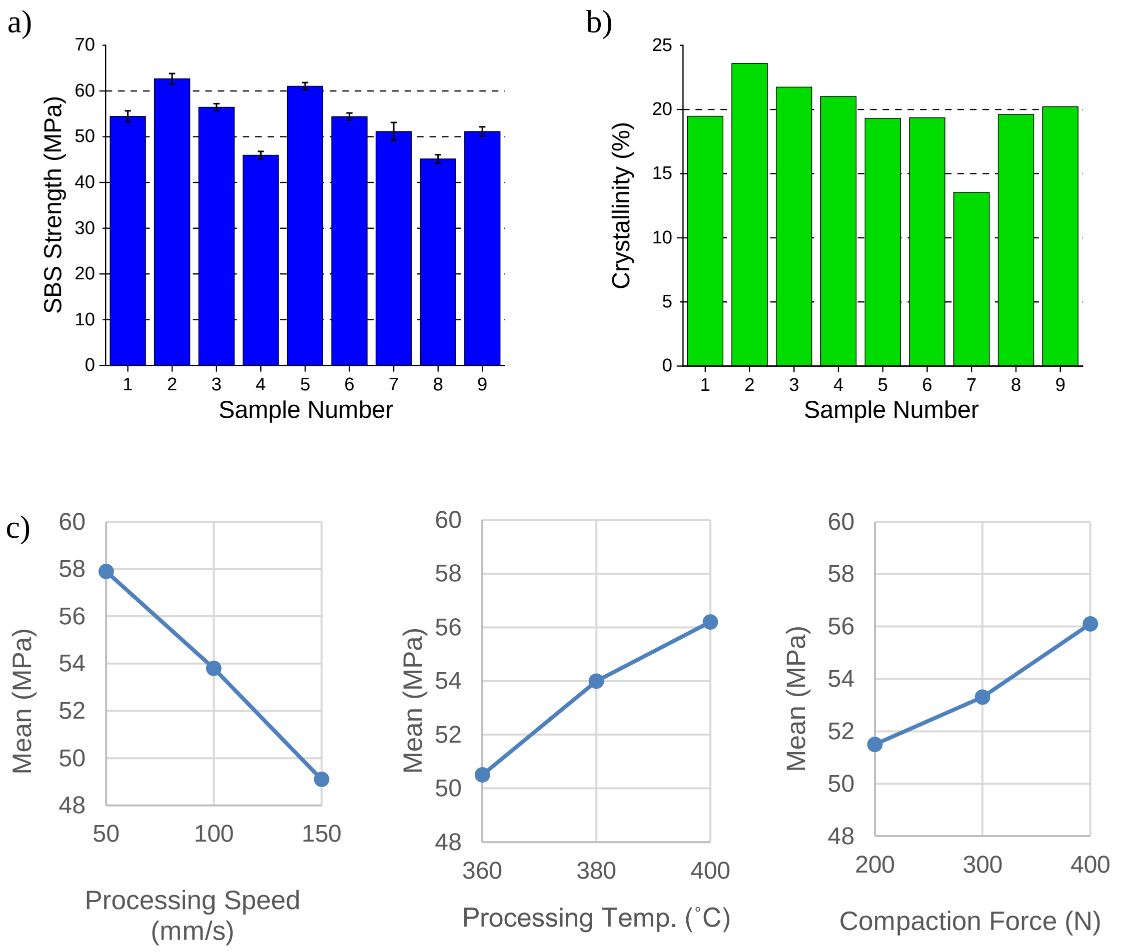

Figure 24: a) Short beam shear results, b) crystallinity values, and c) Taguchi analysis of SBS strengths.

Taguchi analysis shows that processing speed has the greatest effect on interlaminar bonding, with processing temperature having the second largest effect. Where the greatest effect was found by comparing the slopes of the mean plots; the x-axis of these plots corresponds to variable levels 1, 2 and 3, with the actual values superimposed on top for ease of understanding. The main effects plot shows a negative correlation between increasing speed and SBS, but a positive correlation with increasing processing temperature and compaction force. In other words, considering the tested processing space, parts manufactured at low speeds with the highest possible processing temperature and compaction force yield the highest levels of interlaminar bonding.

The process of bond development is complex and depends on multiple factors, such as crystallization kinetics, degree of intimate contact, autohesion (healing), which all in turn depend on pressure and temperature histories of interfaces. The following equation captures the two stages of bonding, namely intimate contact (ic) and autohesion (ah):

$$Degree\ of\ Bonding\ (D_b) \equiv D_{ah}.\,D_{ic} \quad D_{ah} \propto \frac{t^{1/4}}{e^{\frac{\alpha}{T}}} \ \ D_{ic} \propto \left[\int_0^t \frac{P}{\mu} dt\right]^{1/5} \qquad \text{(Equation 2)}$$

Where D_b, degree of bonding, is the product of the degree of intimate contact, D_{ic}, and the degree of autohesion, D_{ah}, t is time, T is the absolute temperature of the interface in isothermal welding, α is a constant, P is the applied pressure, and μ is viscosity (which reduces with temperature) [50]. From these equations, it can be seen that lower AFP speeds combined with higher compaction forces and processing temperatures increase the degree of intimate contact. Similarly, the longer two surfaces for which intimate contact has completed are above a threshold temperature, the greater their degree of bonding will be due to autohesion; the temperature should be low enough to prevent polymer degradation. The threshold temperature for autohesion believed to be slightly above polymer's T_g [85]. Another important factor to consider is that autohesion rate slows down as the crystallinity of the polymer at the interface increases [100].

With the insights gained from the preliminary testing, Figure 24c, further tests were carried out using optimized process parameters with the goal of increasing SBS. Samples were manufactured at 50, 100, and 150 mm/s using a 400 ˚C processing temperature, with 400 N of compaction force. SBS testing results showed no increase in strength for 50 mm/s and 100 mm/s compared to their previous highest values, but at 150 mm/s SBS was increased to 55 MPa. At 150 mm/s processing speed and 400 N compaction force, the laser power was further increased to elevate processing temperature to 450 ˚C and 500 ˚C. SBS testing results showed a drop in strength after 400 ˚C, suggesting that processing temperature was not the cause of the lower SBS at 150 mm/s.

In addition to crystallinity, intimate contact, and autohesion, void formation and elimination influence properties of ICAT coupons. Void formation and elimination is controlled by the quality of the feedstock tape as well as processing temperature and pressure histories. Backside thermal imaging was performed on a specimen laid down at 50 mm/s, as shown in Figure 25a, to monitor tape temperature right after it passed under the roller. The temperature on the top side of the tape upon exiting the roller was ~260 ˚C and cooled below T_g (147 ˚C) within centimeters (in ~1s) after being deposited. Removing the pressure while the material is still above T_g results in void growth. This occurrence is demonstrated in Figure 25b, where the topmost layer of sample #8 shows to have a significantly higher void content than previous layers. It is clear from Figure 25b that voids that are formed in a layer are subsequently eliminated under the repetitive pressure and heat from depositing consecutive tapes on top of it. Figure 25c and d show the through thickness microstructure of SBS samples with a high strength sample #2, Figure 25c, and a low strength sample #8, Figure 25d, shown side by side for comparison. The cross section for sample #2, shows a homogenous distribution of fibers with clear resin rich areas on the tape boundaries and minimal void content. The cross section for sample #8, shows a less homogenous distribution of fibers and a significant number of voids that develop mostly within the interior of the tape layers (intra-laminar voids). From this visual analysis it is clear that processing parameters affect void content significantly.

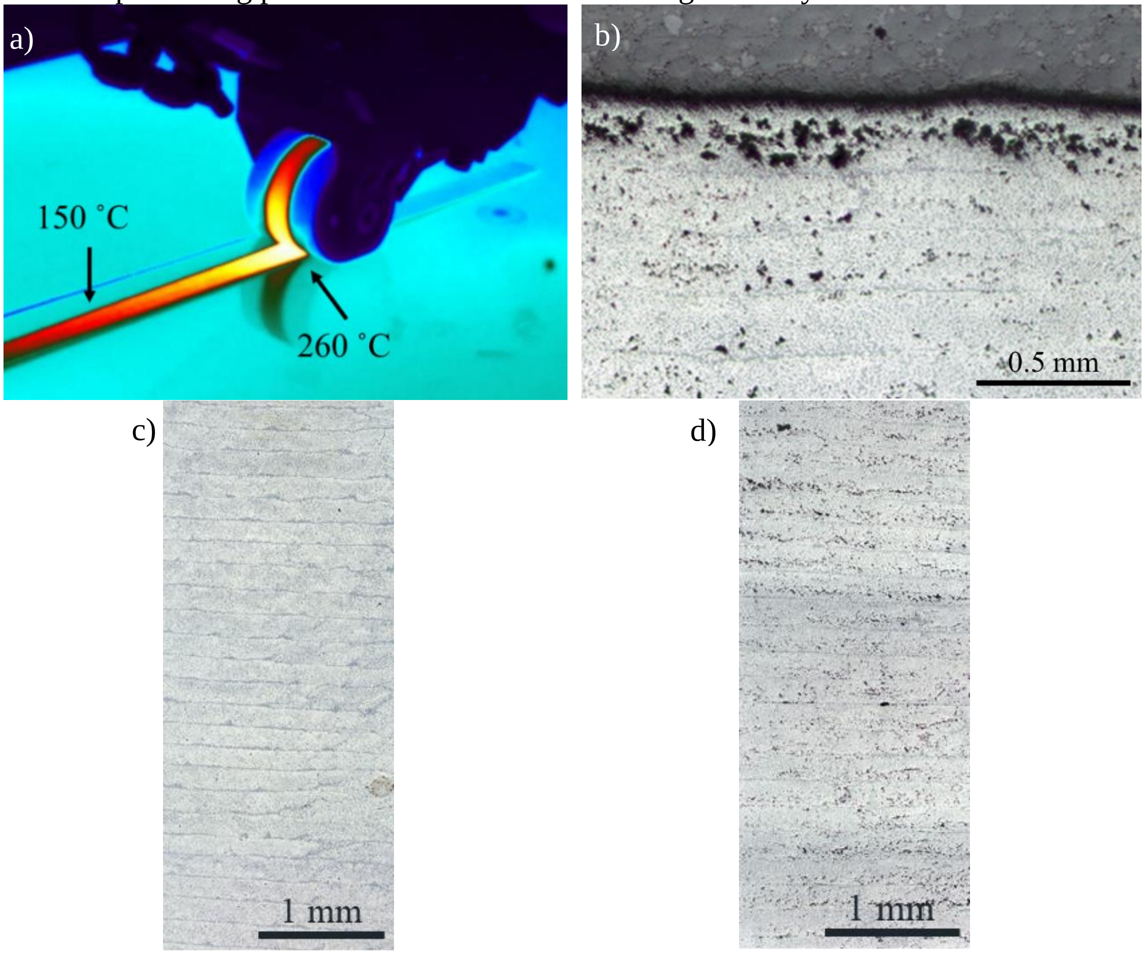

Figure 25: a) Backside thermal image of the laser-assisted AFP, b) voids formed and eliminated in top layers on an AFP specimen, Sample #8, c) cross section of sample #2, and d) cross section sample #8.

Void content is a critical parameter in determining the overall performance of a composite and can greatly impact the level of interlaminar bonding. The microstructure of all samples was analyzed under an optical microscope to calculate void percentage and gain a further understanding of the overall processing-structure relationships. Void analysis results for all nine samples are shown in Figure 26a. Void volume content ranges from

0.2% to almost 2.7%. To understand the effect void content has on SBS, it is plotted as a function of the SBS. A linear trend line is fitted to this data, as shown in Figure 26b, confirming a correlation between low void content and high SBS. However, when extrapolating the trendline down to zero void content, SBS does not match the ideal strength for the material, i.e., ~90 MPa, meaning other phenomena are partially responsible for the reduced interlaminar shear strength. To further analyze the correlation between void content and processing parameters, the DOE was changed to have void content as the desired output and the Taguchi analysis was replotted with the main effects graphs shown in Figure 26c. The results have processing temperature as the most impactful parameter with clear correlations to a higher processing temperature and lower speed producing a lower void content. However, compaction pressure has the inverse effect of what would be expected with a higher compaction pressure producing an increased void content. This is due to utilizing a partial factorial DOE that does not provide a complete data set for Taguchi analysis. Additionally, it seems that compaction pressure has a much smaller effect on void content compared with processing temperature and speed. This is likely due to the fact that the compaction pressure is removed while the material is still above T_g, as shown in the backside thermal image (Figure 25a) and further explained using numerical simulations hereafter. Another possible explanation is that the level of compaction force has a negligible effect when processing temperature is high [92]. Not considering the compaction pressure, the Taguchi results are similar to the analysis developed for SBS, which is to be expected considering the void elimination relies on similar mechanisms as those responsible for interlaminar bonding. That is, a lower polymer viscosity and longer dwell time while under pressure allows resin to flow within the tape to form intimate contact followed by polymer autohesion, resulting in void closure [101].

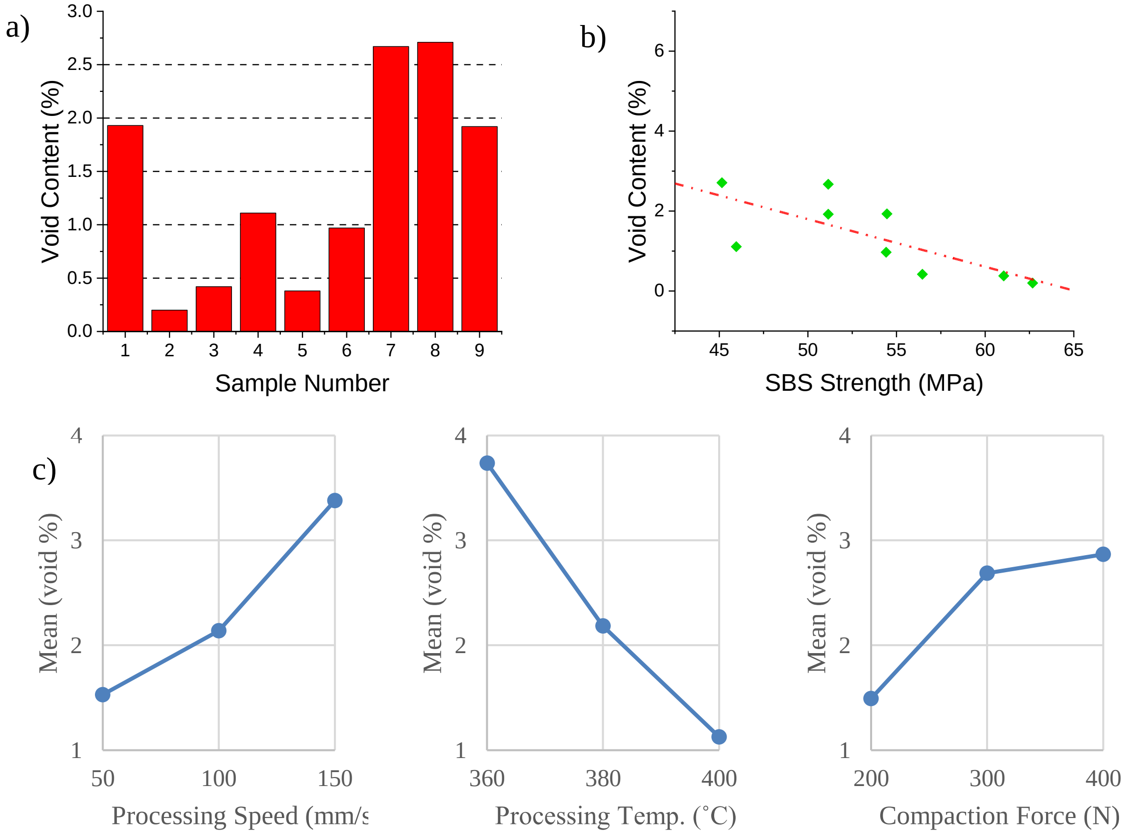

Figure 26: a) Void content for all samples, b) SBS strength vs. Void content, c) Taguchi analysis of processing parameters for void content.

Figure 27 shows simulated pressure and temperature contours at the instance where the third tape layer is being placed, i.e., pressure is applied on top of the third layer and heat flux is applied at the interface between the second and third layers. Pressure in the through the thickness direction is plotted, as only this component contributes to interlaminar bonding. It can be observed that the pressure is the highest directly beneath the roller, ignoring the pressure at the bottom of the first layer. On the other hand, temperature is the highest where the heat flux is applied, i.e., at the interface between the third and second layers and is diffused across a further distance due to the thermal conduction of fibers along the placement direction.

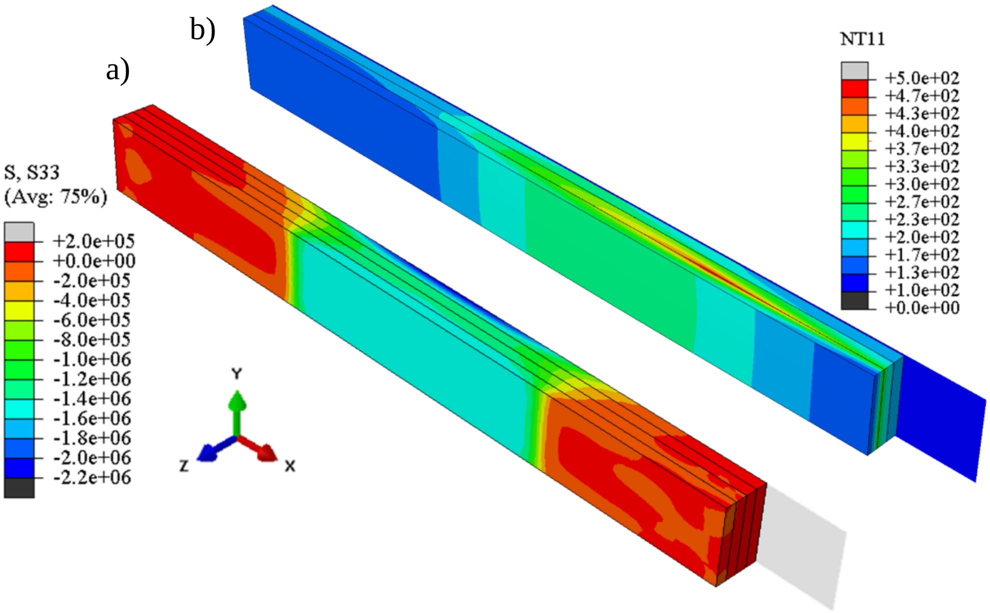

Figure 27: a) Pressure and b) temperature contours from FEA simulations during the placement of a third tape layer.

Figure 28 provides the simulated temperature and pressure histories for a node on the top surface of a tape during its placement, i.e., pressure is applied to the top surface of this tape, whereas heat flux is applied to the bottom surface of this tape. Pressure and temperature histories are also plotted as two subsequent tapes are placed on top of the node. Since the model size and compaction length were scaled down to reduce computational time during simulation, the compaction duration was scaled up to create a history profile that matches experiments. Upon deposition of the first layer onto the tool, temperature on the top side of the tape reaches a maximum of 350 ˚C, whereas when in direct contact with the laser during deposition of the second layer, node temperature reaches up to 500 ˚C. During the deposition of the third layer, the node's temperature only reaches 280 ˚C.

Pressure peak reaches its maximum during the deposition of each layer and declines during the placement of subsequent tape layers.

It is interesting that the tape's temperature reaches 500˚C once the laser (heat flux) passes over the node in question, but only for a fraction of a second. There are two notes regarding this result: i) it is well-known that PAEKs can be processed at 500 ˚C for seconds without degradation, and ii) the experimentally measured temperature near the nip point to be 400 ˚C. This may be due to the thermal camera's spatial and temporal resolution, and that laser heating might interfere with thermal measurements.

There are interesting insights to be learnt from simulation results. Each tape laid down during the AFP process undergoes full melting twice during layup, first when the tape is laid down and again when the subsequent layer is placed on top. When the 3rd and 4th layers are placed, the temperature in the 1st layer is elevated beyond the glass transition and cold crystallization temperatures. This repeated thermal loading enhances interlaminar bonding through repeated autohesion, eliminates voids, enhances intimate contact, and increases the crystallinity via cold crystallization. The cooling rate from melt is significant during ICAT, with material reaching T_g in less than 3 seconds after melting. Such a high cooling rate should result in crystallinities in the range of 5-10%. It can, however, be seen from temperature histories that each layer spends tens of seconds above its cold crystallization temperature (~225 ˚C), resulting in a relatively high degree of crystallinity, i.e., 20-25%. Upon close observation, the pressure is applied for a fraction of a second only (~0.5s) and is removed while the material is still well above T_g. Theoretically, there may be enough time for autohesion to complete; ~3 s according to Figure 28 where the node temperature is above T_g. However, removal of pressure while the material is near its melting temperature allows voids to redevelop. Additionally, successive crystallization of polymer at interfaces slows the rate of autohesion.

As discussed earlier, there is an increased number of voids within the top layer in tested samples, as shown in Figure 25b. Furthermore, DSC testing of the topmost layers resulted in a crystallinity of only 12%. This data suggests that as the tapes are deposited, they do not reach a low void content or fully develop crystalline structure until subsequent layers are deposited on top. In that, in situ consolidation AFP rely on repeated heating and compaction of subsequent layers to develop full bonding, high crystallinity, and low void content. Overall, modeling provides a qualitative understanding of the in-situ AFP process and proves that layups are subjected to very high cooling rates, a short period of intimate contact, and individual tapes are melted twice and subjected to temperatures above T_g with subsequent deposition of tapes on top.

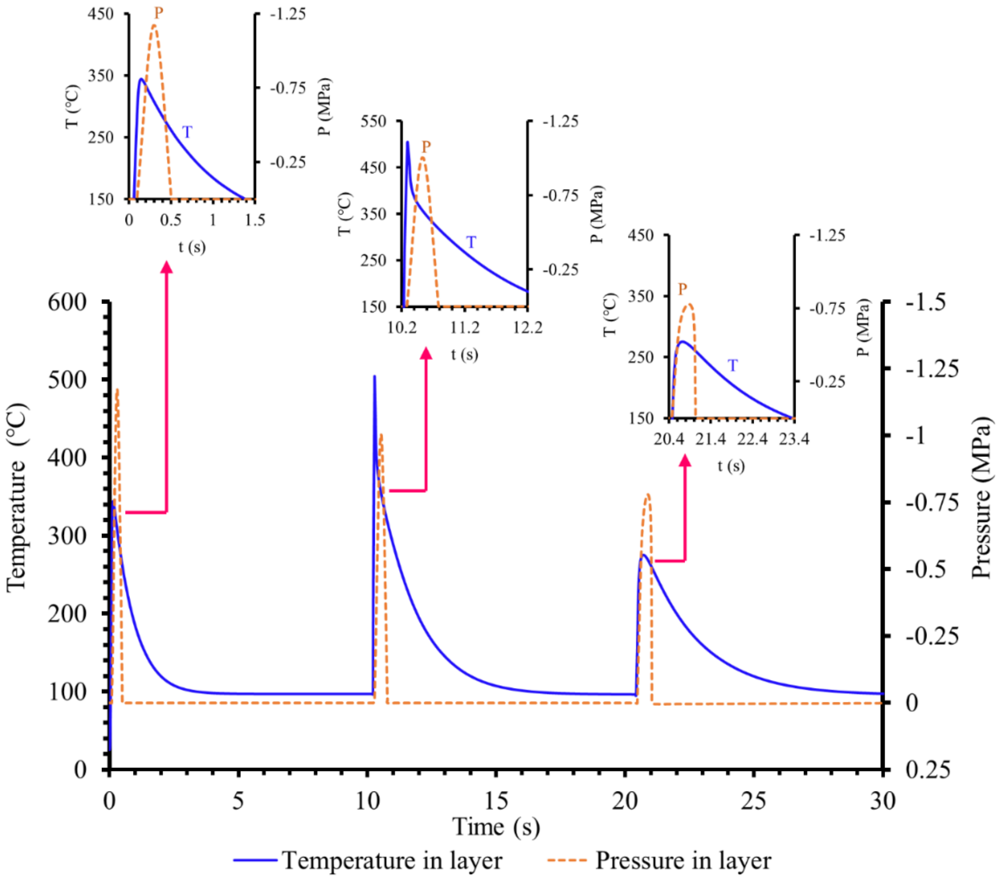

Figure 28: Pressure history and temperature history obtained from FEA ABAQUS simulation at the same node on the top of first layer during placement of three layer.

Samples tested in this study achieved a relatively high crystallinity (~20% or higher) and low void content (<2%). Intimate contact at tapes interfaces seems to have completed based on Figure 25c micrographs. Temperature histories suggest that autohesion has also progressed significantly. Putting all these facts together, it is still unclear why the SBS is only ~70% of compression molded samples. For reference, the tape manufacturer reports a maximum SBS of ~90 MPa for parts manufactured via an ideal compression molding process. Fractography was used to understand this discrepancy. SBS coupon fracture surfaces were imaged with a scanning electron microscope (SEM). First, the fracture surface of sample #2 was imaged, shown in Figure 29a. This image shows several carbon fibers pulled out of the matrix with little to no matrix still adhered. For comparison, thermoformed SBS coupons were prepared with near ideal properties. Fracture surface of this sample is shown in Figure 29b. In contrast to the AFP sample, fibers have matrix adhered to them and there is matrix plastic deformation. AFP samples, therefore, have a lower interfacial strength compared with the thermoformed one. This might be due to the fast cooling rate (>100 ºC/min) and repetitive heating during AFP, resulting in fiber-matrix interphases and residual stress developments that are different than those achieved in slow-cooled thermoformed samples.

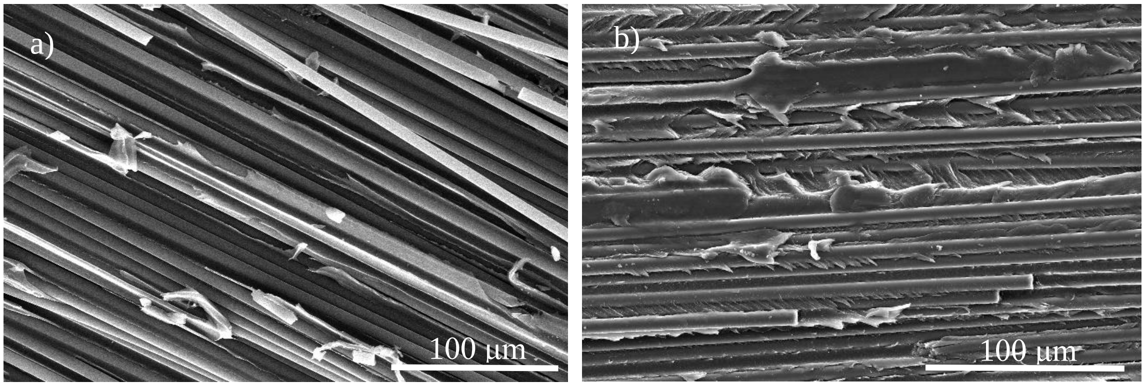

Figure 29: SEM image of clean fibers on fracture surface of a) sample #2, b) a compression molded, slow-cooled sample.

SUMMARY AND CONCLUSIONS

High-rate ICAT can theoretically retire autoclaves, resulting in significant energy and cost savings for composite manufacturing. This study demonstrates successful ICAT of carbon fiber LM-PAEK at up to 0.15 m/s. Increasing this speed by three times will likely result in widespread adoption of TPCs for large-scale aerospace structures. However, even at lower placement rates, it may be economical to use ICAT for manufacturing of small to medium-sized parts and structures for markets sch as urban air mobility and assistive technologies.

Effects of ICAT processing parameters on overall interlaminar bonding strength, void content, and crystallinity of samples were studied here. Simultaneously, finite element analysis was used to provide insights into bonding, void elimination/growth, and crystallization during ICAT. The best ICAT parameters resulted in a 63 MPa short beam strength, 23% crystallinity, and void content below 0.5%. While impressive, these samples only achieved ~70% of manufacturer reported SBS of compression molded samples, despite their similar void content and crystallinities. While residual stresses might be responsible for this lower bonding strength, fractography showed that another mechanism is definitely at play. Interfacial shear strength (fiber-matrix adhesion) was lower for ICAT samples compared with compression molded ones. Improving interfacial strength in ICAT parts is, therefore, necessary to achieve higher bonding levels and ICAT rates. Process modeling showed that deposited tapes are subjected to high cooling rates (100 °C/s) and remain above T_g after pressure from the compaction roller is removed. As a result, top layers of specimens show a higher void content and lower crystallinity than the bulk of the part. Repetitive heating and pressure from deposition of successive layers results in cold crystallization of polymer matrix, elimination of voids, and interlaminar bonding.

This study provides new understanding for unlocking the full potential of ICAT and mitigating its shortcomings. In addition to their potential for high-rate ICAT, thermoplastic composites can offer superior toughness, impact damage resistance, repairability, and weldability for joining parts. Specifically, carbon fiber LM-PAEK can also operate at temperatures as high as 250 °C. All these attributes make ICAT a potentially transformative manufacturing technology due to its dramatically reduced part acquisition cost (no autoclave or oven) and increased platform readiness via ease of repair of thermoplastics.

ACKNOWLEDGEMENTS

Authors are grateful for the research support provided by the Air Force Office of Scientific Research (AFOSR) under award no. FA9550-21-1-0066.

Chapter 6. Investigating Interlaminar Bonding and Fracture Toughness in In-Situ Consolidation Automated Fiber Placement of Carbon Fiber LM-PAEK Composites

Nathaniel T. Heathman, Joseph G Kirchhoff, Timothy Yap, and Mehran Tehrani

ABSTRACT

Fiber-reinforced thermoplastic composites (TPCs) offer advantages such as out-of-autoclave processability, high toughness, recyclability, weldability, and ease of repair. However, their use in the aerospace industry is limited due to challenges in large-scale manufacturing. The development of high-rate in situ consolidation automated fiber placement of TPCs (ICAT) is crucial to fully exploit the potential of TPCs. The authors' recent studies have investigated how processing parameters influence the formation of interlaminar bonds, voids, and crystallization in ICAT parts. This study aims to expand the understanding of bond strength and fracture toughness in ICAT. A laser-assisted automated fiber placement (AFP) machine is utilized to manufacture ICAT short beam shear (SBS) and Mode I and II fracture toughness coupons from carbon fiber-reinforced low-melt polyarylyletherketone (LM-PAEK) tapes. Specimens were fabricated at two different rates of 0.1 and 0.2 m/s. For comparative purposes, additional specimens were prepared using conventional thermoforming methods. Results from extensive testing and detailed fractography provide insights into how variations in void content, bonding, and crystallinity levels influence crack propagation and failure mechanisms in ICAT samples. This study reveals that high-quality ICAT parts (<1% void content) produced at a rate of 0.2 m/s and subjected to a straightforward low-temperature post-annealing step can achieve fracture toughness values on par with those of compression-molded samples, despite their lower SBS strength (50-60% of compression-molded samples).

This chapter contains material from the following publication: [102] SAMPE 2023 Conference

Author Contribution
Nathaniel H: Fabrication, testing, analysis
Joseph K: Data analysis
Timothy Y: Fabrication
Mehran T: Supervisor

INTRODUCTION

Thermoplastic composites (TPCs) are currently employed in the aerospace industry to facilitate the production of next-generation aircraft. They offer superior toughness, recyclability, and hygrothermal resistance. Moreover, TPCs can be welded together, significantly reducing manufacturing time and cost by eliminating the needs for fasteners and bonded joints, and more importantly. Owing to these unique attributes, TPCs have been successfully implemented in defense and commercial aerospace parts, however, they have yet to replace autoclave-cured thermosetting composites used in aircraft fuselages, wings, and other large aerostructures. It has proven difficult to manufacture large-scale thermoplastic structures.

TPC structures can be manufactured in relatively short cycle times (minutes to hours, compared to hours to days for thermosetting composites) using techniques such as stamp forming and over molding. However, these techniques have been limited to smaller components like panels or brackets due to press platen size constraints. Developing manufacturing technologies suitable for large-scale TPC structures without an oven, press, or autoclave is of great interest for the next generation of aircraft. Autoclaves, in particular, require substantial floor space and are energy-intensive, resulting in significant CO_2 emissions. The industry vision for the next generation of composite structures in aircraft focuses on enhancing efficiency, reducing production time, and minimizing environmental impact [103], [104].

A key strategy for realizing this vision involves high rate (>0.5m/s) in situ consolidation AFP of TPCs (ICAT), eliminating the need for any post-consolidation. ICAT is an additive manufacturing process that involves deposition of unidirectional carbon fiber/thermoplastic tapes, deemed towpregs, while simultaneously heating the tapes to melting temperature to form a bond between it and the previously deposited layer [71].

Since ICAT at high rates is challenging, an alternative method emphasizes utilizing multiple cooperating robots for in situ consolidation at lower rates (e.g., 0.1m/s), again achieving high manufacturing rates with multiple AFP heads. Another promising avenue entails depositing TPCs at the maximum speed AFP machines allow (~1m/s), followed by a relatively short post-oven consolidation using a vacuum bag-only (VBO) process. The final approach comprises employing compression molding after rapid AFP, ensuring optimal structural integrity while reducing production times.

Interlaminar bonding strength of a composite coupon is typically measured via short beam strength (SBS) test. Additionally, void analysis is key for understanding composite performance as porosity can degrade several critical mechanical properties of composites. Finally, for TPCs, a crystallinity measurement can reveal important information about the overall performance of the structure. Another critical design criteria for composites is their fracture toughness. Fracture toughness determines how well a material resists crack propagation under an increasing load, quantified by an energy release rate per unit surface area. Fracture toughness is conventionally tested in three different modes of pure tension (Mode I), pure shear (Mode II), and tearing (Mode III). Considering composites comprise of multiple layers of fibers and matrix, which often contain voids and defects, interlaminar cracks that can propagate through a panel are one of the most crucial threats to a composite structure. Given the broad usage of composite systems in manufacturing of aerospace and automotive components for the past 50 years, fracture toughness values for standard thermoset-based composites are well documented. However, in the case of a newly emerging thermoplastic composites market (both new materials and manufacturing techniques), fracture toughness values are more difficult to come by.

ICAT has been widely studied in previous research articles and is even utilized in some instances to manufacture components for end use applications; however, there are some key drawbacks to the process. Most significantly, ICAT parts do not exhibit the level of interlaminar bonding, low void content, and high crystallinity of their compression molded counterparts [97], [98], [66]. In a previous study on ICAT utilizing CF/LM-PAEK, an interlaminar bonding strength of 63 MPa, crystallinity of 23%, and void content below 0.5% were achieved for ideal processing parameter conditions [65]. The next step in providing a comprehensive understanding of ICAT with CF/LM-PAEK is to evaluate the fracture toughness performance of the material system and compare it to other prominent aerospace composite systems. Table 6 provides a comprehensive list of mode I and mode II fracture toughness values for various thermoset and thermoplastic composite systems.

Table 6: Fracture toughness values for various composite material systems: thermosets and thermoplastics

Material	**Manufacturing Method**	**G_{Ic} (kJ/m^2) DCB**	**G_{IIc} (kJ/m^2) ENF**	**Reference**
AS4/APC2 (Solvay)	HGT in-situ AFP	1.35 (25 µm steel shim)	N/A	[105]
AS4/PEEK (CETEX)	HGT in-situ AFP	0.331 – 0.376	N/A	[106]
CF/PEEK	ICAT	0.45 – 1.91	1.44 – 2.48	[107]
Toray TC1255 (LM-PAEK)	Compression Molding	2.1	2.6	[63]
Toray TC1200 (PEEK)	Compression molding	1.6	2.3	[108]
AS4/PEEK	Compression molding	1.26 – 1.68	1.2 – 1.77	[109]
T300/5208	Conventional	0.088-0.109	0.15 – 0.43	[109]
T300/914	Conventional	0.185	0.52 – 0.6	[109]
T300/F-185	Conventional	1.88	N/A	[109]
AS4/3501-6	Conventional	0.13 – 0.19	0.57 – 0.81	[109]
AS1/3501-6	Conventional	0.11 – 0.13	0.46 – 0.67	[109]
AS4/3502	Conventional	0.16 – 0.227	0.56	[109]
AS4 fabric/LY564	Conventional	0.72	3.5	[109]
IM7/8552	Conventional	0.2	1.1 – 1.67	[109]
IM7/E7T1	Conventional	0.18	1.1 – 2.45	[109]

A literature review of previous studies reveals no fracture toughness studies for CF/LM-PAEK. Instead, there is information on the fracture toughness values of ICAT CF/PEEK, a similar thermoplastic, along with general trends of how processing parameters affect their fracture toughness. This information can help draw generalized conclusions and insights about CF/LM-PAEK. In a study on how processing parameters of hot gas torch in-situ automated fiber placement (AFP) affect the strength of a composite, AS4-CF/PEEK specimens were manufactured and evaluated for their interlaminar shear strength (ILSS) and Mode I fracture toughness. Results of the parametric study show a maximum ILSS of 51 MPa at the lowest possible tape laying speed of 57 mm/s and a maximum mode I fracture toughness value (G_{Ic}) of 0.376 kJ/m^2, corresponding to a layup tool temperature of 150 ˚C. The researchers noted that G_{Ic} with a room temperature tool yielded 0.33 kJ/m^2 but had a sharp drop in toughness with a tool temperature of 65 ˚C with a G_{Ic} of 0.17 kJ/m^2. Furthermore, they were able to increase the toughness value to 0.49 kJ/m^2 by inserting a resin rich layer of PEEK between the interfaces [106].

In another study, Mode I and Mode II fracture toughness tests were carried out on a CF/PEEK composite panel manufactured by laser-assisted AFP. Mode I double cantilever beam (DCB) testing results showed values ranging from 0.45 kJ/m^2 to 1.91 kJ/m^2 for differing crack lengths. It is noted that G_{Ic} increased as the crack length increased and once reaching its peak value remained constant, a behavior observed in similar studies. For Mode II, end notched flexure (ENF) G_{IIc} values in the five tested samples ranged from 1.44 kJ/m^2 to 2.48 kJ/m^2 with the fracture toughness value increasing in a linear fashion as the crack length increased. In both mode I and mode II tests, resulting values paralleled those in corresponding studies of CF/PEEK manufactured by conventional methods, thus validating the potential for use of ICAT in manufacturing of aerospace components [107].

A third study on manufacturing CF/PEEK with in-situ consolidation via hot gas torch (HGT) AFP provided results for mode I and mode II fracture toughness tests. Processing parameters for the study were a layup speed of 76 mm/s, consolidation force of 180 N, HGT exit temperature of 950 ˚C, and tool temperature of 25 ˚C. Mode I testing results showed a maximum value of 1.4 kJ/m^2 with behavior similar to the previous study where G_{Ic} was higher during steady crack propagation than during crack initiation. Mode II testing results showed a maximum G_{IIc} value of 2.1 kJ/m^2, again presenting higher values for crack propagation than initiation. SEM analysis of the fracture surface showed a predominantly ductile fracture mode where cracks propagated through the polymer matrix with localized areas of brittle fracture. By comparing their results with those of conventionally manufactured coupons, which have lower G_{Ic} and G_{IIc}, the authors theorize that the increase in strength is due to a lower crystallinity produced by high cooling rates in the AFP process [105].

In a fourth study, CF/PEEK specimens were manufactured via ICAT and also via autoclave consolidation for direct comparison based upon their mode I fracture toughness and further characterized by crystallinity assessment and fractography. ICAT processing parameters for the study were a layup speed of 133 mm/s, laser power of 1350 W, roller pressure of 0.12 MPa, and tool temperature of 150 ˚C. Results from fracture toughness testing yielded a G_{Ic} initiation value of 1.32 kJ/m^2 and load arrest value of 0.92 kJ/m^2 for autoclave manufactured specimens and G_{Ic} initiation value of 2.15 kJ/m^2 and load arrest value of 1.67 kJ/m^2 for ICAT manufactured specimens. The ICAT specimens show an increase in fracture toughness versus the autoclave manufactured samples. Crystallinity analysis yielded a 42% crystallinity for autoclave specimens and 17.6% crystallinity for ICAT samples. Fractography showed a predominately ductile fracture for the ICAT sample with clean fiber surfaces, suggesting weak interfacial bonding between the fiber and matrix [110].

Results from the aforementioned studies provide evidence towards a correlation between fracture toughness in TPCs and the cooling rate from melt during manufacturing. To isolate effects of ICAT, results from a study on fracture toughness of CF/PEEK manufactured via compression molding with different cooling rates are presented. In this study mode I and mode II fracture toughness specimens are manufactured from APC-2 prepregs containing AS4 carbon fibers and a PEEK matrix. The samples were compression molded at 400 ˚C with a pressure of 1.38 MPa for 30 minutes. After which the specimens were cooled at different rates between 1 ˚C/min and 180 ˚C/min. The contrasting cooling rates provided samples sets with different levels of crystallinity and matrix/fiber interfacial strength. Testing results showed an increase in fracture toughness for the fast cooled samples over the slow cooled in both mode I and mode II tests. The authors utilized crystallinity measurements and SEM of the fracture surface to explain the reasoning behind results. It was found that slow cooled sample exhibited a higher crystallinity that led to brittle fracture of the matrix, where fast cooled samples with a lower crystallinity yielded ductile matrix failure. SEM observations led to the conclusion that slow cooled samples had a much higher interfacial bond strength than the fast cooled samples. The authors conclude the article by presenting the major findings, that interlaminar fracture toughness is dependent on the interaction between matrix ductility and fiber matrix interfacial bond strength. The improvement in fracture toughness for the fast cooled specimens is a result of the lower crystallinity and higher matrix ductility. However, the high fracture toughness for the resin system is unable to be fully translated to a high fracture toughness for the composite system due to a low interfacial strength and premature debonding of the matrix from fibers [111].

From the literature review, multiple key observations can be made on fracture toughness of ICAT specimens. First, in most studies it is observed that both mode I and II fracture toughness values are higher in ICAT samples than conventionally manufactured samples, even though ILSS is higher in thermoformed samples. Analysis of the fracture surfaces shows a predominantly ductile fracture for ICAT samples with localized brittle fracture and clean fibers, suggesting a weak interfacial strength but highly ductile matrix, which is consistent with the lower crystallinity of ICAT samples. Whereas thermoformed specimens show a mostly brittle fracture surface but a good level of interfacial bonding. Finally, significant differences in crystallinity are presented between the ICAT and thermoformed specimens, with ICAT typically producing a crystallinity that is half of the thermoformed CF/PEEK specimens. Taking these observations into account, crystallinity plays a major role in fracture toughness, in that, a lower crystallinity yields a matrix with increased ductility and, therefore, increased fracture toughness in both mode I and mode II. Given that the thermoformed samples have higher ILSS and better overall mechanical properties, there is a tradeoff between bulk strength and fracture toughness in ICAT and opens the door for fine-tuning performance based upon the situation loading. It is important to note that although a lower crystallinity is desirable for achieving higher fracture toughness in TPCs, it can adversely affect their chemical, humidity, and creep resistances.

Taking account of previous research into the topic, an experimental plan was developed to evaluate the fracture toughness of CF/LM-PAEK panels manufactured via ICAT. This is of importance given there are no studies of this material currently and while LM-PAEK is similar to PEEK, there are key differences in its molecular and crystalline structure. Standard modulus carbon fiber LM-PAEK 6.35 × 0.13 mm unidirectional tape was used for this study. Four sample types were manufactured with different ICAT parameters for comparison. Two in-situ consolidated samples were fabricated, at 100 and

200 mm/s rates. One sample was manufactured at 200 mm/s then annealed to improve its crystallinity since faster rates typically result in low crystallinities. The final panels were manufactured at 200 mm/s but using processing parameters chose intentionally to produce poor boding and high porosity, then post process consolidated utilizing compression molding. All panels were then tested for SBS, mode I fracture toughness, and mode II fracture toughness. Further characterization of the specimens was carried out by differential scanning calorimetry (DSC) to reveal crystallinity, cross sectional microscopy to analyze the microstructure, and SEM of the fracture surfaces to investigate fracture types.

EXPERIMENTATION

Materials

The feedstock tape used for this study is sourced from Suprem™ and is a LM-PAEK matrix reinforced with 55% volume fraction unidirectional carbon fibers. The tape measured 6.35 mm in width and 0.13 mm in thickness. The polymer matrix is synthesized by Victrex™, called AE250 LM-PAEK and is a recent development in the semicrystalline high performance polymer family that includes PEEK and PEKK. LM-PAEK provides similar mechanical and thermal properties to PEEK while offering a ~40 ˚C lower melt temperature. This is due to a reorganization of the polymer chains into co-polymer groupings that change the thermal, crystallization, and rheological characteristics of the material [62]. This enables a reduced viscosity during processing windows compared to PEEK/PEKK, promoting enhanced bonding.

Fabrication and Post Processing

All samples were fabricated using a laser-assisted AFP cell developed in house. The manufacturing cell utilizes a single tow AFP head, affixed to a KUKA robot, a 980 nm wavelength 600 W diode laser that is used for heating, and a conformable silicone compaction roller. All layups were performed on a heated layup tool at 150 ˚C to eliminate warpage and enhance crystallinity development.

Processing parameters for the in-situ samples were 100 mm/s and 200 mm/s velocity, 400 ˚C processing temperature, and 400 N compaction force. Processing parameters for the compression molded samples was 200 mm/s velocity, 300 ˚C processing temperature, and 200 N compaction force. In-situ samples manufactured at 100 mm/s are expected to provide specimens with good interlaminar bonding and high crystallinity, while in-situ samples manufactured at 200 mm/s are expected to provide a lower interlaminar bonding and lower crystallinity for comparison. The processing conditions for the compression molded samples were chosen to simulate a hi-rate layup where only “light tack” is achieved during layup and full consolidation is reached during post processing.

Three types of specimens were fabricated, SBS, Mode I, and Mode II fracture toughness, with specimen sizes prescribed by ASTM D2344 and ASTM D7905, respectively. The 100 mm/s, 200 mm/s, and annealed in-situ plates were fabricated at a different size than those intended for compression molding. In-situ SBS plates were manufactured at a size of 150 x 100 x 6 mm and cut down into five 40×12×6 mm specimens. In-situ Mode I were manufactured at a size of 200 x 175 x 3.4 mm and cut down into five 175×22×3.4 mm specimens with a 76 mm precrack insert. In-situ Mode II were manufactured at a size of 250 x 175 x 3.4 mm and cut down into five 225×22×3.4 mm specimens with a 50 mm precrack insert. Compression molded SBS plates were manufactured at a size of 180 x 175 x 6.5 mm and cut down into five 40×12×6 mm specimens after post processing. Compression molded Mode I and Mode II plates were manufactured at a size of 275 x 175 x 4.5 mm and cut down into five 200×22×6 mm specimens after post processing with a 76 mm precrack insert for Mode I and 50 mm precrack insert for Mode II. Plates for each type were laid up in the zero direction with a tow staggering pattern of 0%, 50%, 25%, 75%, where each tow in the subsequent layer is shifted relative to the previous layer by percentages stated. The staggering pattern is repeated every four layers and was determined to be the optimal method based upon previous research [112]. For the in-situ fracture toughness samples, the layups were paused at the middle layer and a sheet of 0.33 microns non-adhesive Kapton was inserted to form the precrack. For the compression molded fracture toughness samples, the layups were paused at the middle layer and a sheet of 0.13 microns stainless steel was inserted to form the precrack. Stainless steel was utilized for the compression molded samples due to its ability to withstand the post processing conditions.

Two different types of post processing conditions were utilized. Annealing was performed on the 200 mm/s in-situ coupons utilizing a high temperature oven and carried out in the following manner; samples were heated to 165 ˚C from room temperature at a 3 ˚C/min rate and held at that temperature for 30 minutes, then heated to 210 ˚C at a 3 ˚C/min rate and held at that temperature for 1 hour, after which the oven was turned off and samples were allowed to cool back to room temperature. All panels had 1 kg plates placed on top to minimize warpage during the annealing process. Compression molding was carried out with a compression molding press and aluminum molds were utilized to constrain the plates. During compression molding, the compression platens were heated to 310 ˚C. Once the temperature was reached, the mold was placed in the platens, and 0.2 MPa of pressure was applied by the platens on the mold. The platens and mold were then allowed to heat to 370 ˚C, and dwell at 370 ˚C for 25 minutes. After that, the pressure was increased to 2

MPa, and allowed to dwell for 5 minutes. After that, the heat was turned off and the platens and mold were allowed to cool to room temperature overnight. Pressure was removed after reaching room temperature.

Testing

SBS and fracture toughness testing was carried out with an MTS Criterion Model 43 universal test system, following the outlines provided by ASTM D2344, D5528, and ASTM D7905, respectively. All specimen sizes and precrack insert information is provided in the previous section. For Mode I fracture toughness testing, instead of piano hinges, machined loading blocks were fixed to the end of the dual cantilever beam specimens using Lord 310 A/B epoxy and loading was applied with a machined fixture. For Mode II fracture toughness testing, loading to the end notched flexure was applied in a three-point bending fixture with a bottom span length of 100 mm.

Compliance Calibration, Modified Beam Theory and Modified Compliance Calibration methods were all used to measure the G_{ic}. But Modified Beam Theory was used as it measured the most conservative values. It was observed that the standard deviation of G_{Ic} at different crack lengths varied per processing method. This variance was captured and compared at the processing method level. The variance is insight into the circuitous crack propagation path during loading.

For the G_{IIc} testing, the calculations were performed utilizing compliance calibration without a known flexural modulus. The flexural modulus for a beam at this span-to-length ratio was unknown. Instead, compliance calculations using beam theory were utilized. The approach requires a G_{13}, but it was approximated as G_{12} as 4.06 GPa [113]. The compliance correction factor, C_{SH}, accounts for the interlaminar shear deformations.

$$G_{IIc} = \frac{9a^2P^2(C-C_{SH})}{4bL^3[1+1.5\left(\frac{a}{L}\right)^3]} \tag{Equation 3}$$

$$C_{SH} = \frac{6L+3a-\frac{L^3}{a^2}}{20bhG_{13}} \tag{Equation 4}$$

Differential scanning calorimetry (DSC) was used to find the crystallinity of the matrix in the specimens. Crystallinity measurements were performed with a NETZSCH DSC 214. Samples were heated at 10 C/min up to 400 ˚C to reveal cold crystallization and enthalpy of melting values. Crystallinity was calculated with the following equation, with a fiber weight fraction of 66% provided by the manufacturer and an enthalpy of fusion of 130 J/g.

$$X_c = \frac{\Delta H_f + H_c}{\Delta H_f^{\circ} \times (1-W_f)} \tag{Equation 5}$$

Where X_c is the crystallinity of the material, ΔH_f is the enthalpy of fusion, H_c is the enthalpy of cold crystallization, ΔH°_f is the enthalpy of fusion for a hypothetically completely crystalline polymer, and W_f is the weight fraction of carbon fiber in the sample.

Optical microscopy of the layup cross sections was carried out by the following procedure. Cross sections parallel and perpendicular to the fibers were cut from the SBS coupon plates then mounted in fast cure epoxy. Samples were polished on a Struers polishing machine starting at 80 grit and progressively increasing the grit to 2000, followed by a final polishing with 3 µm suspension fluid. These samples were then imaged using a Keyence VK-X1100 Optical Profilometer. Void content was then calculated through segmentation of the cross sections in Object Research Systems Dragonfly software. Fracture toughness samples were cut to size, gold coated, and the fractured surface was imaged using a FEI Quanta 650 scanning electron microscope to reveal fracture mechanisms.

RESULTS AND DISCUSSIONS

ICAT coupons experience an extremely fast cooling from melt where nearly no crystallization occurs. At faster deposition rates, it is expected that the layers spend less time at elevated temperatures, in the cold-crystallization window. There is generally less time for cold-crystallization, intimate contact, and interdiffusion of polymer chains across layers with higher ICAT rates [65]. As shown in earlier chapters, repetitive heating and pressure application during AFP layup promotes all these mechanisms of consolidation. Consideration of SBS strength, mode I and mode II fracture toughness at varied processing speed is designed to provide insights into the processing influence on consolidation degree in tested coupons. Consolidation degree, measured through SBS and fracture toughness testing here, depends on several factors, including void content and shape, crystallinity degree and morphology, degree of intimate contact, and interdiffusion and entanglement of polymer chains. It is extremely difficult, if not entirely impossible, to measure some of these mechanisms directly and individually. However, their effects can be somewhat understood by comparing several samples fabricated under varying processing conditions.

Samples for DSC testing were taken from the middle of the SBS coupon as considered to be the best representative for crystallinity at the fracture surface for both SBS and fracture toughness samples. The DSC measured the heat flow (mW/mg) over a heat ramp from room temperature up to 400 ˚C at 10 ˚C/min to reveal cold crystallization and enthalpy of melting values. Figure 30 provides heat flow results from the DSC experiments and Table 7 provides calculated crystallinity values for all samples. Interestingly, the cold-crystallization window, measured at the 10 ˚C/min heating rate, is in the 170-200 ˚C rate, which is relatively low compared to PEEK. It was determined that the percentage of crystallinity in the 100 mm/s and 200mm/s specimens were 23% and 9%, respectively. Crystallinity values for the 200 mm/s post-annealed and compression molded samples were 25% and 27%, respectively. The results for ICAT samples suggest that despite the 100 mm/s samples, the 200 mm/s ones suffered from an insufficient time within the cold crystallization window. It should be noted that fast cooling (similar to ICAT rates) of the feedstock tape from melt results in crystallinity values of 6-9%. Furthermore, it can be inferred that the polymer morphology at the interlaminar interfaces is more amorphous for the higher processing speeds. A lower crystallinity promotes intimate contact and interdiffusion during AFP. Post-annealing, as utilized here, can subsequently yield the benefits of crystallization at the interfaces. For compression molded specimens, full crystallinity development was achieved as demonstrated by results from slow cooling in the DSC shown in previous chapters. Our understanding of semi-crystalline TPCs manufactured via compression molding suggests that amorphous microstructures tend to exhibit ductile behavior which is expected to result in higher fracture toughness values. For ICAT, however, bonding strength develops with crystallinity at the interface. A higher crystallinity in ICAT at the interlaminar interfaces may bring about a higher failure strength. Finally, it is expected that the crystal sizes in compression molded samples be much larger than those in ICAT ones, due to the slower colling rates resulting in less nucleation sites for spherulite growth [114].

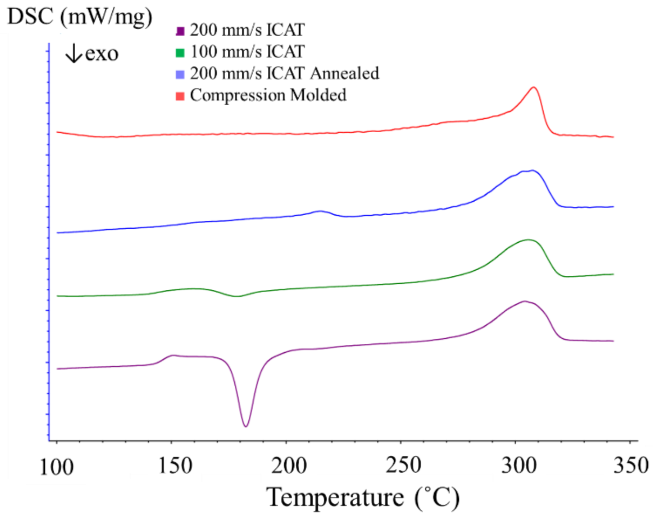

Figure 30: DSC curves for all tested specimens.

Table 7: Crystallinity values for all specimens

Specimen	***Crystallinity (%)***
Reference fast cooled sample	6-9
100 mm/s ICAT	23
200 mm/s ICAT	9
200 mm/s ICAT Annealed	25
Compression Molded	27
Reference slow cooled sample	30

Cross sections of the SBS coupons, imaged at 5X magnification, for all tested specimens are shown in Figure 31. At both processing speeds, the cross sections show a relatively homogeneous distribution of fibers and matrix, with some varying thickness in individual plies due to overlapping of the individual tows, which is most noticeable in the 200 mm/s in-situ specimen. Void analysis was performed on all four specimens by segmenting the cross sections to reveal void content as a percentage of the total volume. In all four instances, it was found that void content was below 1% with the 100 mm/s in-situ having a marginally lower void content than the 200 mm/s in-situ, but both annealed and compression molded having a lower void content than the in-situ samples. The low void content for the 200 mm/s in-situ sample is of particular significance when considering in previous studies conducted by the authors utilizing the same material, void content for specimens manufactured at 150 mm/s was above 2% [65]. Possible explanations for the lower void content could be the use of a thinner material in this study, or that the 150˚C layup tool temperature provided a mechanism for reduced void content compared to the 100˚C layup tool temperature used in the previous study [65]. The authors are unable to explain the lack of voids in the annealed sample. It was expected that the absence of pressure will ensure that there is no enhancement in resin flow, leading to lower void content and improved intimate contact.

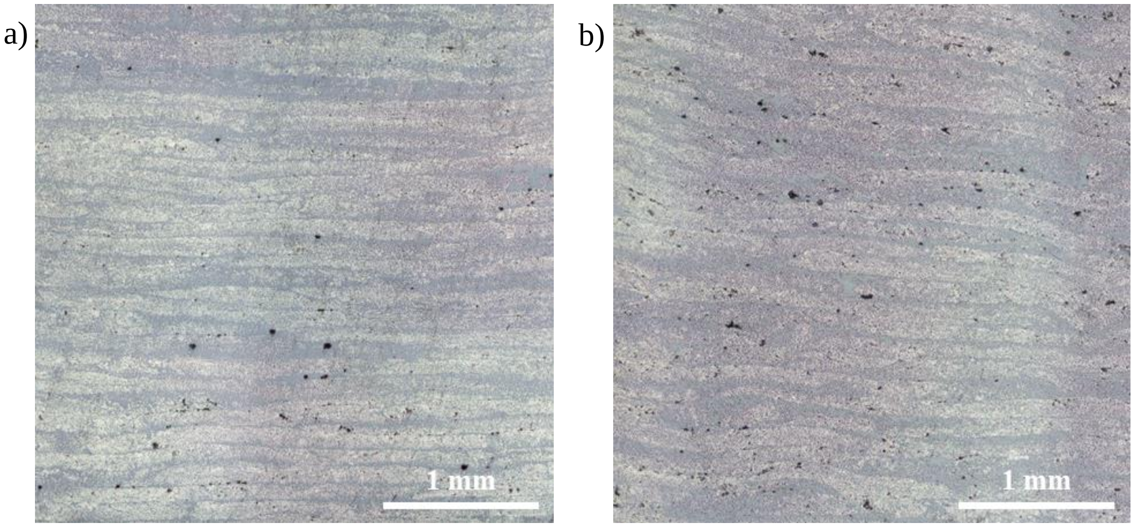

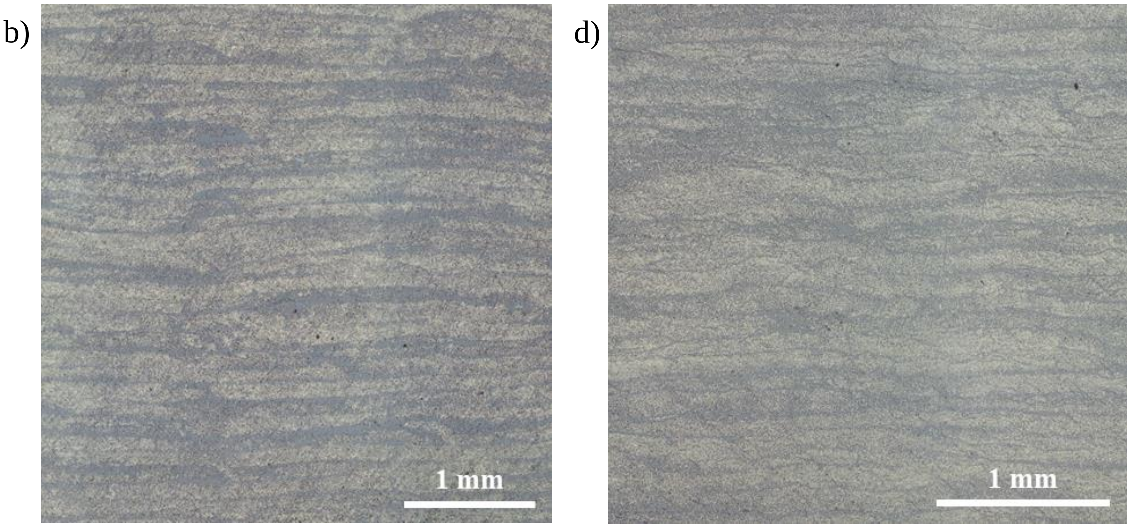

Figure 31: Cross section images of SBS coupons perpendicular to fibers at 10X, a) 100 mm/s in-situ, b) 200 mm/s in-situ, c) 200 mm/s in-situ annealed, d) Compression molded.

Figure 32 details the results from SBS testing specimens from each processing condition. In ICAT specimens there is a knockdown with increasing the processing speed, 57.7±0.8 MPa and 41.5 ±0.8 MPa for the 100 mm/s and 200mm/s rates, respectively. One of the 100 mm/s in-situ specimens was removed from the average calculations as it was an outlier. Upon further inspection, the specimen had an issue from machining. The DSC results showed that at the interface for the 200 mm/s in-situ sample, the crystallinity percentage was only 9% compared to 23% for the 100 mm/s sample. Annealing the 200 mm/s coupons resulted in an improvement of the SBS, increasing it from the aforementioned 41.5 ±0.8 MPa to 50.0±0.6 MPa. Measured SBS values for ICAT specimens are similar to previous studies using CF/LM-PAEK [63], [65].

The annealing temperature used, which was only 210°C, was not sufficiently high to promote interdiffusion. Given the low void fraction (similar observed intimate contact), it can be inferred that crystallization plays a crucial role in the development of strength between the layers. Specifically, interdiffused polymer chains from the crystals are believed to form bridges across the interfaces, thereby augmenting the bond strength. This observation may be particularly applicable to ICAT, considering that the time scales for interdiffusion may not be sufficiently long for polymer chains to entangle and develop strength. Compression molded samples yielded a SBS of 90.9±2.2 MPa, on par with values provided by the manufacturer for compression molded specimens [63]. In compression molding, the polymer is kept in a molten state to ensure complete flow and achieve a nearly perfect intimate contact between the layers. Following intimate contact development, polymer chains interdiffuse and entangle, reducing their mobility. Subsequently, these entangled chains undergo crystallization, which further enhances their bond strength. This process can lead to a maximum SBS between the layers, reaching up to 91 MPa. Despite having similar crystallinity, the in-situ 100 mm/s samples exhibit a higher SBS compared to the post-annealed specimens processed at 200 mm/s. This difference could be attributed to the higher level of intimate contact and interdiffusion achieved in the 100 mm/s sample. The slower processing speed allows for more time for the polymer chains to flow to form intimate contact and interdiffuse to form stronger bonds at the interfaces, leading to an enhanced SBS.

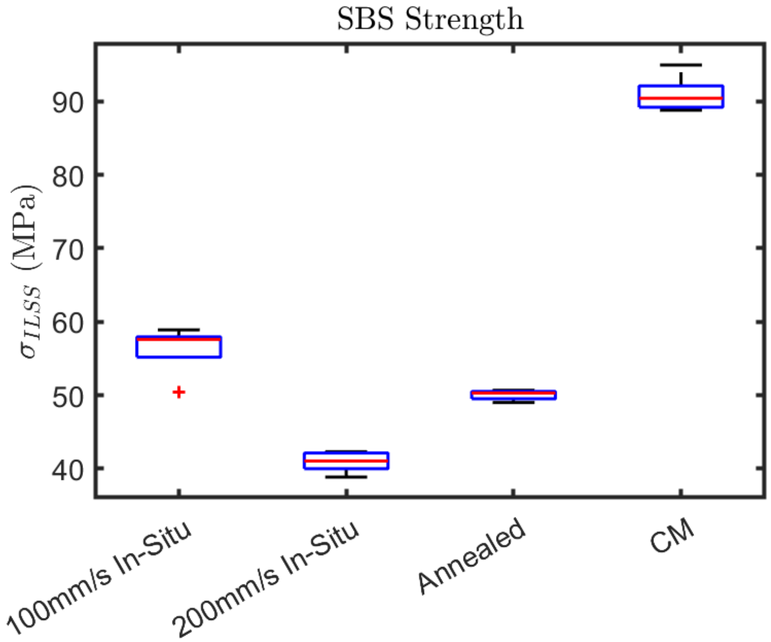

Figure 32: Box plot providing results from SBS testing for all processing conditions. Note: one of the 100 mm/s was an outlier and was removed from the median calculation for SBS strength but shown as a red cross.

Figure 33 provides a box plot summarizing the data from mode I fracture toughness testing for all processing conditions. For in-situ samples, the calculated average values were 1.8±0.1 kJ/m^2 and 1.8±0.2 kJ/m^2, for 100 mm/s and 200 mm/s, respectively. The 200 mm/s annealed and compression molded samples resulted in average values of 2.0±0.1 kJ/m^2, and 1.6±0.1 kJ/m^2, respectively. It is important to note that most measured values here are statistically similar, considering their deviations, and discussions here are to explain the slight differences in measured values. Results for the in-situ specimens suggest that processing speed has no effect on G_{Ic}. The interplay between crystallinity and bond strength can provide an explanation for this phenomenon. While the 200 mm/s in-situ sample has a more favorable (less) crystallinity, its bond strength is lower compared to the 100mm/s in-situ sample. These two opposing effects ultimately balance each other out, leading to identical mode I fracture toughness values for both tested AFP rates. The 200 mm/s annealed specimens yielded the highest G_{Ic} value, despite their high crystallinity. This can be attributed to the small crystal sizes that are nucleated throughout the fast-cooling stage and grow during cold crystallization. Small crystals result in a more ductile behavior and a more tortuous path for crack propagation. Finally, the compression molded and slowed cooled sample offered the lowest G_{Ic} value of the tested samples. This can be attributed to the high crystallinity and the formation of large spherulites that are commonly observed during the slow cooling process from the molten state in compression molded samples. While conclusions are drawn here based on the bulk crystallinity values, the degree of crystallinity as well as crystal/polymer morphology at the newly formed interfaces control fracture toughness.

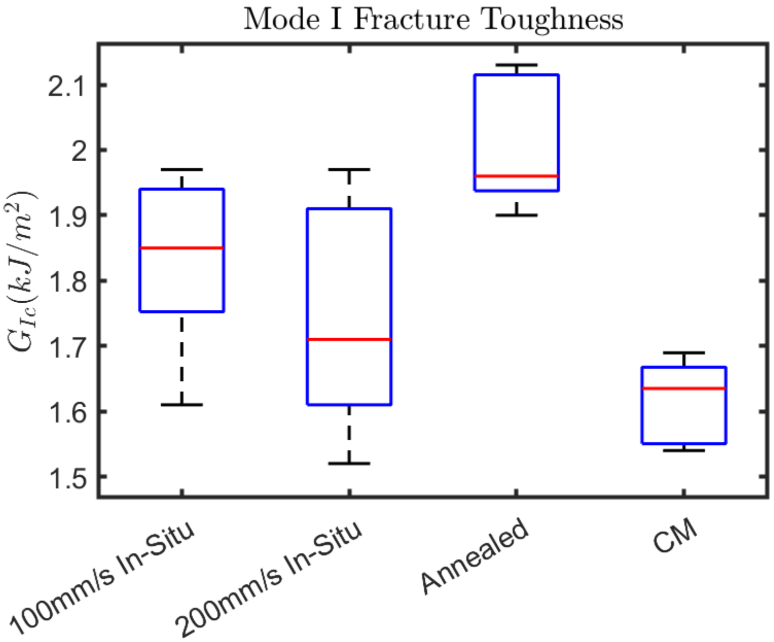

Figure 33: Box plot providing results from Mode I fracture toughness testing for all processing conditions.

Figure 34 includes the results for Mode II fracture toughness tests. For in-situ specimens the calculated average values were $2.4 \pm 0.4\ kJ/m^2$ and $2.1 \pm 0.4\ kJ/m^2$ for 100 mm/s and 200 mm/s rates, respectively. For post processed specimens, the calculated average values were $1.4 \pm 0.3\ kJ/m^2$ and $2.7{\pm}0.3\ kJ/m^2$ for the 200 mm/s annealed and compression molded coupons, respectively. It can be observed that the bonding strength seems to dominate fracture toughness values for the in-situ specimens despite their dissimilar crystallinities, similar to Mode I results. The results for the post-processed specimens exhibit an inverse trend compared the Mode I results, where the annealed samples suffer a drastic reduction in fracture toughness, while the compression molded samples demonstrate the highest fracture toughness among all the tested specimens. Explaining these results based on crystallinity data alone is not possible. Fractography can be, however, used to find mechanisms responsible for the measured values and hopefully explain the observed trends.

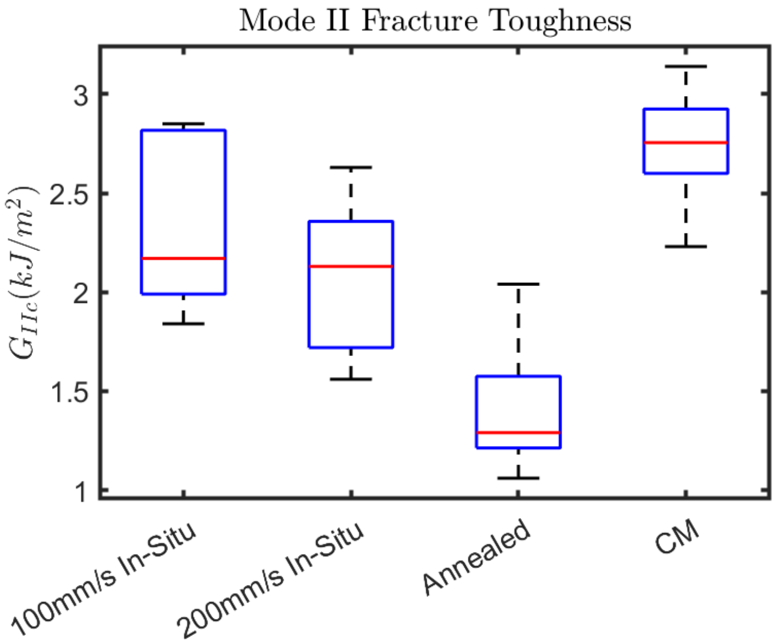

Figure 34: Box plot providing results from Mode II fracture toughness testing for all processing conditions.

Fracture surfaces for Mode I and II specimens are shown in Figure 35 and Figure 36, respectively. Given the significant difference in crystallinities between the in-situ samples, the expectation based upon previous studies is to witness ductile fracture mechanisms in the low crystallinity samples (200 mm/s processing speed) and brittle fracture mechanisms in the high crystallinity samples (100 mm/s processing speed). Whereas both the annealed and compression molded samples are expected to exhibit brittle fracture mechanisms. Analysis of the SEM images for the 100 mm/s in-situ samples for both Mode I and Mode II tests, Figure 35a and Figure 36a, exhibits predominately brittle fracture with presence of hackles in the remaining matrix structures, a large amount of clean fibers, and limited signs of plastic deformation. On the contrary, the 200 mm/s in-situ fracture surfaces, Figure 35b and Figure 36b, suggest pure ductile fracture due to an absence of hackles and the significant signs of matrix plastic deformation, where the matrix is pulled from the fibers and stretched before fracturing. In both 100 mm/s and 200 mm/s in-situ samples, fiber bridging is present, which can help improve the fracture toughness. The 200 mm/s annealed specimens exhibit contrasting fracture types between Mode I and Mode II tests. Figure 35c presents the Mode I fracture surface for this specimen where like the 200 mm/s in-situ sample, a large amount of plastic deformation in the remaining matrix is observed suggesting ductile fracture. Furthermore, these samples contained a significant amount of fiber bridging and even whole bundles of fibers pulled from the bulk of the sample. However, in the Mode II fracture surface, shown in Figure 36c, a large amount of the matrix is sheared clean off the remaining fibers and plastic deformation of the matrix is limited. These contrasting fracture types may help explain the differences in Mode I and Mode II results for the 200 mm/s annealed sample. Fracture surface images of the compression molded samples, presented in Figure 35d and Figure 36d, are significantly different than the previous three specimens. In both Mode I and Mode II images, a mixed mode fracture type is revealed by the presence of both hackles/river marks as well as local microscale matrix plastic deformation. In the compression molded samples, evidence of fiber bridging was nonexistent. Also observed are the fibers on the fracture surface containing a large amount of matrix still adhered to the surface, suggesting a much stronger matrix interphase region than the in-situ and annealed samples.

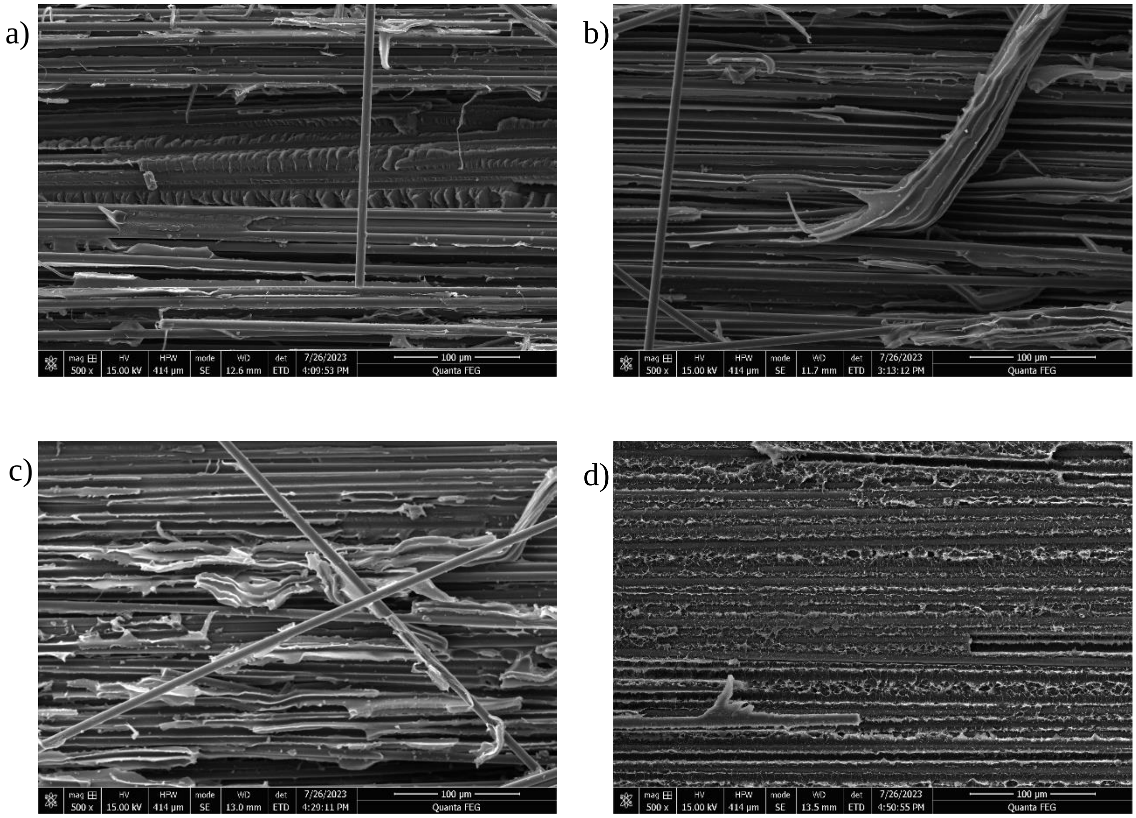

Figure 35: SEM of Mode I fracture surface, a) 100 mm/s in-situ b) 200 mm/s in-situ, c) 200 mm/s annealed, d) Compression molded.

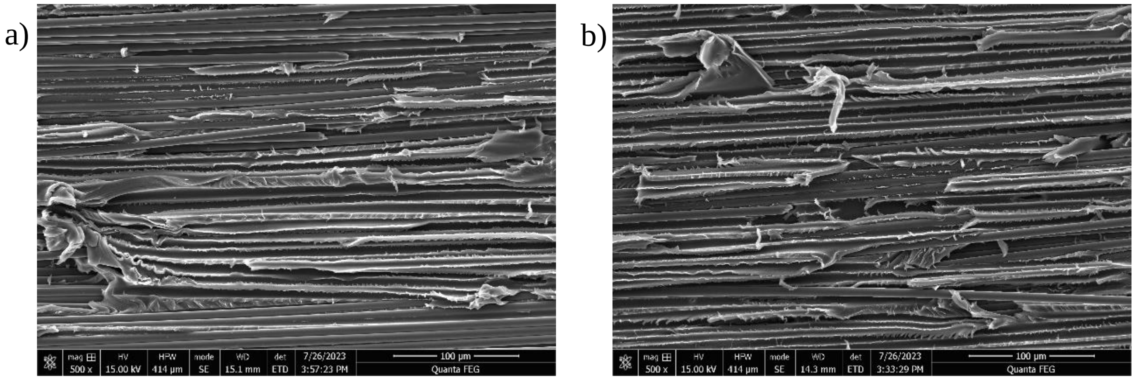

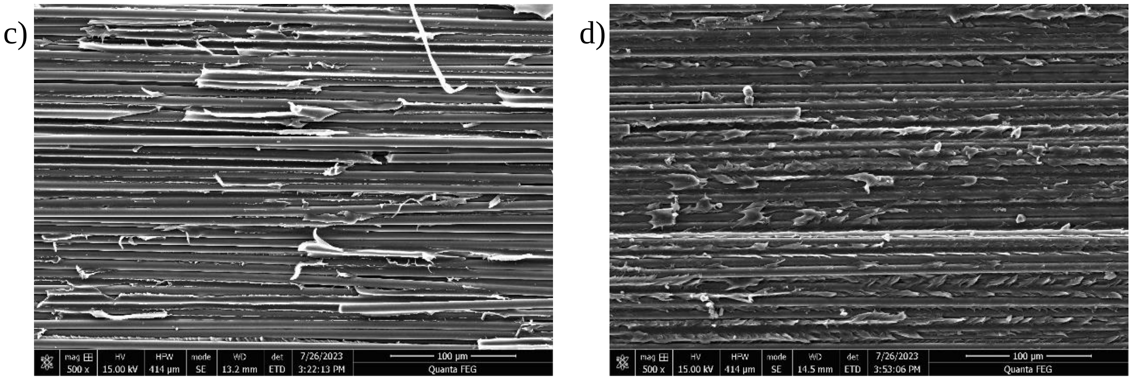

Figure 36: SEM of Mode II fracture surfaces, a) 100 mm/s in-situ, b) 200 mm/s in-situ, c) 200 mm/s annealed, d) Compression molded.

SUMMARY AND CONCLUSIONS

The aim of this study was to explore the relationship between interlaminar bond strength and crystallinity of ICAT coupons with their Mode I and Mode II fracture toughness and related crack energy absorption mechanisms. The findings clearly show that increasing the processing speed influences both the layer-to-layer bond strength and crystallinity. A higher bonding strength, associated with both extended polymer diffusion times across layers and increased cold crystallinity, suggests enhanced SBS strength but introduces a brittle failure mode.

Based on previous research, it was hypothesized that fracture toughness would increase at higher processing speeds as the ductility of the interface increases due to reduced crystallinity. However, the ICAT experiments conducted at 100 mm/s and 200 mm/s yielded the opposite results. The interface for the 200 mm/s samples achieved a crystallinity of only 9% compared to 23% for 100 mm/s. As processing speeds increased, both SBS strength and fracture toughness decreased, with SBS strength falling from 58±1 to 41±1 MPa. The G_{Ic} values were 1.8±0.1 kJ/m^2 and 1.8±0.2 kJ/m^2 for 100 mm/s and 200 mm/s, respectively. The G_{IIc} values were 2.4±0.4 kJ/m^2 and 2.1±0.0 kJ/m^2 for 100 mm/s and 200 mm/s, respectively. Complicating the understanding of the relationships between SBS, crystallinity, and fracture toughness even further were the results from the 200 mm/s annealed and compression molded specimens. The 200 mm/s annealed specimens displayed the highest G_{Ic} but lowest G_{IIc}, while compression molded specimens exhibited the lowest G_{Ic} but highest G_{IIc}.

Investigations into the microstructure revealed that the void content, measured via cross sectional optical microscopy, was below 1% for all specimens, indicating that both in-situ and annealed specimens achieved adequate intimate contact. SEM fractography of the fracture surface of in-situ specimens demonstrated that low crystallinity, as per the 200 mm/s in-situ specimens, tends towards ductile fracture, whereas higher crystallinity, as in the 100 mm/s in-situ specimens, results in a more brittle behavior. Interestingly, the annealed specimens showed contrasting fracture types between Mode I and Mode II tests, and the compression molded specimens displayed mixed mode fracture types in both.

Overall, the results do not offer a distinctive explanation for the variation in fracture toughness values. Contrary to findings in previous studies, the development of high fracture toughness appears to depend on a combination of interlaminar bonding, crystallinity development, spherulite size and alignment, transcrystallinity, and interphase strength. These findings should prompt further scientific investigation into the polymer physics at the interfaces.

ACKNOWLEDGEMENTS

Authors are grateful for the research support provided by the Air Force Office of Scientific Research (AFOSR) under award #FA9550-21-1-0066 and the NASA NSTGRO22 Grant #80NSSC22K1203.

Chapter 7: Conclusions and Future Work

The presented body of work focuses on manufacturing and processing of carbon fiber reinforced LM-PAEK via automated fiber placement and fused filament fabrication. Thermoplastic composites offer various benefits compared to thermosetting ones, including increased toughness, recyclability, weldability, and ease of repair. They also offer the ability to be in-situ consolidated, however, several limitations are currently present. Specifically, low interlaminar bonding, weak matrix/fiber adhesion, high void content, and low crystallinity. Several studies were carried out to investigate these drawbacks, providing information on the resulting thermal and mechanical properties of the material as well as key insights into their bonding and failure mechanisms. Overall, the presented work provides a foundation for understanding the current state of the art and identifies avenues for advancement towards high-performance applications.

The opening study presented in Chapter 2 investigates the post processing of CF/PEKK parts, manufactured via FFF, focusing on the interlaminar bonding strength. Tensile specimens were manufactured in the Z direction to measure interlaminar failure. Samples were subjected to post processing methods to investigate two separate methods of interlaminar bonding enhancement. The first being hot isostatic pressing at varying pressures at a temperature right above T_g to enhance intimate contact, but not crystallinity The second being an annealing process in the cold crystallization window to enhance crystallinity, but not intimate contact. Results showed an almost complete reduction of internal voids from the HIP process, maximizing intimate contact, but no significant increase in interlaminar bonding. Conversely, annealing within the cold crystallization window showed no enhancement of intimate contact, a significant increase in crystallinity, and major improvement in interlaminar bonding. The findings suggest, while removal of voids enhances intimate contact, this alone does not drive an increase in interlaminar bonding. Improving crystallinity through annealing, coupled with the possibility of polymer chain diffusion across the interfaces, is the dominant mechanism for increasing interlaminar bonding.

Chapter 3 presents a study in which CF/LM-PAEK was utilized in a novel from of additive manufacturing, deemed continuous fiber fused filament fabrication. In this research, parts were fabricated using the mentioned form of FFF and analyzed to reveal formerly unknown mechanical properties. Additionally, an investigation into void development, fiber steering, and crystallization kinetics was performed. Results showed the material system was capable of achieving levels of interlaminar bonding and flexural strength that greatly surpassed those produced by discontinuous fiber FFF and even exceeded values of CF/PEEK manufactured by the same technology. Analysis of the crystallization kinetics of the resulting parts revealed that while a high crystallinity was achieved near the build plate, it decreased as height from the build plate increased. However, a uniform crystallinity was achieved through post process annealing. Void development was studied through cross sectional microscopy and µCT analysis. It was discovered that while void content was relatively low for areas where the fibers travel in a straight line, areas where fibers were steered around a corner suffered from a higher void content due to the inability of the filaments to conform to the programmed path.

Chapter 5 provides a study in which a laser assisted automated fiber placement manufacturing cell, developed at UT Austin and explained in detail in Chapter 4, is utilized to investigate the effect of processing parameters on resulting interlaminar bonding, crystallization kinetics, and void development. A partial factorial design of experiments was built, varying tool velocity, processing temperature, and compaction force, from which nine samples of CF/LM-PAEK were manufactured and tested. Results showed the highest achievable level of interlaminar bonding, ~60 % that of compression molded, resulted from a low velocity, highest processing temperature, and highest level of compaction pressure. Further analysis of the best performing sample yielded a void content close to 1% and crystallinity close to the maximum achievable. To provide further analysis of the mechanisms driving the resulting properties, a finite element model was constructed to predict temperatures and pressures in a deposited tape upon first placement and subsequent layers placed on top. Considering all physical and modeling results, it was found that parts manufactured with this process suffer from high cooling rates that results in a low crystallinity, low interfacial strength, and high void content. The process relies on the repeated heating and compaction from multiple deposited layers to enable polymer chain diffusion, build up crystallinity, and eliminate voids. However, interfacial strength in a finished part is still low, which drives the reduction in interlaminar bonding when compared to those manufactured by compression molding.

Chapter 6 builds off the work presented in Chapter 5, where ICAT is utilized to manufacture CF/LM-PAEK parts, but this study investigates how varying processing parameters affect the fracture toughness and interlaminar bonding of resulting parts. Samples were manufactured at two different processing speeds to produce one sample set with a high level of interlaminar bonding, yet brittle matrix, and another sample set with low level of interlaminar bonding, yet ductile matrix. Two additional sets of post processed samples were prepared for comparison, a high-rate in-situ sample set that was annealed, and a compression molded sample set. The hypothesis that a highly ductile matrix would improve fracture toughness, regardless of interlaminar bonding, was tested. Results from testing showed specimens exhibited the expected failure type, however, fracture toughness values were not dependent on fracture mechanisms alone. It was found that for Mode I, the morphology developed through cold crystallization provided the dominate mechanism for an enhanced fracture toughness. For Mode II, it was found that interlaminar bonding and interfacial strength were the most important factors in developing a high fracture toughness. Overall, the study proved that fracture toughness is dependent on a complex combination of interlaminar bonding, matrix ductility, interfacial strength, and crystallization kinetics, specifically spherulite and transcrystalline morphologies.

FUTURE WORK

The additive manufacturing techniques and materials presented in this work are novel to the industry and have yet to be adopted on a widespread basis for use in high-performance applications. While the findings presented in this dissertation lay the groundwork for the technological advancement of these manufacturing processes, several immediate opportunities for further research arise. Examples of these opportunities are provided below.

In the work on post-processing CF/PEKK manufactured by FFF, it was found that HIP could remove voids but did not enhance strength as anticipated. In contrast, higher temperature annealing enhanced interlaminar strength but did not reduce the number of voids. However, these two techniques were not combined. This gap offers an opportunity for further studies into a refined post-processing technique that utilizes both HIP and annealing to remove voids and improve interlaminar bonding and crystallinity.

The research presented on continuous fiber FFF of CF/LM-PAEK demonstrates the ability to manufacture high-strength parts, yet these parts suffer from a high void content in curved sections of the layup. Considering that one of the main advantages of FFF is freeform fabrication ability, curved sections are prominent in most designs. This observation opens the door for a deeper understanding of fiber steering and how to mitigate this issue through changes to the software or hardware.

A significant portion of this dissertation was dedicated to the investigation of ICAT using CF/LM-PAEK. While a substantial number of findings and insights into the technology are presented, this area of focus also provides the largest scope for further work. In both studies, it was identified that ICAT results in parts with low interfacial strengths between the matrix and fibers, yet the underlying mechanisms remain unexplored. Conducting a study to correlate processing parameters to interfacial strength and investigating a method to maximize this value is one possible opportunity for future investigation.

Another key mechanism worth further investigation is crystallization kinetics on fiber surfaces and in the matrix, as they govern interlaminar strength and fracture toughness. The studies in this body of work present crystallinity values but do not provide detailed insight into this phenomenon. Furthermore, little to no insight is provided on crystallinity development on the surface of the fibers, known as transcrystallinity. This creates an opportunity to study the micromechanics of the crystallization process and correlate processing conditions to detailed information about transcrystallinity and spherulite size and distribution. It also provides an opportunity to determine how these traits affect the overall interlaminar bond strength.

References

[1] K. Yassin and M. Hojjati, “Processing of thermoplastic matrix composites through automated fiber placement and tape laying methods: A review,” *J. Thermoplast. Compos. Mater.*, vol. 31, no. 12, pp. 1676–1725, Dec. 2018, doi: 10/gfsffz.

[2] A. Khodaei and F. Shadmehri, “Intimate contact development for automated fiber placement of thermoplastic composites,” *Compos. Part C Open Access*, vol. 8, p. 100290, Jul. 2022, doi: 10.1016/j.jcomc.2022.100290.

[3] O. Çelik, D. Peeters, C. Dransfeld, and J. Teuwen, “Intimate contact development during laser assisted fiber placement: Microstructure and effect of process parameters,” *Compos. Part Appl. Sci. Manuf.*, vol. 134, p. 105888, Jul. 2020, doi: 10/gjmpxz.

[4] F. Yang and R. Pitchumani, “Healing of Thermoplastic Polymers at an Interface under Nonisothermal Conditions,” *Macromolecules*, vol. 35, no. 8, pp. 3213–3224, Apr. 2002, doi: 10.1021/ma010858o.

[5] H. Pérez-Martín, P. Mackenzie, A. Baidak, C. M. Ó Brádaigh, and D. Ray, “Crystallinity studies of PEKK and carbon fibre/PEKK composites: A review,” *Compos. Part B Eng.*, vol. 223, p. 109127, Oct. 2021, doi: 10/gnxv6p.

[6] A. J. Comer *et al.*, “Mechanical characterisation of carbon fibre–PEEK manufactured by laser-assisted automated-tape-placement and autoclave,” *Compos. Part Appl. Sci. Manuf.*, vol. 69, pp. 10–20, Feb. 2015, doi: 10.1016/j.compositesa.2014.10.003.

[7] D. Saenz-Castillo, M. I. Martín, S. Calvo, F. Rodriguez-Lence, and A. Güemes, “Effect of processing parameters and void content on mechanical properties and NDI of thermoplastic composites,” *Compos. Part Appl. Sci. Manuf.*, vol. 121, pp. 308–320, Jun. 2019, doi: 10.1016/j.compositesa.2019.03.035.

[8] N. Heathman, T. Yap, and Mehran Tehrani, “Hot Isostatic Pressing to Enhance Inter-Laminar Tensile Strength of Additively Manufactured Carbon Fiber-PEKK Parts,” *Proc. 35th Annu. Am. Soc. Compos. Tech. Conf. 2020*.

[9] C. Pandelidi, S. Bateman, S. Piegert, R. Hoehner, I. Kelbassa, and M. Brandt, “The technology of continuous fibre-reinforced polymers: a review on extrusion additive manufacturing methods,” *Int. J. Adv. Manuf. Technol.*, vol. 113, no. 11–12, pp. 3057–3077, Apr. 2021, doi: 10.1007/s00170-021-06837-6.

[10] Toray, “Toray Cetex TC1225.” [Online]. Available: https://www.toraytac.com/media/3bd72fac-0406-48e4-bfc4-2ffd2398ac0c/zipxIA/TAC/Documents/Data_sheets/Thermoplastic/UD%20tapes,%20prepregs%20and%20laminates/Toray-Cetex-TC1225_PAEK_PDS.pdf

[11] M. Rinaldi, T. Ghidini, F. Cecchini, A. Brandao, and F. Nanni, “Additive layer manufacturing of poly (ether ether ketone) via FDM,” *Compos. Part B Eng.*, vol. 145, pp. 162–172, Jul. 2018, doi: 10.1016/j.compositesb.2018.03.029.

[12] N. van de Werken, H. Tekinalp, P. Khanbolouki, S. Ozcan, A. Williams, and M. Tehrani, “Additively manufactured carbon fiber-reinforced composites: State of the art and perspective,” *Addit. Manuf.*, vol. 31, p. 100962, Jan. 2020, doi: 10/ghgkm8.

[13] W. Wu, P. Geng, G. Li, D. Zhao, H. Zhang, and J. Zhao, “Influence of Layer Thickness and Raster Angle on the Mechanical Properties of 3D-Printed PEEK and a Comparative Mechanical Study between PEEK and ABS,” *Materials*, vol. 8, no. 9, pp. 5834–5846, Sep. 2015, doi: 10.3390/ma8095271.

[14] N. van de Werken, J. Hurley, P. Khanbolouki, A. N. Sarvestani, A. Y. Tamijani, and M. Tehrani, “Design considerations and modeling of fiber reinforced 3D printed parts,” *Compos. Part B Eng.*, vol. 160, pp. 684–692, Mar. 2019, doi: 10/gfv375.

[15] Li, Zhao, Li, Yang, and Wang, “Flexural Properties and Fracture Behavior of CF/PEEK in Orthogonal Building Orientation by FDM: Microstructure and Mechanism,” *Polymers*, vol. 11, no. 4, p. 656, Apr. 2019, doi: 10.3390/polym11040656.

[16] H. Liu, X. Cheng, X. H. Yang, G. M. Zheng, and Q. J. Guo, “Experimental study on parameters of 3D printing process for PEEK materials,” *IOP Conf. Ser. Mater. Sci. Eng.*, vol. 504, p. 012001, Apr. 2019, doi: 10.1088/1757-899X/504/1/012001.

[17] G. Cicala, A. Latteri, B. Del Curto, A. Lo Russo, G. Recca, and S. Farè, “Engineering Thermoplastics for Additive Manufacturing: A Critical Perspective with Experimental Evidence to Support Functional Applications,” *J. Appl. Biomater. Funct. Mater.*, vol. 15, no. 1, pp. 10–18, Jan. 2017, doi: 10.5301/jabfm.5000343.

[18] van de Werken, Nekoda, Koirala, Pratik, Ghorbani, Jafar, Abel, Matthew, and Tehrani, Mehran, “Improving Properties of Additively Manufactured Carbon Fiber Composites via Post Pressing.pdf,” *Am. Soc. Compos. 2019*.

[19] N. van de Werken, P. Koirala, J. Ghorbani, D. Doyle, and M. Tehrani, “Investigating the hot isostatic pressing of an additively manufactured continuous carbon fiber reinforced PEEK composite,” *Addit. Manuf.*, vol. 37, p. 101634, Jan. 2021, doi: 10.1016/j.addma.2020.101634.

[20] C. Yang, X. Tian, D. Li, Y. Cao, F. Zhao, and C. Shi, “Influence of thermal processing conditions in 3D printing on the crystallinity and mechanical properties of PEEK material,” *J. Mater. Process. Technol.*, vol. 248, pp. 1–7, Oct. 2017, doi: 10.1016/j.jmatprotec.2017.04.027.

[21] E. de Avila, J. Eo, J. Kim, and N. P. Kim, “Heat Treatment Effect on Mechanical Properties of 3D Printed Polymers,” *MATEC Web Conf.*, vol. 264, p. 02001, 2019, doi: 10.1051/matecconf/201926402001.

[22] V. Kishore, C. Ajinjeru, and C. Duty, “RHEOLOGICAL CHARACTERISTICS OF FIBER REINFORCED POLY(ETHER KETONE KETONE) (PEKK) FOR MELT EXTRUSION ADDITIVE MANUFACTURING,” p. 10.

[23] S.-L. Gao and J.-K. Kim, “Cooling rate influences in carbon fibre/PEEK composites. Part 1. Crystallinity and interface adhesion,” *Compos. Part Appl. Sci. Manuf.*, vol. 31, no. 6, pp. 517–530, Jun. 2000, doi: 10.1016/S1359-835X(00)00009-9.

[24] Chumaevskii, A.V., Tarasov, S. Yu., Filippov. A.V., Kolubaev, E. A., Rubtsov, V. E., and Eliseev, A. A., “Mechanical Strength of Additive Manufactured Carbon Fiber Reinforced Polyetheretherketone,” *AIP Conf. Proc. 2016*.

[25] R. R. Fernandes, N. van de Werken, P. Koirala, T. Yap, A. Y. Tamijani, and M. Tehrani, “Experimental investigation of additively manufactured continuous fiber reinforced composite parts with optimized topology and fiber paths,” *Addit. Manuf.*, vol. 44, p. 102056, Aug. 2021, doi: 10.1016/j.addma.2021.102056.

[26] T. Q. Tran, F. L. Ng, J. T. Y. Kai, S. Feih, and M. L. S. Nai, “Tensile Strength Enhancement of Fused Filament Fabrication Printed Parts: A Review of Process Improvement Approaches and Respective Impact,” *Addit. Manuf.*, vol. 54, p. 102724, Jun. 2022, doi: 10.1016/j.addma.2022.102724.

[27] R. Badarinath and V. Prabhu, “Integration and evaluation of robotic fused filament fabrication system,” *Addit. Manuf.*, vol. 41, p. 101951, May 2021, doi: 10.1016/j.addma.2021.101951.

[28] I. Ferreira, M. Machado, F. Alves, and A. Torres Marques, “A review on fibre reinforced composite printing via FFF,” *Rapid Prototyp. J.*, vol. 25, no. 6, pp. 972–988, Jul. 2019, doi: 10.1108/RPJ-01-2019-0004.

[29] X. Gao, S. Qi, X. Kuang, Y. Su, J. Li, and D. Wang, “Fused filament fabrication of polymer materials: A review of interlayer bond,” *Addit. Manuf.*, vol. 37, p. 101658, Jan. 2021, doi: 10.1016/j.addma.2020.101658.

[30] B. Brenken, E. Barocio, A. Favaloro, V. Kunc, and R. B. Pipes, “Fused filament fabrication of fiber-reinforced polymers: A review,” *Addit. Manuf.*, vol. 21, pp. 1–16, May 2018, doi: 10.1016/j.addma.2018.01.002.

[31] C. Pandelidi, S. Bateman, S. Piegert, R. Hoehner, I. Kelbassa, and M. Brandt, “The technology of continuous fibre-reinforced polymers: a review on extrusion additive manufacturing methods,” *Int. J. Adv. Manuf. Technol.*, vol. 113, no. 11–12, pp. 3057–3077, Apr. 2021, doi: 10/gnxv7p.

[32] N. van de Werken, H. Tekinalp, P. Khanbolouki, S. Ozcan, A. Williams, and M. Tehrani, “Additively manufactured carbon fiber-reinforced composites: State of the art and perspective,” *Addit. Manuf.*, vol. 31, p. 100962, Jan. 2020, doi: 10/ghgkm8.

[33] P. Zhuo, S. Li, I. A. Ashcroft, and A. I. Jones, “Material extrusion additive manufacturing of continuous fibre reinforced polymer matrix composites: A review and outlook,” *Compos. Part B Eng.*, vol. 224, p. 109143, Nov. 2021, doi: 10.1016/j.compositesb.2021.109143.

[34] A. Uşun and R. Gümrük, “The mechanical performance of the 3D printed composites produced with continuous carbon fiber reinforced filaments obtained via melt impregnation,” *Addit. Manuf.*, vol. 46, p. 102112, Oct. 2021, doi: 10.1016/j.addma.2021.102112.

[35] G. Struzziero, M. Barbezat, and A. A. Skordos, “Consolidation of continuous fibre reinforced composites in additive processes: A review,” *Addit. Manuf.*, vol. 48, p. 102458, Dec. 2021, doi: 10.1016/j.addma.2021.102458.

[36] T. Suzuki, S. Fukushige, and M. Tsunori, “Load path visualization and fiber trajectory optimization for additive manufacturing of composites,” *Addit. Manuf.*, vol. 31, p. 100942, Jan. 2020, doi: 10.1016/j.addma.2019.100942.

[37] K. Yamamoto, J. V. S. Luces, K. Shirasu, Y. Hoshikawa, T. Okabe, and Y. Hirata, “A novel single-stroke path planning algorithm for 3D printers using continuous carbon fiber reinforced thermoplastics,” *Addit. Manuf.*, vol. 55, p. 102816, Jul. 2022, doi: 10.1016/j.addma.2022.102816.

[38] X. Chen, G. Fang, W.-H. Liao, and C. C. L. Wang, “Field-Based Toolpath Generation for 3D Printing Continuous Fibre Reinforced Thermoplastic Composites,” *Addit. Manuf.*, vol. 49, p. 102470, Jan. 2022, doi: 10.1016/j.addma.2021.102470.

[39] J. Li, Y. Durandet, X. Huang, G. Sun, and D. Ruan, “Additively manufactured fiber-reinforced composites: A review of mechanical behavior and opportunities,” *J. Mater. Sci. Technol.*, vol. 119, pp. 219–244, Aug. 2022, doi: 10.1016/j.jmst.2021.11.063.

[40] J. Pu, C. McIlroy, A. Jones, and I. Ashcroft, “Understanding mechanical properties in fused filament fabrication of polyether ether ketone,” *Addit. Manuf.*, vol. 37, p. 101673, Jan. 2021, doi: 10.1016/j.addma.2020.101673.

[41] H. Wu, M. Sulkis, J. Driver, A. Saade-Castillo, A. Thompson, and J. H. Koo, “Multi-functional ULTEM^{TM}1010 composite filaments for additive manufacturing using Fused Filament Fabrication (FFF),” *Addit. Manuf.*, vol. 24, pp. 298–306, Dec. 2018, doi: 10.1016/j.addma.2018.10.014.

[42] S. M. F. Kabir, K. Mathur, and A.-F. M. Seyam, “A critical review on 3D printed continuous fiber-reinforced composites: History, mechanism, materials and properties,” *Compos. Struct.*, vol. 232, p. 111476, Jan. 2020, doi: 10.1016/j.compstruct.2019.111476.

[43] L. G. Blok, M. L. Longana, H. Yu, and B. K. S. Woods, “An investigation into 3D printing of fibre reinforced thermoplastic composites,” *Addit. Manuf.*, vol. 22, pp. 176–186, Aug. 2018, doi: 10.1016/j.addma.2018.04.039.

[44] M. Iragi, C. Pascual-González, A. Esnaola, C. S. Lopes, and L. Aretxabaleta, “Ply and interlaminar behaviours of 3D printed continuous carbon fibre-reinforced thermoplastic laminates; effects of processing conditions and microstructure,” *Addit. Manuf.*, vol. 30, p. 100884, Dec. 2019, doi: 10.1016/j.addma.2019.100884.

[45] M. Luo, X. Tian, J. Shang, W. Zhu, D. Li, and Y. Qin, “Impregnation and interlayer bonding behaviours of 3D-printed continuous carbon-fiber-reinforced poly-ether-ether-ketone composites,” *Compos. Part Appl. Sci. Manuf.*, vol. 121, pp. 130–138, Jun. 2019, doi: 10.1016/j.compositesa.2019.03.020.

[46] R. Q. de Macedo, R. T. L. Ferreira, A. Gleadall, and I. Ashcroft, “VOLCO-X: Numerical simulation of material distribution and voids in extrusion additive manufacturing,” *Addit. Manuf.*, vol. 40, p. 101900, Apr. 2021, doi: 10.1016/j.addma.2021.101900.

[47] Y. Tao *et al.*, “A review on voids of 3D printed parts by fused filament fabrication,” *J. Mater. Res. Technol.*, vol. 15, pp. 4860–4879, Nov. 2021, doi: 10.1016/j.jmrt.2021.10.108.

[48] E. Polyzos, S. B. Ravindranath, D. V. Hemelrijck, and L. Pyl, “Analytical and numerical modeling of voids in additively manufactured thermoplastic parts,” *Addit. Manuf.*, vol. 48, p. 102356, Dec. 2021, doi: 10.1016/j.addma.2021.102356.

[49] D. Yang, H. Zhang, J. Wu, and E. D. McCarthy, “Fibre flow and void formation in 3D printing of short-fibre reinforced thermoplastic composites: An experimental benchmark exercise,” *Addit. Manuf.*, vol. 37, p. 101686, Jan. 2021, doi: 10.1016/j.addma.2020.101686.

[50] J. Ghorbani, P. Koirala, Y.-L. Shen, and M. Tehrani, “Eliminating voids and reducing mechanical anisotropy in fused filament fabrication parts by adjusting the filament extrusion rate,” *J. Manuf. Process.*, vol. 80, pp. 651–658, Aug. 2022, doi: 10.1016/j.jmapro.2022.06.026.

[51] M. Ueda *et al.*, “3D compaction printing of a continuous carbon fiber reinforced thermoplastic,” *Compos. Part Appl. Sci. Manuf.*, vol. 137, p. 105985, Oct. 2020, doi: 10.1016/j.compositesa.2020.105985.

[52] D. Vaes and P. Van Puyvelde, “Semi-crystalline feedstock for filament-based 3D printing of polymers,” *Prog. Polym. Sci.*, vol. 118, p. 101411, Jul. 2021, doi: 10.1016/j.progpolymsci.2021.101411.

[53] T. Choupin, B. Fayolle, G. Régnier, C. Paris, J. Cinquin, and B. Brulé, “Isothermal crystallization kinetic modeling of poly(etherketoneketone) (PEKK) copolymer,” *Polymer*, vol. 111, pp. 73–82, Feb. 2017, doi: 10.1016/j.polymer.2017.01.033.

[54] N. Yi, R. Davies, A. Chaplin, P. McCutchion, and O. Ghita, “Slow and fast crystallising poly aryl ether ketones (PAEKs) in 3D printing: Crystallisation kinetics, morphology, and mechanical properties,” *Addit. Manuf.*, vol. 39, p. 101843, Mar. 2021, doi: 10.1016/j.addma.2021.101843.

[55] H. Zhang, J. Chen, and D. Yang, “Fibre misalignment and breakage in 3D printing of continuous carbon fibre reinforced thermoplastic composites,” *Addit. Manuf.*, vol. 38, p. 101775, Feb. 2021, doi: 10.1016/j.addma.2020.101775.

[56] C. Becker *et al.*, "Experimental Quantification of the Variability of Mechanical Properties in 3D Printed Continuous Fiber Composites," *Appl. Sci.*, vol. 11, no. 23, p. 11315, Nov. 2021, doi: 10.3390/app112311315.

[57] F. Liu, E. Ferraris, and J. Ivens, "Mechanical investigation and microstructure performance of a two-matrix continuous carbon fibre composite fabricated by 3D printing," *J. Manuf. Process.*, vol. 79, pp. 383–393, Jul. 2022, doi: 10.1016/j.jmapro.2022.04.050.

[58] F. Wang, G. Wang, F. Ning, and Z. Zhang, "Fiber–matrix impregnation behavior during additive manufacturing of continuous carbon fiber reinforced polylactic acid composites," *Addit. Manuf.*, vol. 37, p. 101661, Jan. 2021, doi: 10.1016/j.addma.2020.101661.

[59] S. Terekhina, S. Egorov, T. Tarasova, I. Skornyakov, L. Guillaumat, and M. L. Hattali, "In-nozzle impregnation of continuous textile flax fiber/polyamide 6 composite during FFF process," *Compos. Part Appl. Sci. Manuf.*, vol. 153, p. 106725, Feb. 2022, doi: 10.1016/j.compositesa.2021.106725.

[60] H. Tang, Q. Sun, Z. Li, X. Su, and W. Yan, "Longitudinal compression failure of 3D printed continuous carbon fiber reinforced composites: An experimental and computational study," *Compos. Part Appl. Sci. Manuf.*, vol. 146, p. 106416, Jul. 2021, doi: 10.1016/j.compositesa.2021.106416.

[61] D. Kuba, R. Matsuzaki, S. Ochi, and S. Ogihara, "3D printing of composite materials using ultralow-melt-viscosity polymer and continuous carbon fiber," *Compos. Part C Open Access*, vol. 8, p. 100250, Jul. 2022, doi: 10.1016/j.jcomc.2022.100250.

[62] J. Audoit, L. Rivière, J. Dandurand, A. Lonjon, E. Dantras, and C. Lacabanne, "Thermal, mechanical and dielectric behaviour of poly(aryl ether ketone) with low melting temperature," *J. Therm. Anal. Calorim.*, vol. 135, no. 4, pp. 2147–2157, Feb. 2019, doi: 10.1007/s10973-018-7292-x.

[63] Toray Advanced Composites, "Toray Cetex TC1225 Data Sheet." [Online]. Available: https://bit.ly/3JtGQ0m

[64] T. D. S. Burgani, S. Alaie, and M. Tehrani, "Modeling Flexural Failure in Carbon-Fiber-Reinforced Polymer Composites," *J. Compos. Sci.*, vol. 6, no. 2, p. 33, Jan. 2022, doi: 10.3390/jcs6020033.

[65] N. Heathman, P. Koirala, T. Yap, A. Emami, and M. Tehrani, "In situ consolidation of carbon fiber PAEK via laser-assisted automated fiber placement," *Compos. Part B Eng.*, vol. 249, p. 110405, Jan. 2023, doi: 10.1016/j.compositesb.2022.110405.

[66] I. Schiel, L. Raps, A. R. Chadwick, I. Schmidt, M. Simone, and S. Nowotny, "An investigation of in-situ AFP process parameters using CF/LM-PAEK," *Adv. Manuf. Polym. Compos. Sci.*, vol. 6, no. 4, pp. 191–197, Oct. 2020, doi: 10/gpc35n.

[67] K. Zhang, H. Zhang, J. Wu, J. Chen, and D. Yang, "Improved fibre placement in filament-based 3D printing of continuous carbon fibre reinforced thermoplastic composites," *Compos. Part Appl. Sci. Manuf.*, vol. 168, p. 107454, May 2023, doi: 10.1016/j.compositesa.2023.107454.

[68] National Aeronautics and Space Administration, "ISAAC (Integrated Structural Assembly of Advanced Composites)." NASA, 2016. [Online]. Available: https://ntrs.nasa.gov/api/citations/20210023399/downloads/2021%20ISSAC%20FS%20Ft%20and%20bk.pdf

[69] Addcomposites, *AFP-XS*. [Online]. Available: https://www.addcomposites.com/afpxs

[70] D. H.-J. A. Lukaszewicz, C. Ward, and K. D. Potter, "The engineering aspects of automated prepreg layup: History, present and future," *Compos. Part B Eng.*, vol. 43, no. 3, pp. 997–1009, Apr. 2012, doi: 10.1016/j.compositesb.2011.12.003.

[71] A. Brasington, C. Sacco, J. Halbritter, R. Wehbe, and R. Harik, “Automated fiber placement: A review of history, current technologies, and future paths forward,” *Compos. Part C Open Access*, vol. 6, p. 100182, Oct. 2021, doi: 10.1016/j.jcomc.2021.100182.

[72] Grimsely BW, Cano RJ, Hudson TB, Palmieri FL, Wohl CJ, Ledesma RI, “In-Situ Consolidation Automated Fiber Placement of Thermoplastic Composites for High-Rate Aircraft Manufacturing,” in *SAMPE*, 2022, pp. 38–54.

[73] G. Reyes and U. Sharma, “Modeling and damage repair of woven thermoplastic composites subjected to low velocity impact,” *Compos. Struct.*, vol. 92, no. 2, pp. 523–531, Jan. 2010, doi: 10/cwb98z.

[74] A. Pegoretti, “Towards sustainable structural composites: A review on the recycling of continuous-fiber-reinforced thermoplastics,” *Adv. Ind. Eng. Polym. Res.*, vol. 4, no. 2, pp. 105–115, Apr. 2021, doi: 10/gn46gq.

[75] R. Bernatas, S. Dagreou, A. Despax-Ferreres, and A. Barasinski, “Recycling of fiber reinforced composites with a focus on thermoplastic composites,” *Clean. Eng. Technol.*, vol. 5, p. 100272, Dec. 2021, doi: 10/gnp6j6.

[76] M. H. Nguyen, A. A. Vijayachandran, P. Davidson, D. Call, D. Lee, and A. M. Waas, “Effect of automated fiber placement (AFP) manufacturing signature on mechanical performance of composite structures,” *Compos. Struct.*, vol. 228, p. 111335, Nov. 2019, doi: 10.1016/j.compstruct.2019.111335.

[77] M. Di Francesco, L. Veldenz, G. Dell’Anno, and K. Potter, “Heater power control for multi-material, variable speed Automated Fibre Placement,” *Compos. Part Appl. Sci. Manuf.*, vol. 101, pp. 408–421, Oct. 2017, doi: 10.1016/j.compositesa.2017.06.015.

[78] S.-L. Gao and J.-K. Kim, “Correlation among crystalline morphology of PEEK, interface bond strength, and in-plane mechanical properties of carbon/PEEK composites,” *J. Appl. Polym. Sci.*, vol. 84, no. 6, pp. 1155–1167, May 2002, doi: 10.1002/app.10406.

[79] V. Kishore *et al.*, “Additive Manufacturing of High Performance Semicrystalline Thermoplastics and Their Composites,” in *Solid Freeform Fabrication Symposium*, 2016, p. 10.

[80] C. M. Stokes-Griffin, P. Compston, T. I. Matuszyk, and M. J. Cardew-Hall, “Thermal modelling of the laser-assisted thermoplastic tape placement process,” *J. Thermoplast. Compos. Mater.*, vol. 28, no. 10, pp. 1445–1462, Oct. 2015, doi: 10.1177/0892705713513285.

[81] P. M. Schaefer, D. Gierszewski, A. Kollmannsberger, S. Zaremba, and K. Drechsler, “Analysis and improved process response prediction of laser- assisted automated tape placement with PA-6/carbon tapes using Design of Experiments and numerical simulations,” *Compos. Part Appl. Sci. Manuf.*, vol. 96, pp. 137–146, May 2017, doi: 10.1016/j.compositesa.2017.02.008.

[82] C. M. Stokes-Griffin and P. Compston, “An inverse model for optimisation of laser heat flux distributions in an automated laser tape placement process for carbon-fibre/PEEK,” *Compos. Part Appl. Sci. Manuf.*, vol. 88, pp. 190–197, Sep. 2016, doi: 10.1016/j.compositesa.2016.05.034.

[83] J. Tierney and J. W. Gillespie, “Modeling of In Situ Strength Development for the Thermoplastic Composite Tow Placement Process,” *J. Compos. Mater.*, vol. 40, no. 16, pp. 1487–1506, Aug. 2006, doi: 10.1177/0021998306060162.

[84] O. Çelik *et al.*, “The influence of inter-laminar thermal contact resistance on the cooling of material during laser assisted fiber placement,” *Compos. Part Appl. Sci. Manuf.*, vol. 145, p. 106367, Jun. 2021, doi: 10.1016/j.compositesa.2021.106367.

[85] C. M. Stokes-Griffin and P. Compston, “Investigation of sub-melt temperature bonding of carbon-fibre/PEEK in an automated laser tape placement process,” *Compos. Part Appl. Sci. Manuf.*, vol. 84, pp. 17–25, May 2016, doi: 10.1016/j.compositesa.2015.12.019.

[86] R. Pitchumani, S. Ranganathan, R. C. Don, J. W. Gillespie, and M. A. Lamontia, “Analysis of transport phenomena governing interfacial bonding and void dynamics during thermoplastic tow-placement,” *Int. J. Heat Mass Transf.*, vol. 39, no. 9, pp. 1883–1897, Jun. 1996, doi: 10.1016/0017-9310(95)00271-5.

[87] L. J. Bastien and J. W. Gillespie, “A non-isothermal healing model for strength and toughness of fusion bonded joints of amorphous thermoplastics,” *Polym. Eng. Sci.*, vol. 31, no. 24, pp. 1720–1730, Dec. 1991, doi: 10.1002/pen.760312406.

[88] S. Tumkor, N. Turkmen, C. Chassapis, and S. Manoochehri, “Modeling of heat transfer in thermoplastic composite tape lay-up manufacturing,” *Int. Commun. Heat Mass Transf.*, vol. 28, no. 1, pp. 49–58, Jan. 2001, doi: 10.1016/S0735-1933(01)00212-3.

[89] M. Narnhofer, R. Schledjewski, P. Mitschang, and L. Perko, “Simulation of the Tape-Laying Process for Thermoplastic Matrix Composites,” *Adv. Polym. Technol.*, vol. 32, no. S1, pp. E705–E713, Mar. 2013, doi: 10.1002/adv.21312.

[90] C. M. Stokes-Griffin and P. Compston, “Laser-Assisted Tape Placement of Thermoplastic Composites: The Effect of Process Parameters on Bond Strength,” in *Sustainable Automotive Technologies 2013*, J. Wellnitz, A. Subic, and R. Trufin, Eds., in Lecture Notes in Mobility. Cham: Springer International Publishing, 2014, pp. 133–141. doi: 10.1007/978-3-319-01884-3_13.

[91] S. G. A. Sridhar Ranganathan, “A Non-Isothermal Process Model for Consolidation and Void Reduction during In-Situ Tow Placement of Thermoplastic Composites.pdf,” *J. Compos. Mater.*, vol. 29, no. 8, 1995.

[92] M. A. Khan, P. Mitschang, and R. Schledjewski, “Tracing the Void Content Development and Identification of its Effecting Parameters during in Situ Consolidation of Thermoplastic Tape Material,” *Polym. Polym. Compos.*, vol. 18, no. 1, pp. 1–15, Jan. 2010, doi: 10.1177/096739111001800101.

[93] A. R. Chadwick, K. Kotzur, and S. Nowotny, “Moderation of thermoplastic composite crystallinity and mechanical properties through in situ manufacturing and post-manufacturing tempering: Part 1 – Mechanical characterisation,” *Compos. Part Appl. Sci. Manuf.*, vol. 143, p. 106286, Apr. 2021, doi: 10.1016/j.compositesa.2021.106286.

[94] T. H. Fazil O. Sonmez, “Modeling of Heat Transfer and Crystallization in Thermoplastic Composite Tape Placement Process.pdf,” *J. Thermoplast. Compos. Mater.*, vol. 10, May 1997.

[95] M. Eimanlou, “Investigation of the effect of process parameters on bond strength of thermoplastic composite rings manufactured using fiber laser,” p. 97.

[96] J. Chen, K. Fu, and Y. Li, “Understanding processing parameter effects for carbon fibre reinforced thermoplastic composites manufactured by laser-assisted automated fibre placement (AFP),” *Compos. Part Appl. Sci. Manuf.*, vol. 140, p. 106160, Jan. 2021, doi: 10/gk6gs7.

[97] E. Oromiehie, A. K. Gain, and B. G. Prusty, “Processing parameter optimisation for automated fibre placement (AFP) manufactured thermoplastic composites,” *Compos. Struct.*, vol. 272, p. 114223, Sep. 2021, doi: 10/gkdskb.

[98] C. M. Stokes-Griffin and P. Compston, “The effect of processing temperature and placement rate on the short beam strength of carbon fibre–PEEK manufactured using a laser

tape placement process," *Compos. Part Appl. Sci. Manuf.*, vol. 78, pp. 274–283, Nov. 2015, doi: 10.1016/j.compositesa.2015.08.008.

[99] Gautam Kumar Jeyakodi, "Finite Element Simulation of the In - Situ AFP process for Thermoplastic Composites using Abaqus," Delft University of Technology, 2016.

[100] S. Adhikari, C. J. Durning, J. Fish, J.-W. Simon, and S. K. Kumar, "Modeling Thermal Welding of Semicrystalline Polymers," *Macromolecules*, vol. 55, no. 5, pp. 1719–1725, Mar. 2022, doi: 10.1021/acs.macromol.1c02612.

[101] P. Simacek, S. G. Advani, M. Gruber, and B. Jensen, "A non-local void filling model to describe its dynamics during processing thermoplastic composites," *Compos. Part Appl. Sci. Manuf.*, vol. 46, pp. 154–165, Mar. 2013, doi: 10.1016/j.compositesa.2012.10.015.

[102] Nathaniel Heathman, Joseph Kirchhoff, Timothy Yap, and Mehran Tehrani, "Understanding Interlaminar Bonding and Fracture Toughness in In-Situ Consolidated Automated Fiber Placement of Carbon Fiber LM-PAEK Composites," presented at the SAMPE 2023 Conference

[103] Ginger Gardiner, "Thermoplastic composite demonstrators — EU roadmap for future airframes," *Composites World*, Jan. 29, 2018. [Online]. Available: https://www.compositesworld.com/articles/thermoplastic-composite-demonstrators-eu-roadmap-for-future-airframes-

[104] Rick Young, "Hi-Rate composite Aircraft Manufacturing (HiCAM) Project Overview," NASA. [Online]. Available: https://ntrs.nasa.gov/api/citations/20220010030/downloads/HiCAM%20Overview%20Apr_2022_WebV2.pdf

[105] E. Oromiehie, A. K. Gain, M. J. Donough, and B. G. Prusty, "Fracture toughness assessment of CF-PEEK composites consolidated using hot gas torch assisted automated fibre placement," *Compos. Struct.*, vol. 279, p. 114762, Jan. 2022, doi: 10.1016/j.compstruct.2021.114762.

[106] Z. Qureshi, T. Swait, R. Scaife, and H. M. El-Dessouky, "In situ consolidation of thermoplastic prepreg tape using automated tape placement technology: Potential and possibilities," *Compos. Part B Eng.*, vol. 66, pp. 255–267, Nov. 2014, doi: 10/gj3bpm.

[107] A. K. Bandaru, G. J. Clancy, D. Peeters, R. O'Higgins, and P. M. Weaver, "Interface Characterization of Thermoplastic Skin-Stiffener Composite Manufactured using Laser-Assisted Tape Placement," in *2018 AIAA/ASCE/AHS/ASC Structures, Structural Dynamics, and Materials Conference*, Kissimmee, Florida: American Institute of Aeronautics and Astronautics, Jan. 2018. doi: 10.2514/6.2018-0481.

[108] Toray Advanced Composites, "Toray Cetex TC1200 PEEK Data Sheet." [Online]. Available: https://www.toraytac.com/media/7765d981-1f9f-472d-bf24-69a647412e38/Pr7gdw/TAC/Documents/Data_sheets/Thermoplastic/UD%20tapes,%20prepregs%20and%20laminates/Toray-Cetex-TC1200_PEEK_PDS.pdf

[109] I. M. Daniel and O. Ishai, *Engineering mechanics of composite materials*, 2nd ed. New York: Oxford University Press, 2006.

[110] D. Ray *et al.*, "Fracture toughness of carbon fiber/polyether ether ketone composites manufactured by autoclave and laser-assisted automated tape placement," *J. Appl. Polym. Sci.*, p. n/a-n/a, Nov. 2014, doi: 10.1002/app.41643.

[111] S.-L. Gao and J.-K. Kim, "Cooling rate in¯uences in carbon fibre/PEEK composites. Part II: interlaminar fracture toughness," 2001.

[112] Yap, Timothy, Tamijani, Ali, and Tehrani, Mehran, “Effects of Tape Staggering Pattern on Interlaminar Strength and Surface Quality of In-situ Consolidated Automated Fiber Placement Thermoplastic Composites,” *AIAA SciTech*, 2023.

[113] Evelyn Lian, “Medium Toughness PAEK thermoplastics Toray Cetex TC1225 (LM-PAEK) T700 12K T1E Unidirectional Tap 145 gsm 34% RC Qualification Material Property Data Report.” Wichita State University National Institute for Aviation Research, Feb. 21, 2020. [Online]. Available: https://www.wichita.edu/industry_and_defense/NIAR/Documents/CAM-RP-2019-036-Rev-NC-February-21-2020-MPDR.PDF

[114] M. Wynn and N. Zobeiry, “Investigating the Effect of Temperature History on Crystal Morphology of Thermoplastic Composites Using In Situ Polarized Light Microscopy and Probabilistic Machine Learning,” *Polymers*, vol. 15, no. 1, p. 18, Dec. 2022, doi: 10.3390/polym15010018.